ISTANBUL TECHNICAL UNIVERSITY ★ GRADUATE SCHOOL

DEVELOPMENT OF A NONLINEAR SONIC BOOM PROPAGATION CODE

M.Sc. THESIS

Yusuf DEMİROĞLU

Department of Aeronautical And Astronautical Engineering

Astronautics and Aeronautics Engineering Programme

JANUARY 2023

ISTANBUL TECHNICAL UNIVERSITY ★ GRADUATE SCHOOL

DEVELOPMENT OF A NONLINEAR SONIC BOOM PROPAGATION CODE

M.Sc. THESIS

Yusuf DEMİROĞLU
(511191144)

Department of Aeronautical And Astronautical Engineering

Astronautics and Aeronautics Engineering Programme

Thesis Advisor: Prof. Dr. Melike NİKBAY

JANUARY 2023

İSTANBUL TEKNİK ÜNİVERSİTESİ ★ LİSANSÜSTÜ EĞİTİM ENSTİTÜSÜ

DOĞRUSAL OLMAYAN SONİK PATLAMA YAZILIMI GELİŞTİRİLMESİ

YÜKSEK LİSANS TEZİ

Yusuf DEMİROĞLU
(511191144)

Uçak ve Uzay Mühendisliği Anabilim Dalı

Uçak ve Uzay Mühendisliği Programı

Tez Danışmanı: Prof. Dr. Melike NİKBAY

OCAK 2023

Yusuf DEMİROĞLU, a M.Sc. student of ITU Graduate School student ID 511191144, successfully defended the thesis entitled “DEVELOPMENT OF A NONLINEAR SONIC BOOM PROPAGATION CODE ”, which he prepared after fulfilling the requirements specified in the associated legislations, before the jury whose signatures are below.

Thesis Advisor : **Prof. Dr. Melike NİKBAY** ....
Istanbul Technical University

Jury Members : **Assoc. Prof. Baha ZAFER** ....
Istanbul Technical University

Assoc. Prof. Leifur T. LEIFSSON ....
Purdue University

Date of Submission : 30 December 2022
Date of Defense : 24 January 2023

To my family,

FOREWORD

First, I would like to express my gratitude to my thesis advisor Prof. Melike Nikbay for her support, patience, and guidance throughout my master's study at ITU AeroMDO Lab. I am very pleased for having a chance to study sonic boom propagation and supersonic low-boom aircraft design under her supervision.

I would like to thank my colleagues from ITU AeroMDO Lab for giving me an opportunity to work with an excellent team; Hüseyin Emre Tekaslan, Şıhmehmet Yıldız, Enes Çakmak, Dilan Kılıç, Emre Kara, and Rumed İmrak.

I would like to express my thanks to all my friends for their support in every aspect during my graduate study; Vatan Aksoy Tezer, Utkun Erinç Malkoçoğlu, Tamer Şener, Hasan Karali, Ertuğrul Barış Öndeş, Samet Uzun, and M.D. Furkan Şekerci.

I acknowledge NASA Langley Research Center for providing sBOOM software to our research group. Having sBOOM software was a great advantage for me in validating my results.

Finally, I would like to acknowledge the project funding by TÜBİTAK for the 218M471 project and the graduate thesis support provided by the Istanbul Technical University Scientific Research Program for MYL-2020-42758 project titled "Development of a Non-Linear Sonic Boom Propagation Code".

January 2023

Yusuf DEMİROĞLU
Research Assistant

TABLE OF CONTENTS

Page

ABBREVIATIONS

AIAA	: American Institute of Aeronautics and Astronautics
CFD	: Computational Fluid dynamics
FAA	: Federal Aviation Administration
FFD	: Free-Form Deformation
HSCT	: High-speed Civil Transport
ISPR	: Initial Shock Pressure Rise
JST	: Jameson-Schmidt-Turkel
KZK	: Khokhlov-Zabolotskaya-Kuznetsov
NASA	: National Aeronautics And Space Administration
JAXA	: Japanese Space Agency
JSGD	: Jones-Seebass-George-Darden
JWB	: Jaxa-Wing Body
WPM	: Waveform Parameter Method
SBPW	: Sonic Boom Prediction Workshop

SYMBOLS

A	: ray tube area
A_h	: horizontal projection of ray tube area
A_{slice}	: area of a slice
c	: speed of sound
c_0	: ambient speed of sound
C_v	: dimensionless dispersion parameter
$\hat{f}$	: surface source distribution
$f_{r,v}$	: relaxation frequency
k	: nonlinear age coefficient
K_1	: Bessel function of the second kind
L	: lift distribution
L_{slice}	: lift of a slice
H	: Heaviside function
h	: absolute humidity
h_r	: relative humidity
M	: Mach number
N	: number of points in the waveform
$\vec{n}$	: ray path normal direction
p'	: acoustic pressure
P	: dimensionless pressure
p_0	: reference pressure
p_{sat}	: saturation vapor pressure
Pr	: Prandtl number
q	: dynamic pressure
r	: axial coordinate
R	: radius distribution
s	: ray tube coordinate
S_{eq}	: total equivalent area distribution
S_L	: equivalent area distribution due to the lift
S_V	: equivalent area distribution due to the volume
t	: time
t'	: retarded time
T	: temperature
T_0	: reference temperature
u	: wind velocity component in $y$direction
$\vec{W}$	: wind velocity vector
$\vec{x}$	: shock formation distance
x, y, z	: Global Cartesian coordinates

α_c^{tv} : thermoviscous attenuation coefficient
β : Prandtl-Glauert coefficient
γ : ratio of specific heats
Γ : dimensionless thermoviscous parameter
ζ : dummy integration variable
θ : wave normal inclination angle
κ : thermal conductivity
μ : shear viscosity coefficient
μ_B : bulk viscosity
ρ_0 : ambient density
σ : dimensionless distance
τ : dimensionless time
ϕ : azimuth angle
$\hat{\phi}$: perturbation potential function
ω_0 : angular frequency

LIST OF TABLES

LIST OF FIGURES

Page

DEVELOPMENT OF A NONLINEAR SONIC BOOM PROPAGATION CODE

SUMMARY

Civil supersonic flight is still one of the most challenging research topics in the aerospace industry. Since Concorde's last flight in 2003, researchers tried to find efficient solutions to make supersonic flights more affordable and reliable. Meanwhile, with the advance of computational power, computational fluid dynamics (CFD) has been implemented in advanced optimization studies involved in elevating supersonic aircraft design processes with given operational criteria and requirements. However, reducing the cost of a supersonic flight by increasing aerodynamic efficiency is not the only concern in civil supersonic transport. The second most important factor for a supersonic aircraft is the noise produced on land due to the shock waves that propagate through the atmosphere to the ground. This phenomenon is called sonic boom which is addressed in this thesis study.

A sonic boom generated by a supersonic aircraft can cause very loud noise on the ground that may exceed 100 decibels. This loudness value is not acceptable due to its effects on people's daily life. Therefore, to enable civil supersonic flight over land, sonic boom loudness must be eliminated or reduced below a certain level. This effort is called sonic boom minimization and there are several methodologies that are provided in this study. Lots of studies for sonic boom minimization utilize optimization algorithms that call sonic boom prediction tools along with the CFD solvers. Therefore, to reduce sonic boom loudness, a sonic boom propagation code that accurately predicts sonic boom loudness is essential for the multidisciplinary design optimization of civil supersonic aircraft. In this regard, a new nonlinear sonic boom prediction code, named ITUBOOM, is developed in-house to be incorporated into our design optimization studies to achieve a low-boom aircraft geometry.

ITUBOOM is developed in Python programming language for ease of implementation for design studies. A sonic boom calculation process can be broken down into three main steps; a near-field solution with CFD to generate an initial acoustic signal, atmospheric propagation with acoustics methods, and loudness calculation. Unlike other sonic boom codes, ITUBOOM can also be used to generate a near-field pressure directly from CFD outputs by surface slicing or in-flow signature extraction. Then, it can be used to perform atmospheric propagation by taking into account nonlinear effects such as molecular relaxation and thermoviscous attenuation. Results of ITUBOOM are validated against NASA Langley Research Center's well-known sBOOM code for different conditions on benchmark problems and presented in this thesis in detail.

DOĞRUSAL OLMAYAN SONİK PATLAMA YAZILIMI GELİŞTİRİLMESİ

ÖZET

Ses-üstü sivil hava taşımacılığı uzay ve havacılık alanında hala önemini korumaktadır. Seyahat süresini neredeyse yarıya indiren ses-üstü sivil hava taşımacılığı 1960lı yıllara kadar uzanmaktadır. Concorde isimli uçak sesten 2 kat hızlı uçmak üzere tasarlanmış ve ilk uçuşunu 1969 yılında yapmıştır. 20 yıldan fazla hizmette kalan Concorde uçağı 2003 yılında servisten çıkarılmıştır. O tarihten günümüze kadar ise ses-üstü taşımacılık çalışmaları tasarım aşamasında devam etmektedir.

Concorde uçağının hizmetten çıkarılmasının temel nedeni operasyon maliyetlerinin çok yüksek olmasıydı. Ses-üstü uçuşun doğası gereği uçuş hızı arttıkça operasyon maliyeti de o oranda artmaktadır. Bu nedenle araştırmacılar daha verimli tasarımlar bulma yoluna gittiler. Yıllar içinde hesaplama gücünün de artması ile, modern sayısal hesaplama yöntemleri kullanarak bütün uçak geometrileri için tasarım optimizasyonu çalışmaları başladı. Bu optimizasyon çalışmalarında optimizasyon algoritmasını hesaplamalı akışkanlar dinamiği (HAD) yazılımlarına bağlayarak aerodinamik olarak en verimli uçak geometrisinin bulunması amaçlanmaktadır.

Ses-üstü hızlarda uçan uçakların etrafında oluşan şok dalgaları atmosfer boyunca ilerleyerek yere kadar ulaşır. Bu ilerleme esnasında her bir şok dalgasının yerel olarak ses hızını değiştirmesinden dolayı uçak etrafında oluşan bir çok şok dalgası önde ve arkadan olmak üzere birleşerek güçlü 2 dalga halini alır. Bu dalga yapısı N-dalgası olarak isimlendirilmektedir ve yere ulaştığında yüksek seviyede bir gürültüye neden olmaktadır. Genellikle bu gürültü seviyesi 100 desibelin üzerindedir. Bu nedenle ses-üstü uçuş dünyanın bir çok yerinde yerleşim yerleri üzerinde yasaklanmıştır.

Sonik patlama etkenini de göz önünde bulundurunca sivil ses-üstü ulaşım için yapılan optimizasyon çalışmalarına sonik patlamanın da dahil edilmesi gerektiği görülmektedir. Geçmiş yıllarda sonik patlamayı düşürmek için bazı yöntemler geliştirilmiş ve sonik patlama minimizasyonu olarak isimlendirilmiştir. Bu yöntemler temel olarak doğrusallaştırılmış akış denklemleri üzerine kurulmuştur. Ancak bilgisayar teknolojisindeki ilerlemeler ile hesaplama gücümüz artmış ve araştırmacılar 2000'li yıllardan itibaren HAD analizlerini sonik patlama optimizasyonlarında kullanmaya başlamıştır. Çok-disiplinli optimizasyon olarak adlandırılan bu optimizasyon çalışmalarında hem HAD analiz aracı hem de sonik patlama yazılımı çağırılarak sonik patlama seviyesinin düşürülmesi hedeflenmiştir. Bu bağlamda, yerdeki sonik patlama seviyesini doğru bir şekilde hesaplayan bir sonik patlama yazılımının öneminin arttığı görülmektedir.

Sonik patlama hesaplamaları 1950'li yıllara kadar uzanmaktadır. Bu alandaki ilk çalışma Gerald B. Whitham tarafından 1952 yılında yayınlanmıştır. Bu çalışmada temel olarak ses-üstü hızlarda bir akışkan içerisine yerleştirilen bir cismin akış içerisinde oluşturduğu bozuntunun uzak mesafelere etkisini incelemiştir. Daha önceki çalışmalarda kullanılan doğrusallaştırılmış sıkıştırılabilir akış denklemlerini modifiye ederek kullanmıştır. Whitham'ın geliştirdiği bu yöntem Whitham F-fonksiyonu olarak adlandırılmış ve 2000'li yıllara kadar sonik patlama tahmininde kullanılmıştır. Whitham'ın geliştirdiği yöntem her ne kadar sadece eksenel simetrik cisimler için uygulanıyor olsa da daha sonraki yıllarda bu yöntem herhangi bir uçak geometrisi için eşdeğer alan dağılımı kullanılarak genişletilmiştir. Karmaşık bir geometri üzerinden hesaplanan eşdeğer alan dağılımı o geometriye denk gelen eksenel bir cismi ifade etmektedir.

Whitham'ın geliştirdiği bu yöntem değişmeyen atmosfer ortamı için geçerli olsa da, daha sonraki yıllarda tabakalı atmosfer yapısını hesaba katacak şekilde uygulamaları yapılmıştır. Ancak bu yöntem doğrusal teori üzerine kurulduğu için doğrusal olmayan etkileri hesaba katmamaktadır.

Sonik patlama dalgaları sonlu büyüklüğe sahip küresel yayılan ses dalgaları olarak düşünülebilir. Bu ses dalgaları atmosfer ortamı içerisinde ilerlerken kısa mesafelerde ihmal edilebilecek bazı etkiler uzun mesafelerde önem kazanmaktadır. Dolayısıyla yerdeki sonik patlama gürültüsünü doğru tahmin edebilmek için bu etkilerin de hesaba katılması gerekmektedir. Bu nedenle bu alanda devam eden çalışmalarda, sonik patlama dalgalarının atmosfer içinde ilerlemesi, sonlu büyüklüğe sahip ses dalgalarının yayılmasının termo-viskoz zayıflama ve moleküler gevşeme gibi doğrusal olmayan etkilerin de hesaba katılması ile modellenmiştir. Bu yönteme dayanan ve en yaygın olarak kullanılan sonik patlama yazılımı NASA Langley Araştırma Merkezi tarafından geliştirilen sBOOM yazılımıdır. Bu yazılım geometrik akustik yöntemlerini kullanarak bir ışın tüpü çözüm alanı oluşturup daha sonra bu çözüm alanı içerisinde dalga denklemini çözmektedir. 2011 yılında yayınlanan bu çalışmadan sonra bir çok sonik patlama çalışmasında bu yazılım kullanılmıştır. Ancak bu yazılım açık kaynak değildir ve kullanılabilmesi için özel izinle talep edilmesi gerekmektedir. Ayrıca sBOOM yazılımının uluslararası kullanıcılara dağıtımında kabiliyetleri sınırlı olan 1.sürümünün lisansı verilmektedir.

Bu çalışmada ITUBOOM olarak isimlendirilen bir sonik patlama yazılımı geliştirilmiştir. Bu yazılım hem doğrusal teoriye dayanan Whitham F-fonksiyonu yöntemini hem de doğrusal olmayan etkilerin hesaba katıldığı birleştirilmiş Burger denklemlerinin çözümünü içermektedir. Python programlama dilinde geliştirilen bu yazılım diğer sonik patlama yazılımlarından farklı olarak direkt bir HAD analizi çıktısını kullanarak yakın alan basınç izi üretebilmektedir. Daha sonra bu yakın alan basınç izini kullanarak atmosfer içerinde dalga ilerlemesi çözümü yapmaktadır. Bu aşamada standart atmosfer profilleri kullanılsa da kullanıcı herhangi bir atmosfer profilini girdi olarak yazılıma verebilmektedir. Yerdeki basınç izi hesaplandıktan sonra bu basınç izi kullanılarak gürültü seviyesi hesaplanmaktadır.

ITUBOOM içerisinde yakın alan basınç izi hesaplama aşamasında 3 farklı seçenek kullanılabilmektedir; doğrudan bir sinyal girilmesi, uçak yüzeyi üzerinden basınç izi hesabı ve akış alanı içerisinden basınç dağılımının çıkartılması. Kullanıcının hali hazırda bir yakın alan basınç sinyalini kullanması durumunda bu yazılıma direkt olarak girilebilmektedir. Ancak bir çok çalışmada bu yakın alan basınç sinyalinin HAD analizi çıktısından ve panel yöntemi gibi düşük doğruluklu yöntemlerle hesaplanan çıktılardan elde edilmesi gerekmektedir. Bu bağlamda kullanıcının sadece uçak yüzeyini kullanarak yakın alan basınç dağılımı kullanması durumunda ITUBOOM dilimleme yöntemi kullanarak uçağın ekseni boyunca eşdeğer alan dağılımı hesaplayıp, daha sonra bu eşdeğer alan dağılımını basınç sinyaline çevirmektedir. Mach sayısı ve azimut açısına bağlı olarak bu dilimlerin oryantasyonu belirlenmektedir. Daha sonra her bir dilim düzleminin uçağın yüzeyi ile olan kesişimi eğrisi hesaplanıp, bu eğri boyunca 2 farklı çizgi integrali işlemi yapılmaktadır. Birinci integral ile kesişim eğrisinin oluşturduğu kapalı alan hesaplanmaktadır. İkinci integral işleminde ise bu eğri boyunca basınç, yüzey normalleri ve hücre alanı kullanılarak bu eğri üzerindeki toplam taşıma kuvveti hesaplanmaktadır. Uçağın boylamsal ekseni boyunca elde edilen bu iki alan dağılımı hacim katkısı ve taşıma katkısı olarak isimlendirilir ve toplanarak bütün eşdeğer alan dağılımı elde edilir.

HAD analizinden bütün akış alanı çıktısı verilmesi durumunda ise ITUBOOM için gerekli olan girdi direkt olarak akış alanı içerisinden hesaplanabilmektedir. Bu bağlamda ITUBOOM sonik patlama optimizasyon çalışmalarında genel algoritmaya entegrasyonu konusunda diğer yazılımlara kıyasla kolaylık sağlamaktadır.

Yakın alan basınç izi sağlandıktan sonra uçuş koşulları ve atmosfer profilleri yazılıma girilerek sonik patlama analizi başlatılmaktadır. Tabakalı atmosfer irtifaya bağlı olarak tanımlanmış 4 adet profil ile tanımlanabilir; sıcaklık profili, basınç profili, bağıl nem profili, ve yatay rüzgar profili. Bağıl nem profili özellikle moleküler gevşeme ile direkt olarak bağlantılıdır ve farklı bağıl nem profillerinin sonik patlama gürültüsüne etkisinin oldukça önemli olduğu literatürdeki çalışmalarda gösterilmiştir. Kullanılan yöntemden kaynaklı olarak sadece yatay rüzgar hesaba katılmaktadır. Bu aşamada yazılım ilk önce 4 adet ışının gideceği yolun uçuş irtifasından yere kadar olan koordinatlarını hesaplamaktadır. Atmosferin homojen özelliklere sahip olması durumunda bu ışınların geometrisi birer doğru parçası olacaktır. Ancak tabakalı atmosfer durumunda bu ışınlar kırınıma uğrayarak yere yaklaştıkça yer düzlemi ile yaptıkları açı azalmaktadır. Bu 4 ışın birbirinden farklı azimut açıları ve zaman adımları ile ayrılmaktadır. 4 ışının arasında kalan hesaplanarak ışın tüpü alanı olarak isimlendirilir ve dalga ilerlemesi boyunca dalganın toplam enerjisinin hesaplamasında kullanılır. Bu prensip Blokhintzev değişmezi olarak isimlendirilmektedir.

Işın tüplerinin alanları ve yörüngesi hesaplandıktan sonra birleştirilmiş Burger denklemi uçaktan yere kadar ışın koordinat ekseninde çözülmektedir. Sayısal çözüm için operatör ayırma yöntemi olarak isimlendirilen bir yöntem kullanılmıştır. Bu yöntemde diferansiyel denklem içerisinde bulunan her bir terim ayrı ayrı çözülerek sonuçlar toplanmaktadır. Denklem içerisinde doğrusal olmayan terim olarak isimlendirilen terim Poisson çözümü ile, termo-viskoz azalma ve moleküler gevşeme terimleri ise Crank-Nicolson yöntemi ile çözülmektedir. Yazılım içerisinde adım boyutu çözüm esnasında dinamik olarak kontrol edilmektedir. Sayısal çözüm için basınç sinyalinin belli bir sayının üzerinde örneklenmesi gerekmektedir. 10000 noktadan oluşan bir sinyalin çözüm doğruluğu açısından yeterli olduğu görülmüştür.

ITUBOOM yazılımı geliştirildikten sonra NASA'nın sBOOM yazılımı ile doğrulama çalışması yapılmıştır. Farklı uçak geometrileri, uçuş koşulları ve atmosfer profilleri kullanılarak yapılan kıyaslama çalışmalarında ITUBOOM yazılımının oldukça yakın sonuçlar verdiği görülmektedir. Bu bağlamda ITUBOOM yazılımının ses-üstü uçak tasarımı çalışmalarında kullanılabileceği görülmüştür.

1. INTRODUCTION

The supersonic flight era began in 1947 as Chuck Yeager exceeds Mach 1 with the rocket-powered Bell X-1 experimental aircraft. Later, this experimental flight was followed by other experimental projects and military applications. Even though there was no civil supersonic activity in the early years of supersonic flight, supersonic civil airliners emerged in the 1960s. While Boeing 2707 supersonic airliner remained as a design project due to the funding cut in 1971 [9], Tupolev TU- 144 and Concorde made their first flights in 1968 and 1969, respectively. Concorde was used until 2003 before it retired due to the high operation costs. Besides the high cost of supersonic flights, the sonic boom generated by the aircraft itself is the second important burden for supersonic travel. Due to the high-level noise, supersonic flight was prohibited over land by Federal Aviation Administration (FAA) in 1973 [10]. Therefore, considering sonic boom loudness during the design process is essential for supersonic flight. Even though there were earlier attempts to reduce sonic boom loudness such as the High-speed Civil Transport (HSCT) design project [11] or sonic boom conferences [12], researchers focused on sonic boom minimization during the design of supersonic airliners after Concorde's retirement [13–16].

Many shock waves occur on the surface of an aircraft in the supersonic regime. Figure 1.1 illustrates the flow structure around NASA X-59 low-boom flight demonstrator aircraft [1]. This picture reveals these shock structures near the aircraft. Each of these shock waves changes the local speed of sound around them. This change causes all shock and expansion waves to coalesce with each other in the front and rear sections of the pressure signal [17]. Therefore, as shock waves travel in the atmosphere, they form an N-shape signature called N-wave. The main effort of low-boom aircraft design is to prevent the formation of an N-wave during atmospheric propagation. This indicates that accurate modeling of shock waves' propagation is essential to achieve a low-boom design.

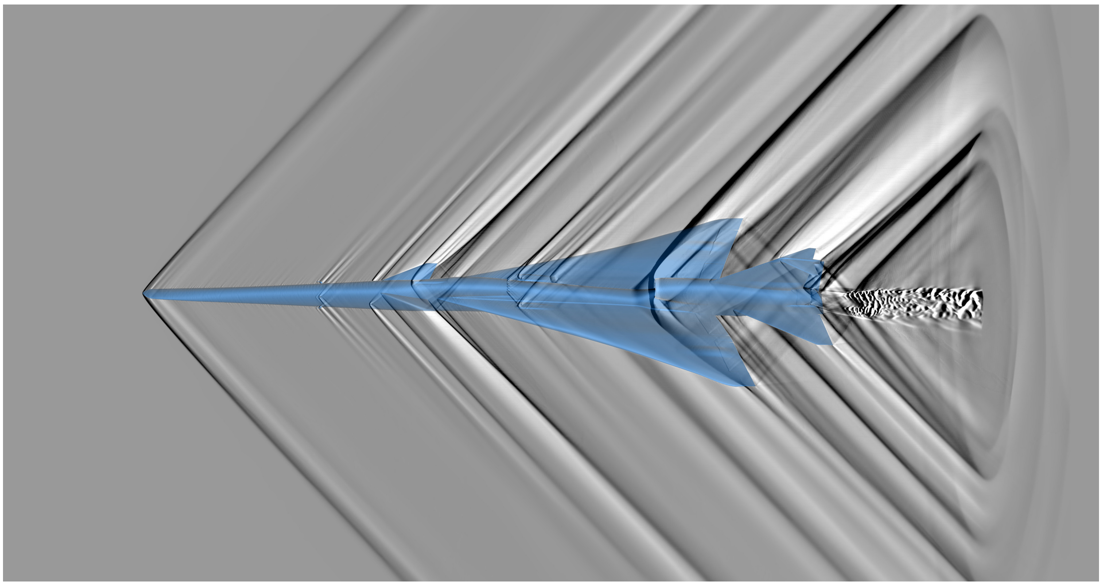

Figure 1.1 : Supersonic flow around NASA X-59 model [1]

In this regard, a sonic boom prediction tool, named ITUBOOM, is developed in this study to be used for the design optimization of supersonic aircraft. ITUBOOM utilizes both linear and non-linear methods developed over the years. ITUBOOM is written in Python language for the sake of ease of implementation in an optimization framework. In the following sections, an overview of the development of the sonic boom theory is presented. Then, developed tools with these methods are provided.

1.1 Organization

The organization of this thesis can be summarized as follows. In Section 1, a literature survey is presented from a historical perspective. Existing studies for the classical methods and modern methods in the field are given. In Section 2, methodologies for these methods which are the basis of ITUBOOM are provided in detail. In Section 3, numerical solution methods in ITUBOOM are explained with an illustration of program structure. In Section 4, a validation study, an extensive application case, and the results of ITUBOOM are discussed. Finally, in Section 5, a conclusion from this study is given with the goals of future works which are required to make ITUBOOM a more accurate prediction tool.

1.2 History and Development of Sonic Boom Theory

Sonic boom prediction methods can be divided into two sections; classical methods and nonlinear methods.

1.2.1 Classical methods

Sonic boom research dates back almost to the first supersonic flight. In 1952, Gerald B. Whitham published his study titled *The Flow Pattern of a Supersonic Projectile* [18]. This study was an extension of a supersonic linearized flow solution to far distances [19]. As the distance between the object and the point of interest increases, the linearized solution looses its validity due to the straight and parallel characteristic curves assumption. Since the supersonic flow is nonlinear, the characteristic curves propagate in nonlinear paths to far distances. Also, shock waves can only be created with overlapping characteristics. To address this issue, Whitham proposed a new relation for the characteristic curves to increase the accuracy of the solution for the far distances. According to his proposition, characteristics no longer had to be parallel straight lines, instead, they can intersect and form shock waves with a new relation called nonlinear aging. This method is also called "modified linear theory". Whitham's method was only valid for axisymmetrical objects with the small angle assumption. Small angle assumption requires moderate angles of attack and slender bodies such as projectiles. This theory was not applicable to supersonic aircraft due to the continuous axisymmetrical body assumption. Therefore, it had to be modified to make it applicable to aircraft geometries.

One issue of Whitham's formula about characteristics was multi-valued pressure values after the intersection. He solved this problem with the equal area rule that is explained in detail in Section 2. The equal area rule basically derived from the weak shock theory to eliminate non-physical multi-valued regions. Figure 1.2 shows the behavior of characteristics with the modified linear method [20].

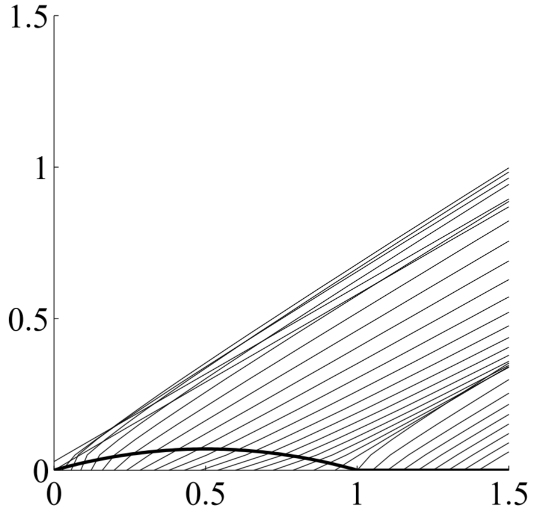

Figure 1.2 : Characteristics generated by ellipsoid body Timothy2012

The author also concluded that pressure signatures from slender objects eventually formed an N-wave at far distances. On the basis of this assumption, he derived a formula to calculate the initial jump on the pressure signature called initial shock pressure rise (ISPR). Researchers used this ISPR formula with computational fluid dynamics (CFD) in their optimization studies to quantify sonic boom value in the 2000s [14].

Later, Whitham adapted his theory for non-lifting wings in his study [6]. He defined an equivalent area distribution generated by a supersonic wing. He considered this equivalent area distribution as a representation of wings with axisymmetrical objects. Since the theory was not capable of aircraft geometries that generate lift, further improvements had to be done. After 2 years, Walkden [7] published a study about the extension of this theory to lifting wings by taking into account another component of equivalent area distribution; lift. Due to the lift, the flow field around the object is disturbed such that pressure and velocity values are changed. With a convenient relation, Walkden defined equivalent area distribution due to the lift by using surface pressure distribution. Therefore, an equivalent area distribution for a whole aircraft geometry consists of two main components; volume and lift. Figure 1.3 shows an example distribution for the equivalent area components of a low-boom aircraft.

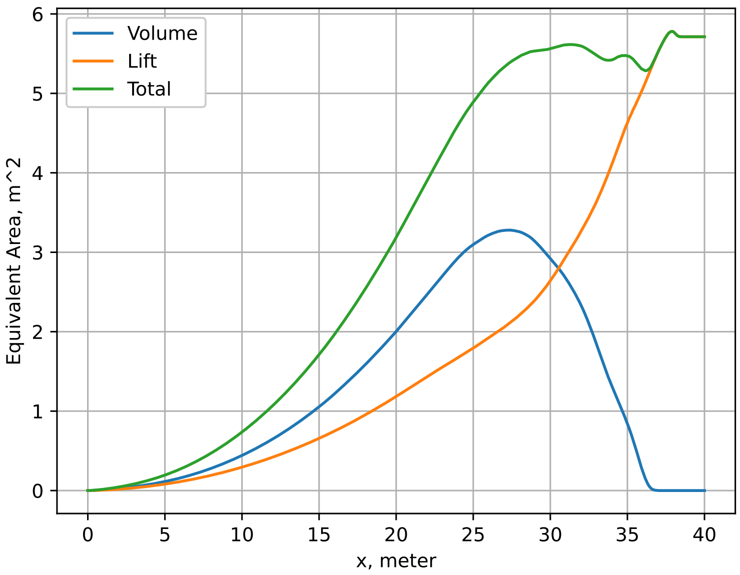

Figure 1.3 : Equivalent area components of a low-boom aircraft

The sonic boom theory was still not practical to predict a sonic boom signature from a supersonic aircraft. This theory required a continuous equivalent area distribution which was not the case for most aircraft geometries. In 1948, Lighthill [21] published a study for the extension of the linear theory to axisymmetrical objects that had discontinuous cross-section distribution. He used Heaviside calculus with the Bessel function of the second kind to define and solve F-function integral. Therefore, this study could be adapted into the sonic boom theory for geometries whose equivalent area distribution was discontinuous. In the 1980s, Gottlieb and David [22] examined and compared Whitham's and Lighthill's methods and showed the advantage of using Lighthill's method. Lighthill's method is also implemented in this thesis study to calculate pressure signature from the equivalent area distribution in Section 2.

Another issue with the modified linear theory is the assumption of a uniform medium. It assumes ambient properties such as temperature and pressure are constant. This assumption limits the usage of this theory in the real atmosphere since pressure and temperature values are changing with altitude. There are three main assumptions for the atmosphere; homogeneous, isothermal, and real atmosphere in sonic boom research. To address this issue, researchers tried to adapt the sonic boom theory to a non-homogeneous atmosphere in the 1960s. Mclean [23] made a modification on this, replacing Whitham's reference pressure with the geometric mean pressure on the ground and at flight altitude. Thus, atmospheric changes during wave propagation were also taken into account.

He also concluded that "*The results indicate that if certain effective area distributions can be achieved by real airplanes, sonic-boom overpressures much lower than those predicted by current asymptotic methods would be possible at critical transonic acceleration conditions.*" Instead of assuming an N-wave on the ground, he realized that a non-homogeneous atmosphere may lead to a non-asymptotic pressure signature. According to Whitham's ISPR formula, geometric changes can only lead to the magnitude of the initial pressure rise, not the shape of the signature. This reveals the importance of atmospheric assumptions for sonic boom propagation. After Mclean's studies, Seebas [2] and Hayes [24] improved non-homogeneous atmosphere to stratified atmosphere with custom profiles instead of isothermal atmosphere profiles.

Up to this point, sonic boom prediction can be considered a solution to the modified linear theory. However, with the use of real atmosphere, the calculation process can be broken down into three main points; near-field solution, mid- or far-field solution, and loudness calculation on the ground. Until the 1990s, researchers used equivalent area distribution and linear theory to calculate a pressure signature near the aircraft. Since equivalent area distribution requires pressure distribution on the surface of the aircraft, a pressure distribution calculated by a more advanced tool can be used directly without changing the propagation method. In this regard, researchers started to implement computational fluid dynamics (CFD) tools into the sonic boom prediction by calculating equivalent area distribution in the early 1990s. This method was first addressed by Cheung et al. [25] and Page and Plotkin [26]. They also provided a comparison with experimental results for the near-field signature calculation for various geometries such as projectile, wing, and wing-body combinations. Nikbay [27] provided an extensive use of CFD in the sonic boom minimization. Later, researchers continued to use this method for sonic boom research [28, 29].

Another improvement in the sonic boom theory was made for atmospheric propagation. In the case of a stratified atmosphere, the path of sonic boom waves changes by refraction. Variation in ambient values such as pressure and temperature results in a change in the speed of sound. Variation in the speed of sound changes the shape of the path from a straight line to a horn-shaped curve. Therefore, calculating the trajectory of the sonic boom waves, called rays, by considering random profiles is essential [30, 31]. The most common solution to overcome this issue is the implementation of geometric acoustics for wave propagation [32]. Likewise, in optics, Snell's law can be utilized to calculate the change in the path of sonic boom rays. Snell's law can be applied to each transformation between the layers of the atmosphere numerically. This technique is called ray tracing [33].

The first robust computer program which took account of the stratified atmosphere by ray tracing was developed by Hayes et al. [24]. They used Whitham F-function method for the calculation of near-field pressure signature. Then, they applied nonlinear aging and the equal area rule which are explained in Section 2 to distort the pressure signature. For wave propagation, the ray tracing technique was implemented in that computer program which was called Aeronautical Research Association of Princeton (ARAP) computer code. They broke down the problem into two main reference frames; aerodynamics and acoustics. An illustration which is taken from [2] is provided in Figure 1.4.

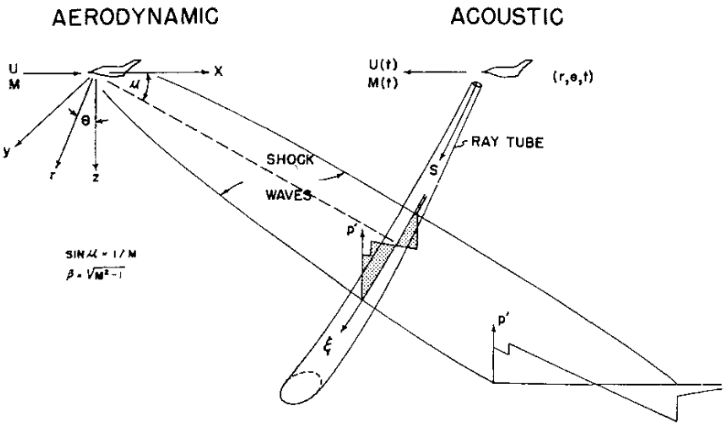

Figure 1.4 : Aerodynamics and acoustics frame of references [2]

The final study which should be mentioned in the content of classical methods is Thomas' Waveform Parameter Method (WPM) [34]. This method is based on the same fundamental theory as Whitham F-function. However, the pressure signature is divided into several segments and identified with three parameters called waveform parameters. This method eliminates the need for the equal area rule to distort the pressure signature. Also, ray tracing can be used with WPM for a real atmosphere.

Later, Thomas' study evolved into NASA PCBOOM sonic boom prediction tool [35]. Plotkin [36] published an extensive overview of classical sonic boom theory in 1989.

1.2.2 Nonlinear methods

Even though sonic boom prediction is a field of research in itself, it can be considered as a sound wave propagation problem, basically. For the simplest form, sonic boom propagation is a spherical sound wave spreading (Mach cone shape in reality) generated by a supersonic aircraft. However, wave amplitude is much higher than a normal sound wave. To specify, the sonic boom problem is nonlinear wave propagation in a relaxing gas with a moving medium [37–42].

Even though the main nonlinearity is caused by wave distortion, several cumulative effects such as thermoviscous attenuation and molecular relaxation can become important nonlinear factors during wave propagation for far distances. Here, the nonlinear term stands for these cumulative effects which are not taken into account in classical methods.

As mentioned in the previous section, characteristic curves can intersect and form a shock wave during wave propagation. In modified linear theory, the shock rise time is zero which is a non-physical solution. By considering thermoviscous attenuation and molecular relaxation, we can calculate shock rise time which is an essential parameter for loudness calculation.

In the early 1970s, researchers started to use practical implementation with vibrational relaxation and thermoviscous attenuation in sonic boom modeling. Pestorius [43] developed an algorithm to take into account dispersion and absorption during wave propagation in addition to wave distortion. First, the algorithm uses lossless propagation identical to the modified linear theory. Then, absorption and dispersion are applied by transferring the solution into the frequency domain. This algorithm requires small step sizes. To overcome the multi-valued solution, weak shock theory was utilized.

Following Pestorius' work, Anderson [44] added thermoviscous absorption into the solution. By using thermoviscous absorption, the solution algorithm does not have to rely on weak shock theory to prevent a multi-valued solution. Thermoviscous absorption smoothes the waveform with shocks by keeping the step size small. Later, this study was extended by Orenstein [45] with the molecular relaxation process. They demonstrated this application for N-waves to examine sonic booms.

In 1991, Robinson [46] combined weak shock theory and linear absorption and dispersion. Before transferring to the frequency domain, this algorithm does not require a small step thanks to weak shock theory. Instead of preventing multi-valued waveforms with small step sizes, the equal area rule was implemented in case of non-physical results. This solution was also performed in the frequency domain. The algorithm was formed into a computer program called ZEPHYRUS.

The first algorithm fully relying on the time domain solution was addressed by Cleveland [47]. He explained numerical difficulties with the frequency domain solution in his thesis. He provided a derivation of the augmented Burgers equation by ranking from governing equations of the relaxing flow. In his study, the augmented Burgers equation was solved in a horn-shaped ray tube domain calculated by geometric acoustics. Dynamic step size was introduced to prevent multi-valued waveform. During the numerical solution from the aircraft to the ground, an algorithm monitors the maximum allowable step size and controls it. The solution algorithm solves the dimensionless equation in retarded time frame. The operator-splitting method is implemented for the numerical solution. This method allows solving each term in the equation individually. While the analytical solution is used for nonlinear distortion term such as Poisson solution, thermoviscous absorption and multiple molecular relaxation terms are solved with the Crank-Nicolson method. He also implemented stratification and geometric spreading into the equation to be solved analytically. This program was named THOR by Cleveland. In 1996, Cleveland published a comparison study for the state-of-art sonic boom programs to evaluate accuracy and solution time [48].

Following Cleveland's work, sonic boom modeling was performed with the numerical solution of the augmented Burgers equation in the ray tube domain [49–54]. In 2011, Sriram [55] published his study titled *Advanced Sonic Boom Prediction Using the Augmented Burgers Equation*. He developed a sonic boom prediction program in the Fortran language called sBOOM. sBOOM is widely used for both sonic boom prediction and optimization studies. This program has the same basis as Cleveland's THOR program, except for the aircraft maneuver. With a modification of the initial wave normal's equation during the ray path calculation [24], the effect of aircraft maneuvers such as acceleration, pitching, and turning can be taken into account. This program also can be run with custom atmosphere profiles for pressure, temperature, humidity, and horizontal wind.

1.2.3 Further studies in sonic boom research

All the sonic boom studies addressed in the previous section are based on geometrical acoustics that was first applied by Hayes [24]. As explained in Section 2, geometrical acoustics methods are based on a linear theory that is valid for non-horizontal rays. As the rays reach a horizontal position due to atmospheric stratification, the ray tube area is formed by four adjacent rays goes to zero. This led to a singularity in the numerical solution. Another restriction from linear geometric acoustics is the effect of vertical wind. During the ray tracing solution, only horizontal wind can be taken into account. Therefore, the atmospheric turbulence can not be examined with a sonic boom program based on linear geometric acoustics. In addition, due to the one-dimensional solution of the augmented Burgers equation, self-refraction during propagation can not be calculated.

To address the effect of atmospheric turbulence on the sonic boom and self-refraction, researchers tried to solve the sonic boom problem with Khokhlov-Zabolotskaya-Kuznetsov (KZK) equation [56, 57]. This equation is an extended version of the augmented Burgers equation into 2-dimension.

Extension of sonic boom prediction to a higher fidelity method was presented by Yamashita and Suzuki [58–60]. They studied sonic boom prediction by solving Euler equations with an adaptive grid strategy. Molecular relaxation was combined with Euler equations in the 3-dimensional domain from the aircraft to the ground. Also, an improved version of the full-field simulation was presented by Qiao et al. [61] to study the effect of atmospheric turbulence.

When the rays generated by the aircraft reach ground with various azimuth angles form a hyperbolic carpet called primary carpet. Rays that have higher azimuth angles can deflect to a horizontal position before reaching the ground and follow a trajectory toward to upper atmosphere. Due to the stratification, these rays reflect back to the ground and form an outer carpet on the ground called a secondary carpet. This phenomenon is illustrated in Figure 1.5 by Locey [3]. Several studies on the secondary sonic boom can be found in literature [62, 63]

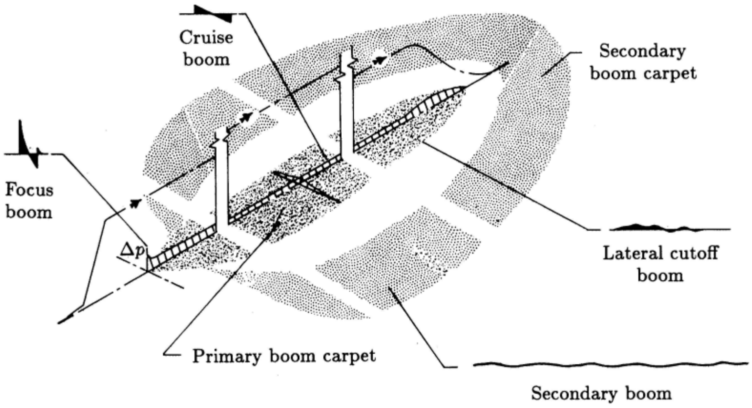

Figure 1.5 : Secondary sonic boom carpet [3]

The final topic beyond the scope of this study is focusing. During the aircraft's acceleration, adjacent rays can overlap during the ray tracing calculation and lead to a singularity for the methods presented in this study. The linear geometric acoustics method predicts an infinite amplitude at caustics, therefore a special treatment must be considered [64].

1.3 AIAA Sonic Boom Prediction Workshops

The American Institute of Aeronautics and Astronautics (AIAA) organized workshops focused on sonic boom prediction. Four sonic boom prediction workshops (SBPW) were organized in 2014, 2017, 2020, and 2022 [4], respectively. They defined 3 cases in each SBPW such that these cases cover several challenging computational problems in sonic boom research. Results for specified cases from participants were published by Park and Morgenstern [65], Rallabhandi and Loubeau [66, 67]. These results were generated by participants' sonic boom prediction tools. Figure 1.6, 1.7, and 1.8 show 3 models provided in the first, second and third SBPW, respectively [4]. The model in Figure 1.8 is named NASA C608 and later involved X-59 low-boom demonstrator.

Figure 1.6 : LM1021 model from SBPW-1 [4]

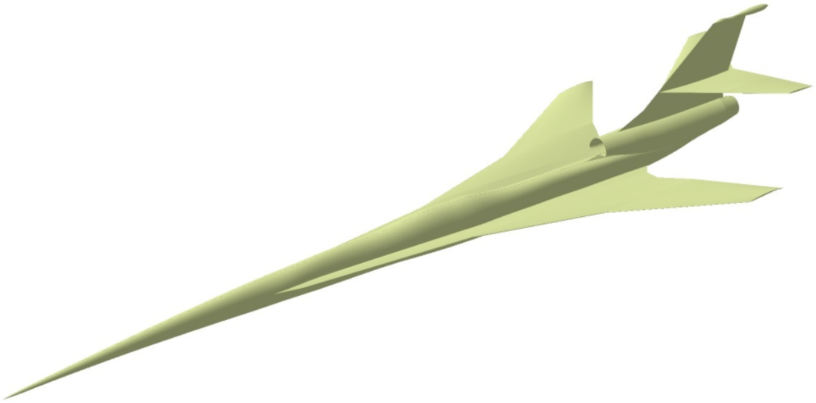

Figure 1.7 : NASA C25D model from SBPW-2 [4]

In addition to the AIAA SBPW, several sonic boom workshops and conferences were held by NASA in the past. In 1994 and 1995, two sonic boom workshops were organized titled *High-Speed Research Program Sonic Boom Workshops* focused on sonic boom prediction, low-boom aircraft design concepts, sonic boom minimization, and testing [68–70]. In 1967 and 1968, the first and second sonic boom conferences were held to present current sonic boom research in terms of theory and experiment, and examine the possibility of reduction of sonic boom overpressure [71, 72].

Figure 1.8 : NASA C608 from SBPW-3 [4]

1.4 Low-Boom Aircraft Design And Optimization Studies

Sonic boom minimization is essential to achieve the goal of supersonic civil transport over land. As sonic boom prediction methods have been developed over the years, researchers also investigated to find a way to reduce sonic boom overpressure. Sonic boom minimization research dates back to 1960s as Jones [73] tried to find a lower bound for the sonic boom overpressure by using specific F-functions such as those generated by wings that have a uniform or elliptical lift distribution in a straight flight. Seebas and George [74] extended sonic boom minimization theory that was not restricted to the far-field by using F-function. In this study, Seebass and George used an F-function characterization with an effective area distribution that had an infinite slope at the nose called nose-bluntness. Nose-bluntness prevents strong shock coalescence at the front of the signature while increasing drag in the supersonic regime. These studies were based on the assumption of a uniform atmosphere. Also, the stratified atmosphere was taken into account by George and Plotkin [75]. Later, Darden [76] extended this study to include nose-bluntness relaxation in a real stratified atmosphere. After these studies, the sonic boom minimization theory that used F-function characterization was called Jones-Seebass-George-Darden (JSGD) theory by Seebass and George [77].

As the CFD has become a practical tool with the advance in computational power, researchers started to implement shape optimization techniques for sonic boom minimization. In the earlier of 2000s, Nikbay [27] developed an optimization framework by using shape optimization to reduce ISPR. She studied Lockheed

Martin's Point of Departure supersonic aircraft designed for the DARPA's Quiet Supersonic Platform (QSP) program. By using free-form deformation (FFD), the surface of the aircraft can be deformed according to FFD points. After each deformation, an equivalent area distribution can be generated by using surface slicing to calculate ISPR with Whitham's formulation. She also examined "freezing" in the sonic boom signature during propagation with the lobe-balancing technique for F-function. In the following years, several design and optimization studies that utilized high-fidelity analysis tools were published for a supersonic airliner or business jet [14, 15, 78–83].

In 2008, Maute et al. [84] implemented an adjoint methodology for Shaped Sonic Boom Demonstration (SSBD) aircraft to reduce ISPR. Following that, Rallabhandi [85] published his study based on the adjoint methodology of sonic boom minimization. He derived adjoint equations for the numerical solution of the augmented Burgers equation. In 2011, Li and Shields [86] published a study for the generation of a target equivalent area distribution to be used in optimization studies. This target equivalent area distribution can be generated by using the required lift and volume constraints. The whole distribution is represented by a B-spline curve to obtain a smooth shape. Later, Li and Rallabhandi [87] implemented an inverse design method for sonic boom minimization by using the reversed equivalent technique. In this method, an equivalent area can be obtained by pressure signature calculated by CFD in the near-field by using reverse formulation. Then, they used the augmented Burgers equation for an inverse propagation from the near-field pressure signature location to the aircraft axis. This technique increases the fidelity of the equivalent area distribution by considering the nonlinear flow structure in the solution 3D domain, unlike surface slicing. Recently, Li and Geiselhart [88, 89] published their study funded by the NASA Commercial Supersonic Technology Project for the design of a supersonic airliner that carries 40 passengers. They studied two different conditions such as overwater and overland (low-boom).

A comprehensive report titled '*Sonic Boom: Six Decades of Research*' published by Magieri et al. [90] in 2014 on the research of sonic boom at NASA Langley Research Center. Those interested in learning more about sonic boom research can refer to this report.

2. METHODOLOGY

In this section, the methodologies employed in this thesis are explained. First, the near-field pressure signature calculation is presented with a multi-fidelity approach which is used as an input signal for sonic boom propagation. Then, the classical sonic boom theory is discussed with its validity and importance in sonic boom studies. Next, the derivation of the nonlinear wave propagation equation in a non-homogeneous medium is provided. Finally, noise metrics and perceived loudness calculations are derived.

2.1 Multi-Fidelity Near-Field Flow Solution

In the sonic boom theory, a supersonic aircraft is assumed as a moving acoustic source that creates pressure waves. Therefore, to solve wave propagation in the atmosphere, a near-field pressure signature must be obtained near the aircraft. A diagram that illustrates the sonic boom propagation process is shown in Figure 2.1. Due to the spherical source assumption in the sonic boom calculations as mentioned in Section 2.2, this near field pressure signature must be computed at least 2 or 3 body lengths away from the aircraft to be used as an input signal in the propagation. In this regard, accurate prediction of near-field pressure signature is essential for the sonic boom loudness calculation. Even though computational fluid dynamics has been widely used to obtain near-field flow solutions, low-fidelity tools can be preferred in design and optimization studies [88,91–93]. In the following section, the theory of the low-fidelity methods, especially panel methods are elaborated. Then, the use of the CFD for the supersonic flow solution in the sonic boom prediction is explained.

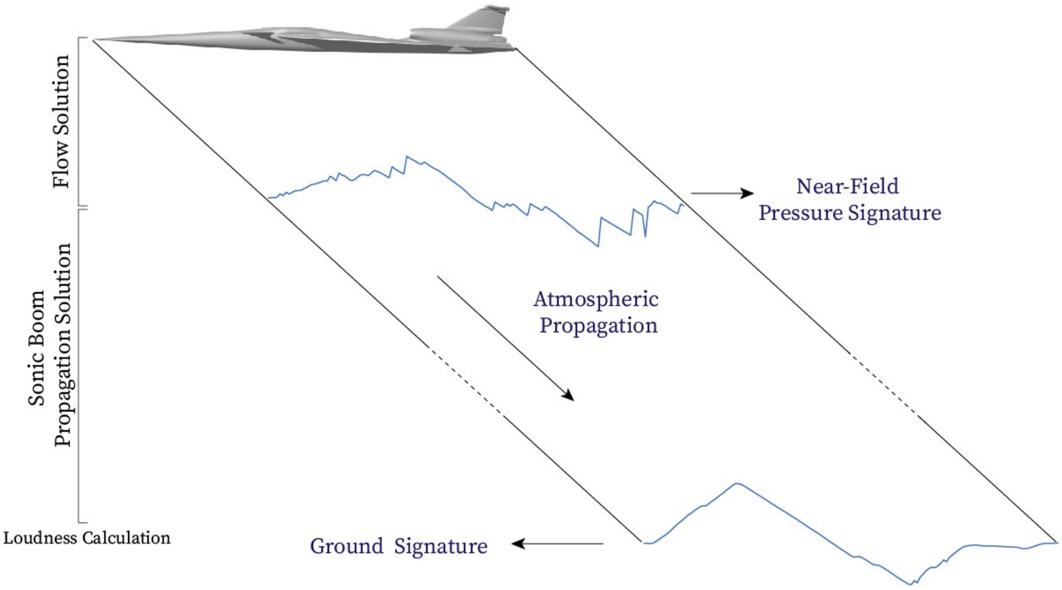

Figure 2.1 : Sonic boom calculation diagram

2.1.1 Low-fidelity flow solution, panel methods

There are various methods in the literature to predict supersonic flow around slender bodies at moderate angles of attack. As mentioned in Section 2.2, pressure distribution on the surface of the aircraft is required to calculate an equivalent area distribution. Therefore, these low-fidelity tools must provide a pressure distribution in addition to the aerodynamic coefficients. Jung [8] used a low-fidelity flow solution that assumed a uniform lift distribution over the lifting surface. In this thesis study, the three-dimensional panel method is preferred due to the advantage of dealing with arbitrary objects. The theory behind panel methods is explained as follows.

Linearized potential flow is the fundamental theory of the panel methods. The governing equation of the linearized potential flow is called the Prandtl-Glauert equation, given in equation (2.1), derived from small-perturbation theory.

$$\left(1-M_{\infty}^{2}\right)\hat{\phi}_{xx}+\hat{\phi}_{yy}+\hat{\phi}_{zz}=0 \tag{2.1}$$

where $\hat{\phi}$ is the perturbation velocity potential, M is the Mach number, and subscripts x, y, z are the Cartesian coordinates. This equation is derived with the assumption of slender bodies and moderate angles of attack in subsonic and supersonic regimes [94]. To solve equation (2.1) numerically on the surface of the aircraft, the singularity method can be utilized. Several singularity types such as source, vortex, and doublet can be used to obtain induced velocity on the control points of the surface panels.

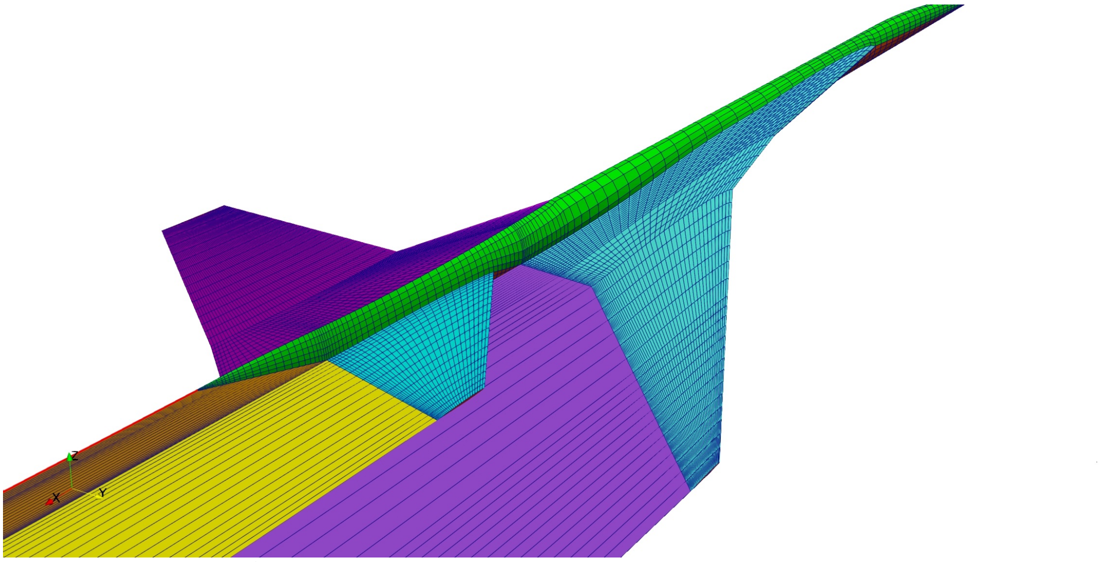

Figure 2.2 : Surface mesh of a supersonic aircraft

If Mach number is greater than 1, special treatment must be made due to the nature of the supersonic flow. Each singularity can affect the control points in its domain of influence. Therefore, a search algorithm must be used to take into account the domain of influence.

There are several codes in the literature that use panel methods to solve potential flow such as VSPAERO, XFLR5, VORLAX, etc. However, only a few computer programs are available which have the capability of the supersonic flow solution. PAN AIR [95] is one of the low-fidelity flow solvers that is widely used in supersonic aircraft design optimization and is preferred in this study. Also, there are recent studies on the topic of supersonic panel solvers [96, 97].

PAN AIR is written in the FORTRAN language and requires an input file. This input file includes flow conditions and surface mesh information. The surface mesh of each component is called the network in PAN AIR. An example of a surface mesh of a supersonic aircraft is illustrated in Figure 2.2. There are several options to be selected in PAN AIR for the surface boundary condition. In this study, a supersonic solid surface boundary condition is selected for the analysis. In addition to the surface networks, wake networks placed behind the lifting surfaces must be defined. These wake networks are illustrated with yellow and purple colors in Figure 2.2.

As PAN AIR is implemented to provide input for the sonic boom analysis, the near-field pressure signature must be obtained from the analysis. PAN AIR has an output option that enables the export of pressure coefficient on a predefined line segment which is called off-data points. This line must be placed in the flow direction and at least 2 body lengths away from the aircraft. In Figure 2.3, an example of a near-field pressure signature that is computed at 2 body length away from the JAXA Wing-Body (JWB) model [93] is provided.

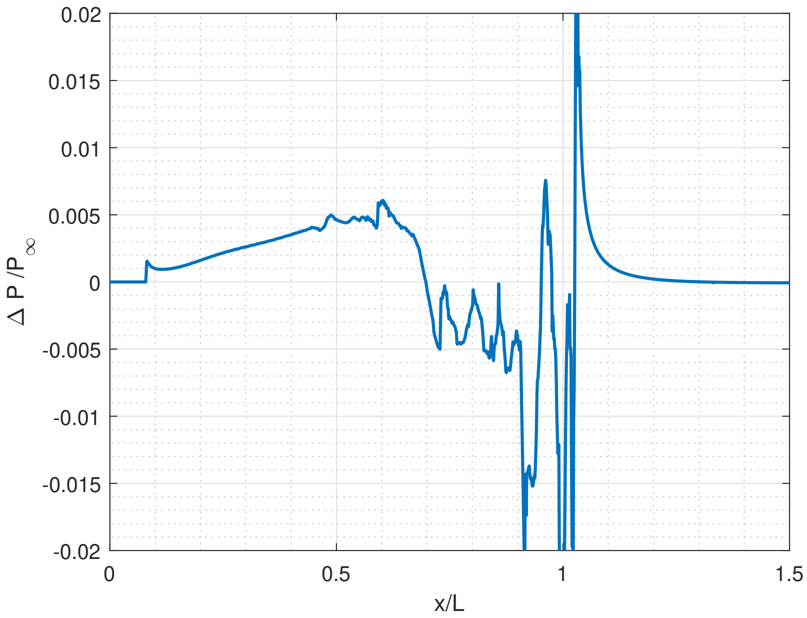

Figure 2.3 : Near-field pressure signature of the JWB model

As mentioned in Section 4, PAN AIR is integrated into a computational framework to generate low-fidelity near-field pressure data. In addition to off-data points, a VTK file can be generated from the PAN AIR analysis. This VTK file includes surface mesh and pressure coefficient distribution on this surface. Later, this VTK file will be used to calculate an equivalent area distribution.

The validity of the PAN AIR is examined in detail in [98]. Both aerodynamic coefficients and sonic boom loudness values are in the acceptable range for the initial design and optimization.

2.1.2 High-fidelity Euler solution

For the high-fidelity solution of the flow field around a supersonic aircraft, the CFD method is utilized. In this study, SU2 multi-physics solver [99] is employed for the high-fidelity flow solution. A finite volume solver is used in SU2 with a vertex-based data structure.

First, a solution domain must be generated to solve governing equations numerically. An example of a solution domain is shown in Figure 2.4.

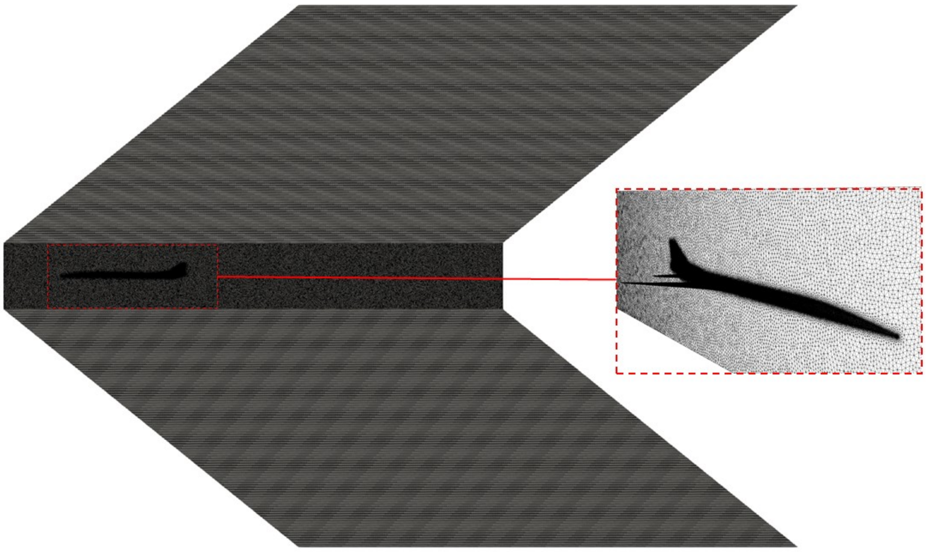

Figure 2.4 : Solution domain of the CFD analysis

As seen in the figure, the flow domain is created like a cone shape. The reason for this cone shape for the flow domain lies in the main interest of the flow solution. The near-field signature is computed at 2 or 3 body lengths away from the aircraft. This pressure disturbance propagates in the Mach cone direction from the aircraft to the far field. Therefore, a cone shape that is aligned with the Mach number is preferred to avoid unnecessary region that is not interested.

Due to the acoustic assumption requirement, the pressure signature must be computed at least 2 body lengths away from the center line of the aircraft. This requirement forces flow domain size to be relatively large compared to other cases. To avoid a huge amount of computational burden, two strategies can be utilized. First, a core region near the aircraft can be created by unstructured mesh to be able to represent the aircraft surface properly. Then, the cone shape region can be created with a structured mesh that is aligned with the Mach angle [100, 101]. The other strategy is the use of adaptive mesh refinement. In this method, the entire flow domain consists of unstructured mesh with adaptive mesh [102]. An example study that was performed by mesh adaptation is shown in Figure 2.5.

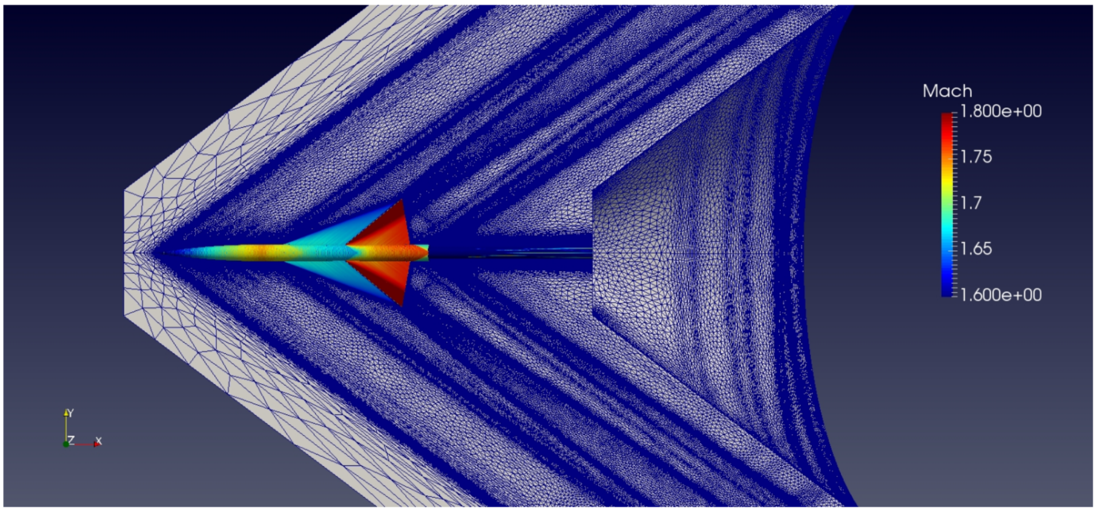

Figure 2.5 : Adaptive mesh structure created for the NASA 69^o Delta Wing Model [5]

In SU2, Euler analysis is selected for the flow solution. The governing equation for inviscid analysis is given in equation 2.2 with the differential form.

$$\frac{\partial Q}{\partial t} + \nabla \cdot \bar{F}_c(Q) = 0 \tag{2.2}$$

where Q is the conservative state vector, F_c is the convective flux vector and, t is time. Here, Q and F_c can be defined by

$$Q = \left\{ \begin{array}{c} \rho \\ \rho \bar{V} \\ \rho E \end{array} \right\} \quad \bar{F}_c = \left\{ \begin{array}{c} \rho \bar{V} \\ \rho \bar{V} \otimes \bar{V} + \bar{\bar{I}} p \\ \rho E \bar{V} + p \bar{V} \end{array} \right\} \tag{2.3}$$

In this equation system, ρ, E, p, $\bar{V}$, and $\bar{I}$ represent density, energy per mass, thermodynamic pressure, velocity vector, and identity matrix, respectively. For the calculation of the fluxes, the weighted least squares method is selected. Also, 1 or 2 level V cycle multi-grid can be utilized to accelerate convergence. Finally, Jameson-Schmidt-Turkel (JST) scheme is used in the analysis.

We performed unsteady supersonic analysis for a low-boom concept aircraft from the second SBPW which is named NASA C25D [103] in a previous study [104]. The geometry and pressure coefficient distribution for $M = 1.6$ on the symmetry plane are provided in Figure 2.6 and 2.7 respectively.

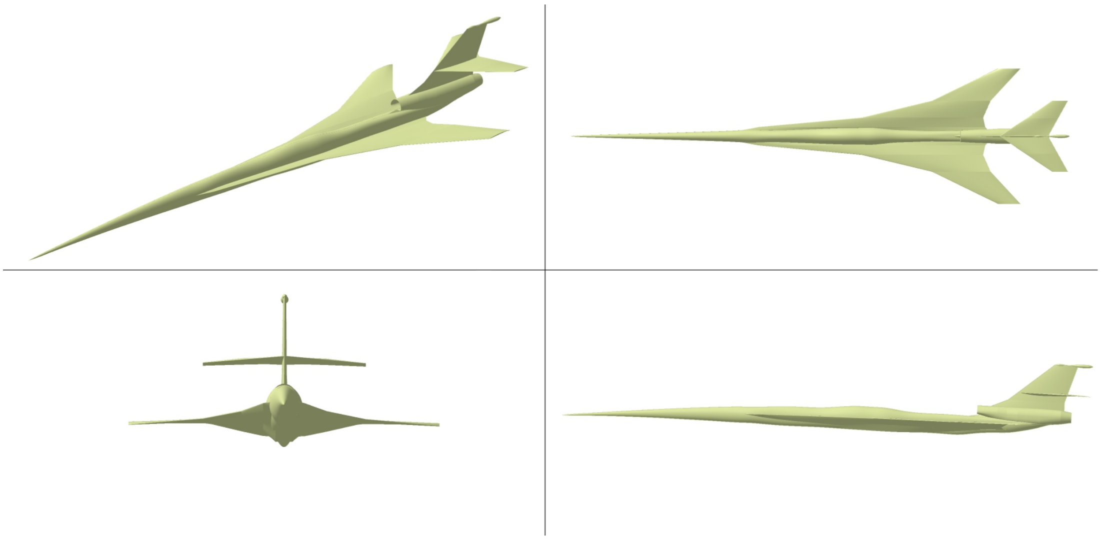

Figure 2.6 : NASA C25D aircraft render

The convergence criterion is entered as 10^{-10} for the RMS density. SU2 generates two VTK files; one for the entire flow domain and the other one for the only selected surfaces by the user. The first one is used in this study to extract pressure signatures from the flow domain.

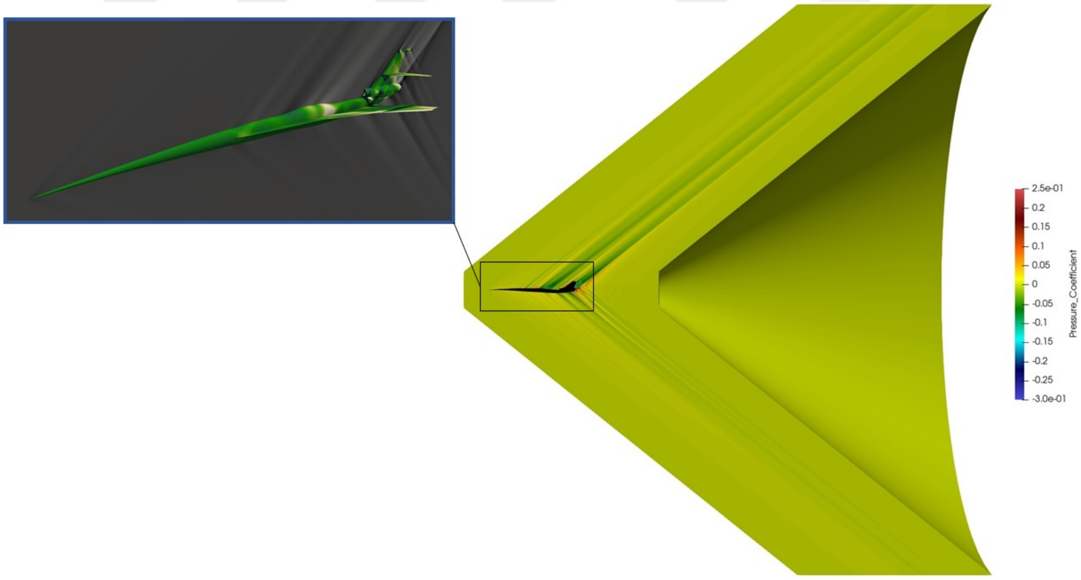

Figure 2.7 : Pressure coefficient distribution on the symmetry plane, $M = 1.6$

2.2 Classical Sonic Boom Theory

In the following subsections, the derivation of classical sonic boom theory is presented beginning from the most basic form, F-function, to the geometrical acoustics.

2.2.1 Modified linear theory

As mentioned in the previous section, governing equation of linearized flow for both subsonic and supersonic regimes is the Prandtl-Glauert equation which is given in equation (2.4).

$$\left(1-M_\infty^2\right)\hat{\phi}_{xx}+\hat{\phi}_{yy}+\hat{\phi}_{zz}=0 \tag{2.4}$$

Equation (2.4) is defined by the Cartesian coordinates. It can be transformed into the polar coordinates:

$$\phi_{rr}+\frac{\phi_r}{r}-\beta^2\phi_{xx}=0 \tag{2.5}$$

where β is the Prandtl-Glauert coefficient which can be defined as:

$$\beta=\sqrt{M_\infty^2-1} \tag{2.6}$$

Here, the linearized flow represents irrotational, steady, and isentropic flow with small perturbations. Since the linearized flow is a first-order approximation, it is not valid in the transonic and hypersonic regimes.

Due to the linearization, the linear theory is valid near the slender object by ignoring second and higher-order terms. This leads to inaccurate predictions for the flow field far from the object in the supersonic regime. More specifically, the assumption of straight and parallel characteristics in the flow field is not realistic for the far-field calculations. Whitham [18] first addressed this issue and proposed a new method by giving a modified formulation of characteristics.

2.2.1.1 Whitham's F-function

The solution of equation (2.5) can be given as:

$$\phi=\int_0^{x-\beta r}\frac{-f(\zeta)}{\sqrt{(x-\zeta)^2-\beta^2r^2}}d\zeta \tag{2.7}$$

where r is the axial coordinate away from the body axis, f is a function derived from the body shape, and ζ is a dummy coordinate in the x-axis. For this solution, characteristics in the flow field can be defined with the linear equation:

$$y = x - \beta r \tag{2.8}$$

Here, it is assumed that $\beta r \gg y$. Then, we can calculate perturbation velocities u and v as:

$$u = \frac{-1}{\sqrt{2\beta r}} \int_0^y \frac{f'(\zeta)}{\sqrt{y-\zeta}} d\zeta \tag{2.9}$$

$$v = -\beta u \tag{2.10}$$

Whitham defined an F-function such that:

$$F(y) = \int_0^y \frac{f'(\zeta)}{\sqrt{y-\zeta}} d\zeta \tag{2.11}$$

Substituting into equation (2.9) and (2.10):

$$u = -\sqrt{\frac{2\beta}{r}} F(y) \tag{2.12}$$

$$v = \sqrt{\frac{\beta}{2r}} F(y) \tag{2.13}$$

It should be noticed that r is in the denominator. Therefore, these equations can be applied far from the body. In addition to the velocities, a relation can be derived from F-function for the pressure perturbation. By using isentropic relations and energy equation, perturbation pressure can be defined as [18]:

$$\Delta p = \frac{\gamma p_\infty M_\infty^2}{\sqrt{2\beta r}} F(y) \tag{2.14}$$

The next step is to find an expression for the F-function. Here, boundary conditions can be utilized. On the surface of the slender object, we can define perturbation velocity v as:

$$v(x,r) = \frac{\partial \phi}{\partial r} = \frac{f(x)}{r} \tag{2.15}$$

On the body, we can define $R(x)$ as the radius distribution of the axisymmetrical body.

$$f(x) = Rv|_{body} \tag{2.16}$$

Since the flow must be tangent on the surface with respect to the body:

$$R' = \frac{v|_{body}}{1 + u|_{\text{body}}} \approx v\Big|_{\text{body}} \tag{2.17}$$

By using these two equations, we can define f, the source strength, as:

$$f(x) = vR(x) = R'(x)R(x) = \frac{S'(x)}{2\pi} \tag{2.18}$$

Here, S is the cross-sectional area distribution along the body. By differentiation;

$$f'(x) = \frac{1}{2\pi}S''(x) \tag{2.19}$$

This can be substituted into equation (2.11). Then, we can obtain a relation for F as:

$$F(y) = \int_0^y \frac{S''(\zeta)}{\sqrt{y-\zeta}}d\zeta \tag{2.20}$$

This refers to Whitham's F-function. Since it requires S'' in the integral term, area distribution must be continuous along the x-axis. A sample F-function calculation for a projectile is illustrated in Figure 2.8.

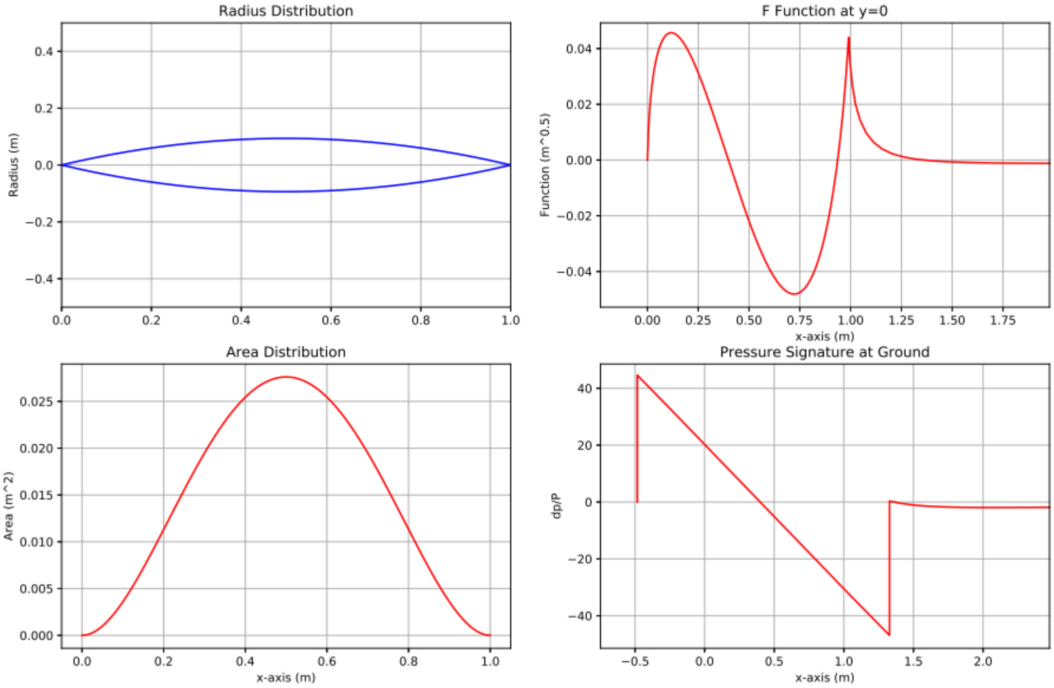

Figure 2.8 : F-function calculation of a projectile

As seen in the right-upper figure, F-function has an asymptotic behavior as y goes to infinity. This projectile is an axisymmetric body with continuous area distribution. However, the F-function method must be applied to objects that have non-axisymmetric shapes. Therefore, the extension of Whitham's F-function to the non-axisymmetric bodies is provided in the following section.

2.2.1.2 Equivalent area distribution

In equation (2.20), S'' term must be calculated to find F-function. The equivalent area distribution concept is addressed here to define S'' for bodies that are non-axisymmetric. The area distribution can be divided into two components:

$$S_{\mathrm{eq}}(y) = S_L(y) + S_V(y) \tag{2.21}$$

Where S_L is the lift contribution and S_V is the volume contribution to the equivalent area. Whitham [6] addressed the extension of F-function for the wings that are non-axisymmetric geometries. He formulated an equivalent body of revolution that represents the wing itself. He calculated the cross-sectional area of the wing at slices and took a projection of them onto the plane perpendicular to the streamwise direction. An independent variable, η, is used to define the leading edge as the distance from the centerline. $l(\eta)$ is the dependent variable in the direction of the x-axis. According to Whitham, the wavefront is a surface generated by PM where M lies on the Mach cone as P moves along AB in Figure 2.9.

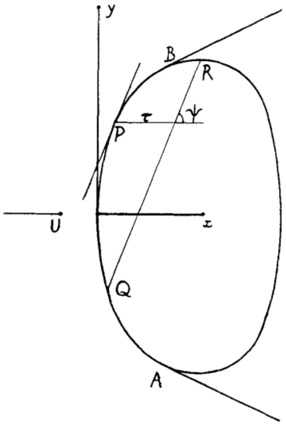

Figure 2.9 : Wing construction lines, taken from [6]

Here, the Mach cone is defined as:

$$(x - l(\eta))^2 = \beta\left((y-\eta)^2 + z^2\right) \tag{2.22}$$

Taking the derivative of both sides:

$$\frac{l'(\eta)}{\beta} = \frac{\beta(y-\eta)}{(x - l(\eta))} \tag{2.23}$$

It is assumed that $z = 0$. This is the equation of plane $(l(\eta), \eta)$ which is parallel to the z-axis and has an angle of $\tan^{-1}\left(l'(\eta)/\beta^2\right)$ with respect to the x-axis. He defined a coordinate system such that:

$$\begin{aligned} x &= x \\ y &= \eta + r\cos\theta \\ z &= r\sin\theta \\ \tau &= x - l(\eta) - \beta r \end{aligned} \tag{2.24}$$

τ is the distance between the point of interest and the leading edge. Therefore, the potential from the wing is:

$$\phi(x,y,z) = -\frac{1}{\pi}\iint \frac{Z_x(x_i,y_i)}{\sqrt{(x-x_i)^2 - \beta^2\left((y-y_i)^2 + z^2\right)}} dx_i dy_i \tag{2.25}$$

Here, $Z_x(x_i,y_i)$ is the thickness distribution of the wing.

Later, Walkden [7] adopted the lift contribution of non-symmetric bodies by using superposition. He used to the same geometry without thickness as shown in Figure 2.10.

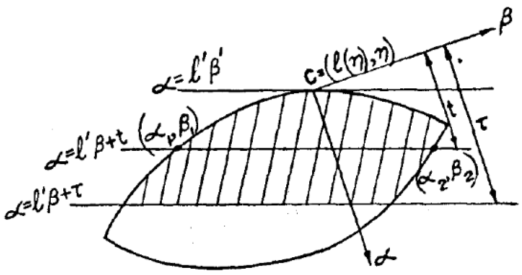

Figure 2.10 : Wing construction lines, taken from [7]

Similar to Whitham's method, Walkden assumed a supersonic leading edge and used construction lines parallel to the leading edge. First, Walkden used a flat plate potential function as:

$$\phi(x,y,z) = \frac{1}{4\pi}\iint \frac{z(x-x_i)}{(y-y_i)^2 + z^2} \frac{c_L(x_i,y_i)}{\sqrt{(x-x_i)^2 - \beta^2\left((y-y_i)^2 + z^2\right)}} dx_i dy_i \tag{2.26}$$

The lift distribution can be represented as an equivalent area distribution as follow.

$$S_L(t) = \frac{\beta\cos\phi}{2}\int_0^t \int_{\beta_{W1}}^{\beta_{W2}} c_L(\alpha, \beta_W)\, d\beta_W\, d\alpha \tag{2.27}$$

Here, the limit of integration must be determined according to the domain of influence. To simplify, following relations can be used.

$$r^2 = (y - y_i)^2 + z^2 \tag{2.28}$$

$$\frac{-z}{r} = \cos\phi \tag{2.29}$$

$$\frac{x - x_i}{r} = \frac{-z}{r\tan\theta_1} = \frac{\cos\phi}{\cos\phi\tan\mu} = \beta \tag{2.30}$$

Then:

$$\phi(x, y, z) = -\frac{\beta}{4\pi}\cos\phi \iint \frac{\Delta C_p(x_i, y_i)}{\sqrt{(x - x_i)^2 - \beta^2 r^2}} dy_i dx_i \tag{2.31}$$

Where ΔC_p is:

$$\Delta C_p = \frac{p_{\text{lower}} - p_{\text{upper}}}{q} \tag{2.32}$$

From the previous definition of the potential function:

$$\phi = \int \frac{-f(x_i)}{\sqrt{(x - x_i)^2 - \beta^2 r^2}} dx_i \tag{2.33}$$

Combining these equations leads to the following relation for the general lift contribution on area distribution.

$$S_L(x) = \frac{\beta\cos\phi}{2q} \iint L(x_i, y_i)\, dy_i dx_i \tag{2.34}$$

To perform this integration, the limits must be specified as mentioned. Since the domain of influence is the Mach cone shape for a point on the surface of the aircraft or the wing, the intersection between the Mach plane and geometry along the y-axis can be calculated on the several slices as shown in Figure 2.11.

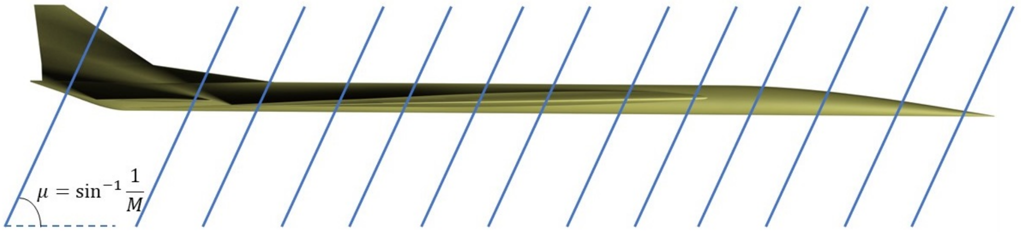

Figure 2.11 : Slicing of the aircraft surface

The orientation of each slice must be aligned with the Mach angle defined as $\sin^{-1}\frac{1}{M}$. The calculation algorithm of the equivalent area distribution from slicing is explained in Section 3. A sample area distribution calculated for a lifting wing-body configuration is provided in Figure 2.12.

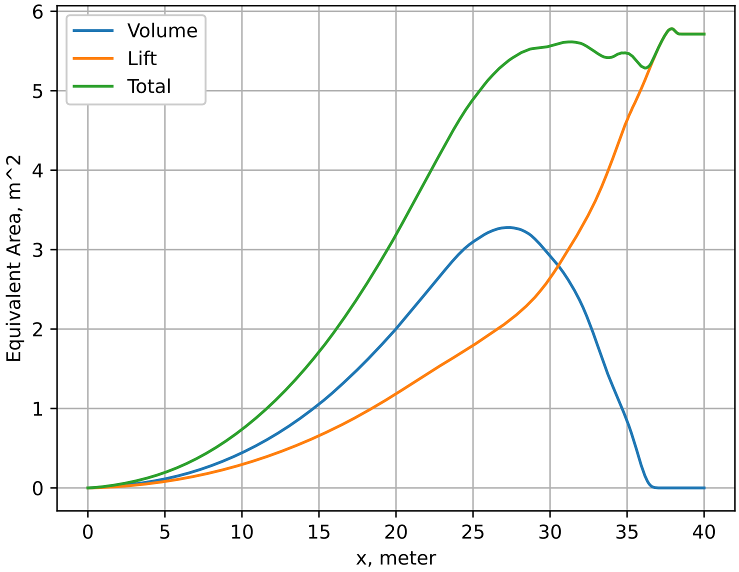

Figure 2.12 : A sample equivalent area distribution

According to the given formulation, the total area distribution must be continuous to define the second derivative term in the F-function formula. For the practical usage of F-function, this assumption must be eliminated as the aircraft geometries may have discontinuous area distribution. The extension of Whitham's F-function to the non-smooth discontinuous area distribution is presented in the following section.

2.2.1.3 Lighthill's F-function

Lighthill [21] published a study for the calculation of F-function for the discontinuous bodies. The following relation was provided.

$$F(y) = \int_0^\infty \sqrt{\frac{2}{\beta R(\zeta)}}\, h\left(\frac{y-\zeta}{\beta R(\zeta)}\right) \frac{dS'(\zeta)}{2\pi} \qquad \textbf{(2.35)}$$

where:

$$h(\chi) = \sqrt{\frac{\pi}{2p}} \frac{1}{K_1(p)} H(\chi) \qquad \textbf{(2.36)}$$

Here, H is the Heaviside function and K_1 is the Bessel function of the second kind. Even though this solution was considered expensive with the computational power in the 1980s [105], it takes seconds to solve with the current computers. Therefore, this formulation is implemented in this study to handle discontinuous geometries. A comparison of Whitham's F-function and Lighthill's F-function is illustrated in Figure 2.13. In the figure, there are 4 different functions consisting of different numbers of points. As the number of points that are used for the representation of the F-function increases, the validity of Whitham's F-function decreases.

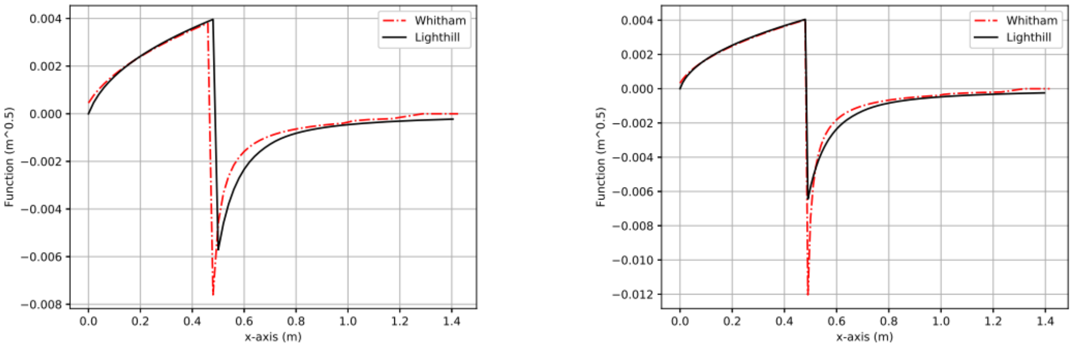

(a) N=50

(b) N=100

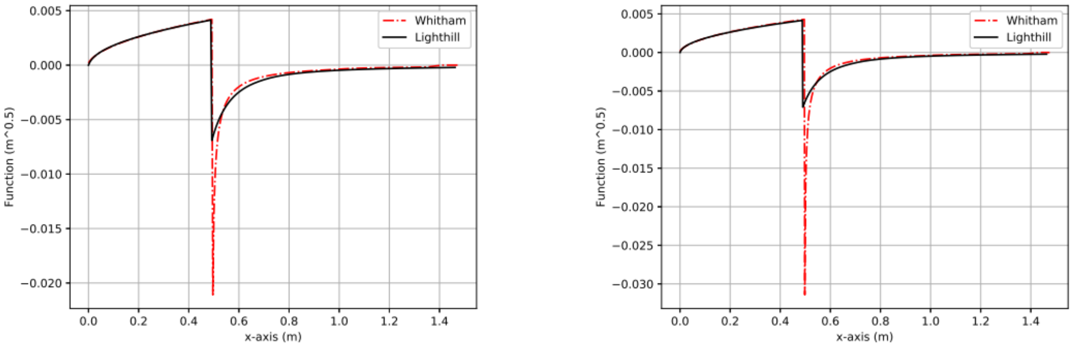

(c) N=250

(d) N=500

Figure 2.13 : Comparison of Whitham's and Lighthill's F-functions

An example of F-function calculation for a discontinuous shape is provided in Figure 2.14.

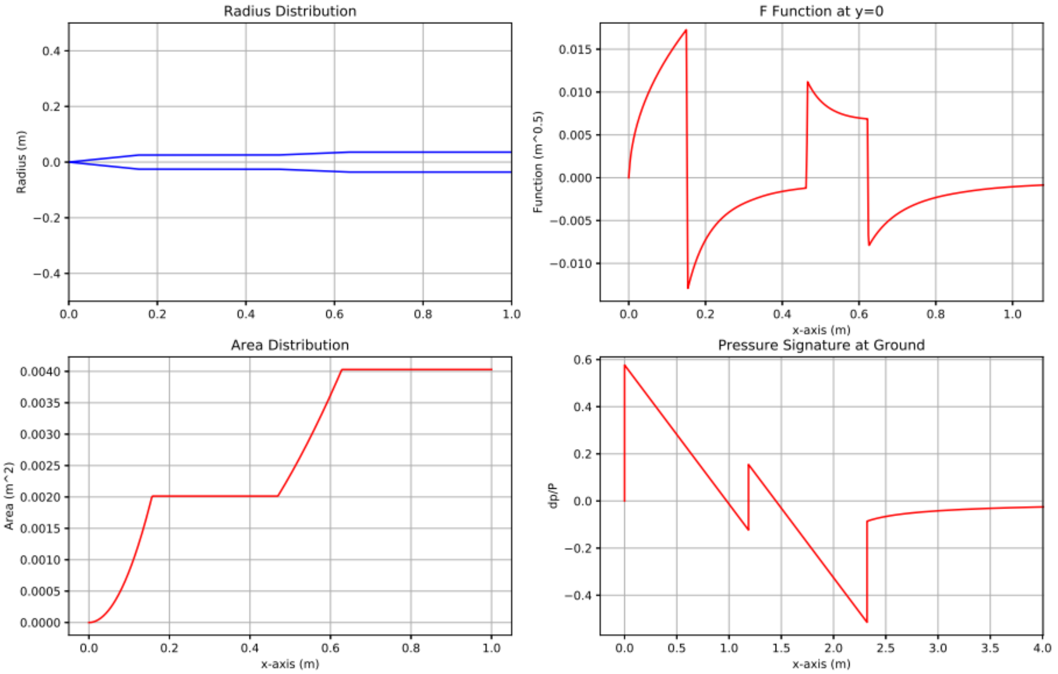

Figure 2.14 : F-function of a discontinuous body

2.2.2 Signal distortion

The F-function that is calculated by using equivalent distribution is defined at the central axis of the aircraft. In other words, F-function represents a kind of acoustics source distribution along the x-axis. To obtain a pressure signature far from the body, this F-function must be propagated by using the characteristic relation. According to the modified theory, the following equation can be used to define characteristic curves.

$$y = x - \beta r + \frac{(\gamma+1)M^4}{\sqrt{2\beta^3}}\sqrt{r}F(y) \tag{2.37}$$

As the axial distance r increases, the F-function is distorted as shown in Figure 2.15. The amount of distortion for a point depends on the value of the F-function at that point.

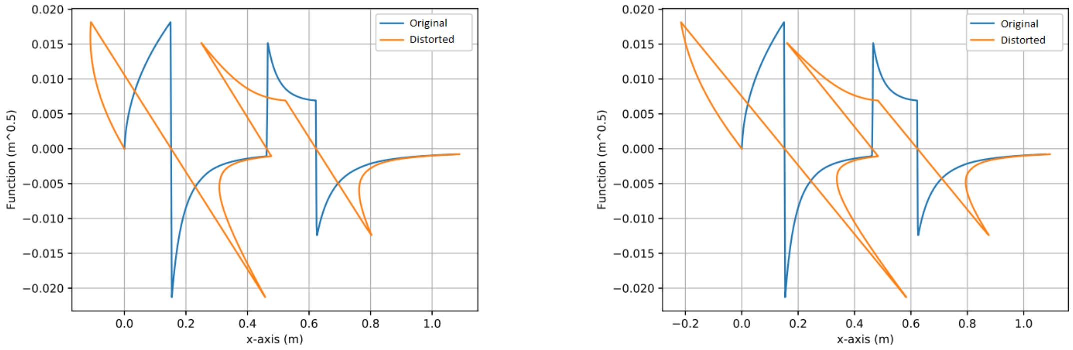

(a) $r = 5$

(b) $r = 10$

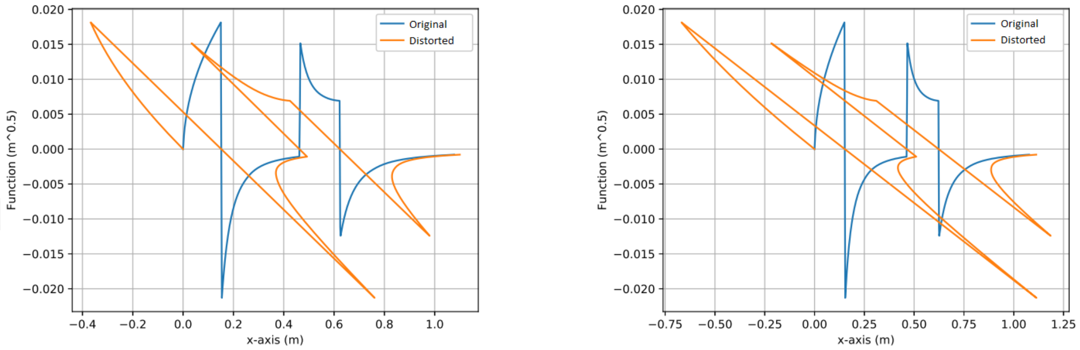

(c) $r = 20$

(d) $r = 50$

Figure 2.15 : F-function distortion

Since characteristic curves are no longer parallel straight lines, they can intersect as r goes to infinity as shown in Figure 1.2. This is also observed in Figure 2.15. To prevent a multi-valued non-physical result, the weak shock theory [37] can be utilized. According to the weak shock theory, when characteristics merge, a shock wave is formed with a slope of an average of the merging characteristic's slopes. This can be also related to the wave speed of the shock wave such that the speed of the shock is the average of the merging characteristics' speed. In other words, a shock wave can be placed in the F-function where the area of the right and left sides are equal in the multi-valued region. This method is called the equal area rule and is illustrated in Figure 2.16.

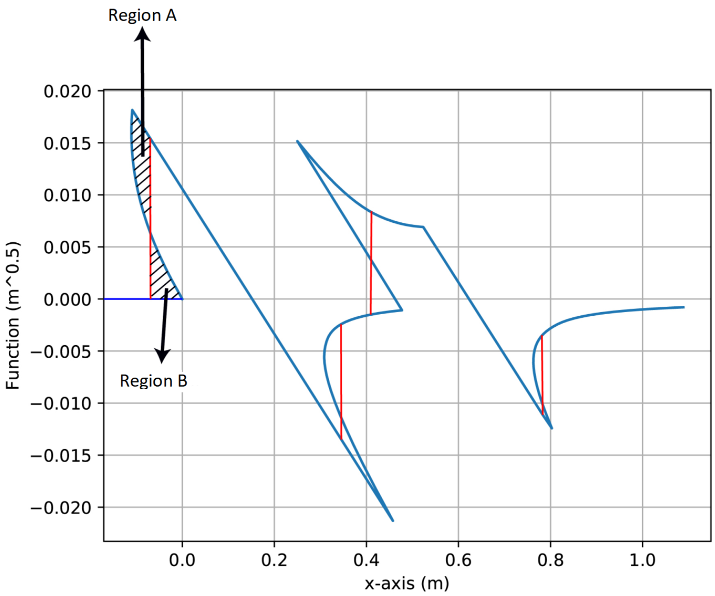

Figure 2.16 : Equal area rule illustration

In this figure, the shock location can be calculated by integration of the F-function with respect to distorted coordinates. The integration curve of the F-function in Figure 2.16 is shown in Figure 2.17.

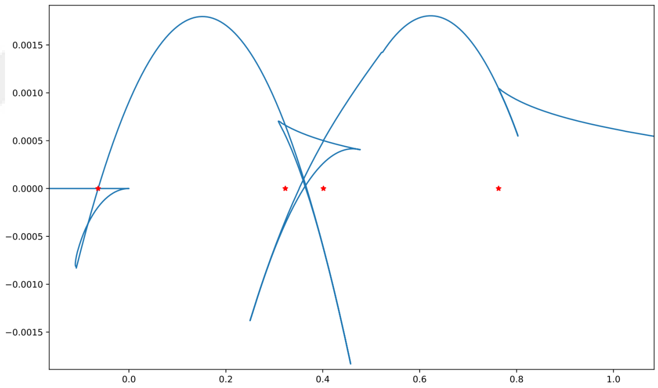

Figure 2.17 : Integration curve of the F-function

In this figure, red points represent shock locations where the integration curve intersects with itself. Replacing shocks in the F-function is explained in Section 3.

Equation (2.37) is defined for a uniform atmosphere. To extend the signal propagation for a real stratified atmosphere, geometrical acoustics can be utilized instead of Whitham's formula which is named the aging parameter.

2.2.3 Geometrical acoustics and ray tracing

The theory of geometrical acoustics is derived from geometrical optics. First, a supersonic aircraft can be considered as a point source that generates plane waves in the acoustical frame of reference. Therefore, a pressure signature computed at the near-field region can be considered as a family of wavefronts moving in the atmosphere. These waves are considered as plane waves. Each of these wavefronts has wave normals oriented in the direction of propagation. For a uniform atmosphere, the wave normals are constant during propagation and the shape of the ray paths is a straight line. Stratification in the atmosphere causes a curvature via refraction in the ray's paths. This refraction can be calculated by using Snell's law as shown in Figure 2.18.

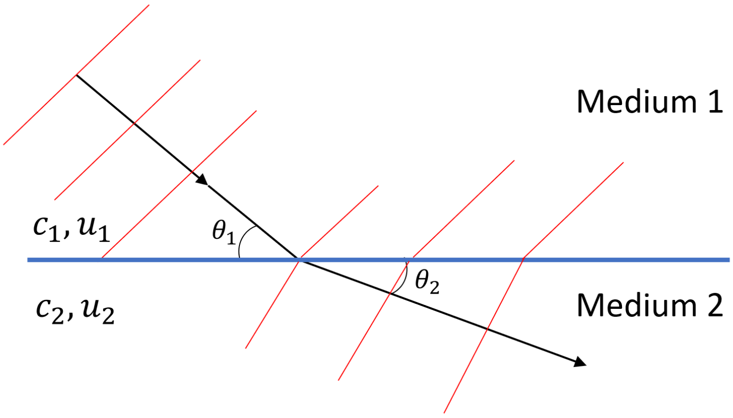

Figure 2.18 : Illustration of Snell's Law for a ray path

And the formula of Snell's Law is:

$$\frac{c_1}{\cos\theta_1} + u_1 = \frac{c_2}{\cos\theta_2} + u_2 \qquad \textbf{(2.38)}$$

where θ is the grazing angle, the angle between the horizontal plane and ray, u is the horizontal wind velocity and c is the ambient speed of sound. The calculation of ray paths starts with the initial wave normals. These initial wave normals depend on flight conditions such as Mach number, horizontal wind velocity at flight altitude, and aircraft maneuver. The following relations can be used to calculate initial wave normals:

$$\sin\gamma = \lambda \sin\phi \left[1 + \lambda^2 \sin^2\phi\right]^{-1/2} \qquad \textbf{(2.39)}$$

$$\cos\theta = -\frac{1}{M\cos\gamma} \qquad \textbf{(2.40)}$$

where ϕ is the azimuthal angle and $\lambda = \left(M^2 - 1\right)^{-1/2}$. There are four different ordinary differential equations that govern the ray tracing solution defined by Eq. 2.41.

$$\begin{aligned} \frac{d\xi}{dz} &= \frac{(lc_0 + u)}{nc_0} \\ \frac{d\eta}{dz} &= \frac{v}{nc_0} \\ \frac{dt}{dz} &= \frac{1}{nc_0} \\ \frac{ds}{dz} &= \left[\frac{d\xi^2}{dz} + \frac{d\eta^2}{dz} + 1\right]^{1/2} \end{aligned} \tag{2.41}$$

In equation (2.41), ξ is the coordinate that is aligned with the wave normal direction and η is the coordinate perpendicular to the wave normal direction. c_0 is the speed of sound in the atmosphere. $l = cos\theta$ and $n = sin\theta$ are the cosine directors in the ξ and z directions, respectively.

This calculation process is applied to the four adjacent rays to be used to calculate the ray tube area. These adjacent rays differ from each other by a small time step Δt and a small azimuthal angle $\Delta\phi$ as illustrated in Fig. 2.19.

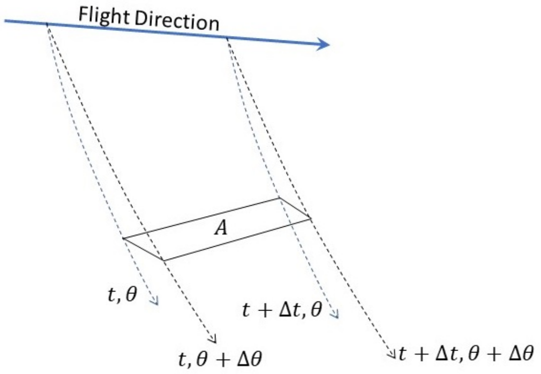

Figure 2.19 : Four adjacent rays in a ray tube

In this figure, A represents the ray tube area. First, the cross product of ray paths results in A_h which is the area of the ray tube normal to the horizontal plane. By using A_h, the actual tube area, A, perpendicular to the wavefront can be calculated as:

$$A = \frac{cA_h \sin\theta}{c_n} \tag{2.42}$$

where:

$$c_n = c + \vec{W} \cdot \vec{n} \tag{2.43}$$

$\vec{W}$ is the wind vector and $\vec{n}$ is the ray path direction. The effect of a windy atmosphere on a ray trajectory is illustrated in Fig. 2.20 and on the hyperbolic ground intersection curve in Fig. 2.21. The red curve represents the atmosphere profile without wind while the blue curve is calculated with a sample wind profile.

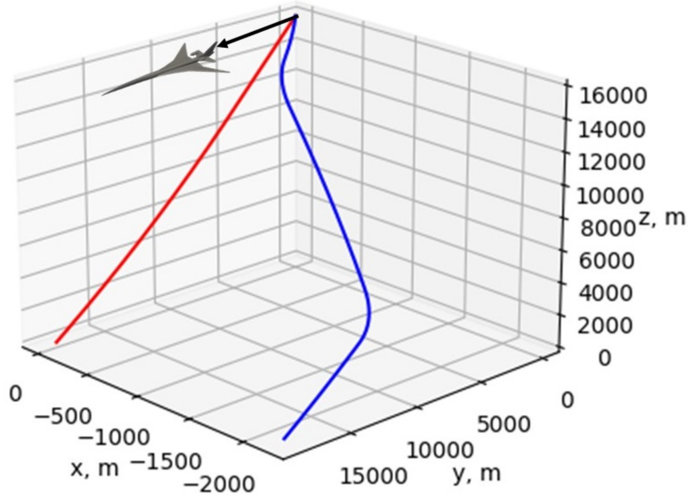

Figure 2.20 : Ray path trajectory with and without wind

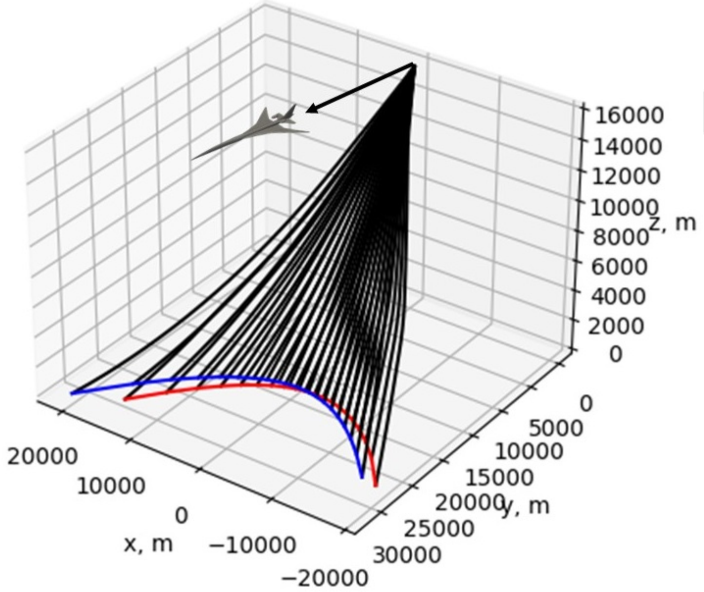

Figure 2.21 : Wind effect on the ground intersection curve of rays

The ray tube area can be calculated for the amplitude of the pressure signature at each calculation step through the ray tube. Blokhintzev invariant that is derived based on the conservation of energy [36] can be used to find the change of amplitude for pressure signature:

$$\frac{\mathrm{P}^2}{\mathrm{q}^2\rho_\mathrm{o}\mathrm{c}_\mathrm{o}}\mathrm{A} = \text{ constant} \tag{2.44}$$

In the equation (2.44), $q = \left(1+\frac{\vec{u}_0}{c_0}\cdot\vec{n}\right)^{-1}$, ρ_0 and c_0 are ambient density and speed of sound, and P is the acoustic pressure. Blokhintzev invariant is satisfied during the nonlinear wave propagation with stratification and spreading.

2.3 Nonlinear Sonic Boom Propagation

Nonlinear sonic boom propagation is the high amplitude wave propagation in a nonhomogeneous relaxing medium. Therefore, the governing equations can be derived from fluid dynamics equations such as continuity, momentum, energy equations, and equation of state. Then, it can be reduced to one-dimensional space to be calculated along the ray tube.

For the sake of completeness, the derivation of the augmented Burgers equation which is the governing equation of nonlinear sonic boom propagation is summarized in the following section from Cleveland's thesis [47].

2.3.1 Wave propagation in a non-homogeneous medium

First, we can start with the continuity equation of fluid dynamics:

$$\frac{\partial \rho}{\partial t} + \nabla\cdot(\rho \mathrm{u}) = 0 \tag{2.45}$$

For the conservation of momentum, the typical equation is not practical due to the constant viscosity assumption. In the atmosphere, viscosity changes with altitude. Therefore, the following momentum equation can be used:

$$\begin{aligned}\rho\left(\frac{\partial \mathbf{u}}{\partial t}+\mathbf{u}\cdot\nabla\mathbf{u}\right) = &-\nabla p+\rho\mathbf{B}+(\lambda+2\mu)\nabla(\nabla\cdot\mathbf{u})-\mu\nabla\times\nabla\times\mathbf{u}\\ &+(\nabla\lambda)\nabla\cdot\mathbf{u}+2(\nabla\mu)\cdot\nabla\mathbf{u}+(\nabla\mu)\times(\nabla\times\mathbf{u})\end{aligned} \tag{2.46}$$

Since the irrotational flow assumption holds for the sonic boom problem, the momentum equation reduces to:

$$\rho\left(\frac{\partial \mathbf{u}}{\partial t}+\mathbf{u}\cdot\nabla\mathbf{u}\right) = -\nabla p+\rho\mathbf{B}+(\lambda+2\mu)\nabla(\nabla\cdot\mathbf{u})+(\nabla\lambda)\nabla\cdot\mathbf{u}+2(\nabla\mu)\cdot\nabla\mathbf{u} \tag{2.47}$$

The energy equation can be written in terms of entropy for a viscous and heat-conducting fluid:

$$\rho T\frac{\mathrm{D}\chi}{\mathrm{D}t} = \nabla\cdot(\kappa\nabla T)+\tau_{ij}\partial_j u_i \tag{2.48}$$

For an irrotational flow, $\tau_{ji} = \lambda \partial_u u_k \delta_{ij} + 2\mu \partial_i u_j$. Therefore:

$$\begin{aligned} \rho T \frac{\mathrm{D}\chi}{\mathrm{D}t} &= \nabla \cdot (\kappa \nabla T) + \left(\lambda \partial_k u_k \delta_{ij} + 2\mu \partial_j u_i\right) \partial_i u_j \\ &= \nabla \cdot (\kappa \nabla T) + \lambda \left(\partial_k u_k\right)^2 + 2\mu \left(\partial_i u_j \partial_j u_i\right) \end{aligned} \tag{2.49}$$

The equation of state can be used to close the system of equations:

$$p = p(\rho, \chi). \tag{2.50}$$

In these equations, the following variables are used:

- ρ density
- p pressure
- u particle velocity
- B body force
- T temperature
- χ entropy
- λ dilatational viscosity coefficient
- μ shear viscosity coefficient
- κ thermal conductivity coefficient

The ranking system can be utilized for the acoustic waves to simplify these equations. First, we can introduce acoustics variables such as $\mathbf{u}$, ρ', p', and T'. Then, the fluid variables can be decomposed into ambient and acoustics variables such that $\rho = \rho_0 + \rho', p = p_0 + p', \mathbf{u} = \mathbf{u}, T = T_0 + T', \chi = \chi_0 + \chi'$. Substituting these variables into fluid dynamics equations and ignoring third and higher-order terms, the fluid dynamics equations for an inhomogeneous fluid that are correct to second order can be recovered.

$$\begin{aligned} \frac{\partial \rho'}{\partial t} + \rho_0 \nabla \cdot \mathbf{u} &= -\mathbf{u} \cdot \nabla \rho_0 - \nabla \cdot \left(\rho' \mathbf{u}\right) \\ \rho_0 \frac{\partial \mathbf{u}}{\partial t} + \nabla p' - \rho' \nabla p_0 &= -\rho' \frac{\partial \mathbf{u}}{\partial t} - \rho_0 \mathbf{u} \nabla \cdot \mathbf{u} + (\lambda + 2\mu) \nabla (\nabla \cdot \mathbf{u}) \\ \rho_0 T_0 \left(\frac{\partial \chi'}{\partial t'} + \mathbf{u} \cdot \chi_0\right) &= \kappa_0 \nabla^2 T' \end{aligned} \tag{2.51}$$

The equation of state must also be written using acoustic variables to be combined with other fluid dynamics equations. Taylor series expansion around ambient conditions can be written as:

$$p_0+p'=p\left(\rho_0,\chi_0\right)+\rho'\left.\frac{\partial p}{\partial \rho}\right|_{\rho_0,\chi_0}+\frac{\rho'^2}{2}\left.\frac{\partial^2 p}{\partial \rho^2}\right|_{\rho_0,\chi_0}+\chi'\left.\frac{\partial p}{\partial \chi}\right|_{\rho_0,\chi_0}+\cdots \tag{2.52}$$

As the ambient pressure is $p_0=p\left(\rho_0,\chi_0\right)$, equation (2.52) reduces to

$$p'=\rho'\left.\frac{\partial p}{\partial \rho}\right|_{\rho_0,\chi_0}+\frac{\rho'^2}{2}\left.\frac{\partial^2 p}{\partial \rho^2}\right|_{\rho_0,\chi_0}+\chi'\left.\frac{\partial p}{\partial \chi}\right|_{\rho_0,\chi_0}+O\left(\varepsilon^3,\delta\varepsilon^2\right). \tag{2.53}$$

The first two terms can be calculated with respect to density:

$$\left.\frac{\partial p}{\partial \rho}\right|_{\rho_0,\chi_0}\triangleq c_0^2 \tag{2.54}$$

$$\left.\frac{\partial^2 p}{\partial \rho^2}\right|_{\rho_0,\chi_0}\triangleq \frac{c_0^2}{\rho_0}\frac{B}{A} \tag{2.55}$$

Since $\chi'=0$ for isentropic flow, the equation of state can be written as follows.

$$p'=c_0^2\rho'+\frac{c_0^2}{\rho_0}\frac{B}{2A}\rho'^2 \tag{2.56}$$

If the entropy is not constant, the term $\chi'\left.\frac{\partial p}{\partial \chi}\right|_{\rho_0,\chi_0}$ must be calculated. According to the Kirchhoff-Fourier equation for a thermally conducting fluid:

$$\frac{\partial \chi'}{\partial t}+\mathrm{u}\cdot\nabla\chi_0=\frac{\kappa}{\rho_0 T_0}\nabla^2 T' \tag{2.57}$$

Here, we need to obtain a relation for χ in terms of density. If the temperature is as a function of density and entropy, the first-order Taylor series expansion can be calculated as follows.

$$T'=\rho'\left.\frac{\partial T}{\partial \rho}\right|_{\rho_0,\chi_0}+O\left(\varepsilon\delta,\varepsilon^2\right) \tag{2.58}$$

and

$$\nabla^2 T'=\left.\frac{\partial T}{\partial \rho}\right|_{\rho_0,\chi_0}\nabla^2\rho' \tag{2.59}$$

With the assumption of an ideal gas:

$$\left.\frac{\partial T}{\partial \rho}\right|_{\rho_0,\chi_0}=(\gamma-1)\frac{T_0}{\rho_0} \tag{2.60}$$

The equation can be written as following form by using $\nabla^2\rho'=\frac{1}{c_0^2}\frac{\partial^2\rho'}{\partial t^2}+O\left(\varepsilon^2\right)$ for denisty.

$$\frac{\partial \chi'}{\partial t}+\mathbf{u}\cdot\nabla\chi_0=\frac{\kappa}{c_0^2\rho_0^2}(\gamma-1)\frac{\partial^2\rho'}{\partial t^2}+O\left(\delta\varepsilon^2\right) \tag{2.61}$$

Since we are considering a non-homogeneous fluid, $\nabla\chi_0 \neq 0$. Then, we can take the partial derivative of the equation (2.53) and substitute it into equation (2.61):

$$\frac{\partial p'}{\partial t} = c_0^2\frac{\partial \rho'}{\partial t} + \frac{\kappa}{C_p}(\gamma-1)\frac{\partial^2 \rho'}{\partial t^2} - \left.\frac{\partial p}{\partial \chi}\right|_0 \mathbf{u}\cdot\nabla\chi_0 + \frac{c_0^2}{\rho_0}\frac{B}{2A}\frac{\partial \rho'^2}{\partial t} \tag{2.62}$$

From the equation of state:

$$\nabla p_0 = \left.\frac{\partial p}{\partial \rho}\right|_0 \nabla\rho_0 + \left.\frac{\partial p}{\partial \chi}\right|_0 \nabla\chi_0 \tag{2.63}$$

Finally, the gradient of entropy can be expressed in terms of the density and pressure gradient as:

$$\left.\frac{\partial p}{\partial \chi}\right|_0 \nabla\chi_0 = \nabla p_0 - \left.\frac{\partial p}{\partial \rho}\right|_0 \nabla\rho_0 \tag{2.64}$$

Substituting into equation (2.62) yields the equation of state for a non-homogeneous fluid as follows.

$$\frac{\partial p'}{\partial t} = c_0^2\frac{\partial \rho'}{\partial t} + \frac{\kappa}{C_p}(\gamma-1)\frac{\partial^2 \rho'}{\partial t^2} + \frac{c_0^2}{\rho_0}\frac{B}{2A}\frac{\partial \rho'^2}{\partial t} - \mathbf{u}\cdot\left(\nabla p_0 - c_0^2\nabla\rho_0\right) \tag{2.65}$$

where B is the body force.

2.3.2 Relaxing fluid

There are 3 energy modes of molecules in a fluid such as transitional, rotational, and vibrational energy. During the passage of an acoustic wave, the external energy of the wave can be transformed into the internal energy of molecules. This changes the equilibrium state of molecules, especially N_2 and O_2 for the air. Returning to the equilibrium state is called the relaxation process and the time between wave passage and the equilibrium state is called relation time. The relaxation process, therefore relaxation time, is responsible for the shock rise time in the pressure waveform.

The relaxation process can be added to the equation of state to the model during wave propagation. Only vibrational relaxation is considered as it dominates the effect of others. For O_2 and N_2, relaxation processes can be calculated independently and added as a superposition solution. A new thermodynamic variable representing each relaxation process is introduced as ξ. Now, the equation of state depends on these variables $p = p(\rho, \chi, \xi_O, \xi_N, \cdots)$. Here, we can write ξ in terms of equilibrium and deviation terms $\xi_v = \xi_{v,q} + \xi_v'$.

For the new variables, the Taylor series expansion of the equation of state is:

$$p' = \rho'\left.\frac{\partial p}{\partial \rho}\right|_q + \frac{\rho'^2}{2}\left.\frac{\partial^2 p}{\partial \rho^2}\right|_q + \chi'\left.\frac{\partial p}{\partial \chi}\right|_q + \sum_v \xi_v'\left.\frac{\partial p}{\partial \xi_v}\right|_q + \cdots \tag{2.66}$$

The partial derivative of ξ with respect to time is

$$\frac{\partial \xi_v}{\partial t} = \frac{\partial \xi_v'}{\partial t} + \frac{\partial \xi_{v,q}}{\partial t} \tag{2.67}$$

Here $_q$ represents the equilibrium state where $_o$ is the ambient subscript. It should be noticed that the equilibrium conditions are time-dependent. Therefore, they can vary in waveform. The following law also can be used to define time derivative [37]:

$$\frac{\partial \xi_v}{\partial t} = -\frac{\xi_v - \xi_{v,q}}{\tau_v} \tag{2.68}$$

where τ_v is the relaxation time and ξ as a function of density can be written by Taylor series expansion as follows.

$$\xi_{v,q} = \xi_{v,0} + \rho' \left.\frac{\partial \xi_{v,q}}{\partial \rho'}\right|_0 + O\left(\varepsilon^2, \delta\varepsilon\right) \tag{2.69}$$

Here, relaxation processes are independent of the second order. The equation (2.67) and (2.69) can be substituted into equation (2.68):

$$\xi_v' = -\left.\frac{\partial \xi_{v,q}}{\partial \rho}\right|_0 \frac{\tau_v}{1 + \tau_v \frac{\partial}{\partial t}} \frac{\partial \rho'}{\partial t} \tag{2.70}$$

The operator may be expressed as the following integral:

$$\frac{\tau_v}{1 + \tau_v \frac{\partial}{\partial t}} f(t) = \int_{-\infty}^{t} e^{(t'-t)/\tau_v} f\left(t'\right) dt' \tag{2.71}$$

Here, the equation of state can be written such that the acoustic pressure in terms of the acoustic density:

$$p' = c_0^2 \rho' + \frac{c_0^2}{\rho_0} \frac{B}{2A} \rho'^2 + \frac{\kappa}{C_p}(\gamma - 1) \frac{\partial \rho'}{\partial t} - \sum_v \left.\frac{\partial p}{\partial \xi_v}\right|_0 \left.\frac{\partial \xi_{v,q}}{\partial \rho}\right|_0 \frac{\tau_v \frac{\partial}{\partial t}}{1 + \tau_v \frac{\partial}{\partial t}} \rho' \tag{2.72}$$

A new parameter can be introduced as the dispersion parameter:

$$m_v = -\frac{1}{c_0^2} \left.\frac{\partial p}{\partial \xi_v}\right|_0 \left.\frac{\partial \xi_{v,q}}{\partial \rho}\right|_0 \tag{2.73}$$

Finally, the equation of state for a non-homogenous relaxing fluid can be obtained:

$$\frac{\partial p'}{\partial t} = c_0^2 \frac{\partial \rho'}{\partial t} + \mathscr{K} \frac{\partial^2 \rho'}{\partial t^2} + \frac{c_0^2}{\rho_0} \frac{B}{2A} \frac{\partial \rho'^2}{\partial t} - \mathbf{u} \cdot \left(\nabla p_0 - c_0^2 \nabla \rho_0\right) \tag{2.74}$$

where;

$$\mathscr{K} = \frac{\kappa}{\rho_0 C_p}(\gamma - 1) + c_0^2 \sum_v \frac{m_v \tau_v}{1 + \tau_v \frac{\partial}{\partial t}} \tag{2.75}$$

For an ideal gas, $B/A = \gamma - 1$.

2.3.3 Augmented Burgers equation

In the previous section, the equation of state in addition to continuity and momentum equations is provided. In this section, these equations will be reduced into one dimension for the sonic boom problem. The continuity, momentum, and state equations with multiple relaxations in one dimension can be written as follows.

$$\frac{\partial \rho'}{\partial t} + \rho_0 \frac{\partial u}{\partial z} = -\frac{\partial \left(\rho' u\right)}{\partial z} \tag{2.76}$$

$$\rho_0 \frac{\partial u}{\partial t} + \frac{\partial p'}{\partial z} = (\lambda + 2\mu)\frac{\partial^2 u}{\partial z^2} - \frac{\rho_0}{2}\frac{\partial u^2}{\partial z} - \rho' \frac{\partial u}{\partial t} \tag{2.77}$$

$$p' = c_0^2 \rho' + \mathscr{K} \frac{\partial \rho'}{\partial t} + \frac{c_0^2}{\rho_0}\frac{B}{2A}\rho'^2 \tag{2.78}$$

Here, we need to perform a transformation of the independent variables to a slow range variable ($x = \varepsilon z$) and retarded time frame $\tau = t - z/c_0$. If we apply the continuity equation:

$$\frac{\partial \rho'}{\partial \tau} + \rho_0 \left(\varepsilon \frac{\partial u}{\partial x} - \frac{1}{c_0}\frac{\partial u}{\partial \tau} \right) = -\varepsilon \frac{\partial \rho' u}{\partial x} + \frac{1}{c_0}\frac{\partial \rho' u}{\partial \tau} \tag{2.79}$$

We can eliminate higher-order terms:

$$\frac{\partial \rho'}{\partial \tau} - \frac{\rho_0}{c_0}\frac{\partial u}{\partial \tau} = -\rho_0 \varepsilon \frac{\partial u}{\partial x} + \frac{1}{c_0}\frac{\partial \rho' u}{\partial \tau} \tag{2.80}$$

Then, the momentum equation becomes:

$$\rho_0 \frac{\partial u}{\partial \tau} - \frac{1}{c_0}\frac{\partial p'}{\partial \tau} = -\varepsilon \frac{\partial p'}{\partial x} - \frac{(\lambda + 2\mu)}{c_0^2}\frac{\partial^2 u}{\partial \tau^2} - \frac{\rho_0}{2c_0}\frac{\partial u^2}{\partial \tau} - \rho' \frac{\partial u}{\partial \tau} \tag{2.81}$$

From previous section, we have the first-order relations as $\rho' = \rho_0 u / c_0, p' = \rho_0 c_0 u$, and $p' = c_0^2 \rho'$. By using the first-order relations, the second-order can be manipulated to obtain continuity and momentum equations as follows.

$$\frac{\partial \rho'}{\partial \tau} - \frac{\rho_0}{c_0}\frac{\partial u}{\partial \tau} = -\frac{\varepsilon}{c_0}\frac{\partial p'}{\partial x} + \frac{1}{\rho_0 c_0^4}\frac{\partial p'^2}{\partial \tau} \tag{2.82}$$

$$\begin{aligned} \rho_0 \frac{\partial u}{\partial \tau} - \frac{1}{c_0}\frac{\partial p'}{\partial \tau} &= -\varepsilon \frac{\partial p'}{\partial x} + \frac{(\lambda + 2\mu)}{\rho_0 c_0^3}\frac{\partial^2 p'}{\partial \tau^2} + \frac{1}{2\rho_0 c_0^3}\frac{\partial p'^2}{\partial \tau} - \frac{1}{2\rho_0 c_0^3}\frac{\partial p'^2}{\partial \tau} \\ &= -\varepsilon \frac{\partial p'}{\partial x} + \frac{(\lambda + 2\mu)}{\rho_0 c_0^3}\frac{\partial^2 p'}{\partial \tau^2}. \end{aligned} \tag{2.83}$$

And the equation of state is:

$$p' = c_0^2\rho' + \frac{\mathscr{K}}{c_0^2}\frac{\partial p'}{\partial \tau} + \frac{1}{\rho_0 c_0^2}\frac{B}{2A}p'^2 \tag{2.84}$$

We can use the equation of state to remove density from the continuity equation:

$$\begin{gathered}
\frac{1}{c_0^2}\frac{\partial p'}{\partial \tau} - \frac{\mathscr{K}}{c_0^4}\frac{\partial^2 p'}{\partial \tau^2} - \frac{1}{\rho_0 c_0^4}\frac{B}{2A}\frac{\partial p'^2}{\partial \tau} - \frac{\rho_0}{c_0}\frac{\partial u}{\partial \tau} = -\frac{1}{c_0}\varepsilon\frac{\partial p'}{\partial x} + \frac{1}{\rho_0 c_0^4}\frac{\partial p^2}{\partial \tau} \\
\frac{1}{c_0}\frac{\partial p'}{\partial \tau} - \rho_0\frac{\partial u}{\partial \tau} = -\varepsilon\frac{\partial p'}{\partial x} + \frac{\mathscr{K}}{c_0^4}\frac{\partial^2 p'}{\partial \tau^2} + \frac{\beta}{\rho_0 c_0^3}\frac{\partial p'^2}{\partial \tau}
\end{gathered} \tag{2.85}$$

This equation can be substituted into the momentum equation to eliminate $\frac{\partial u}{\partial \tau}$ term.

$$0 = -2\varepsilon\frac{\partial p'}{\partial x} + \frac{(\lambda + 2\mu + \rho_0\mathscr{K})}{\rho_0 c_0^3}\frac{\partial^2 p'}{\partial \tau^2} + \frac{\beta}{\rho_0 c_0^3}\frac{\partial p'^2}{\partial \tau} \tag{2.86}$$

This is a progressive wave equation in terms of p'. Now, we can transform back to the physical range variable:

$$\frac{\partial p'}{\partial z} - \frac{\beta}{2\rho_0 c_0^3}\frac{\partial p'^2}{\partial t'} = \frac{b}{2\rho_0 c_0^3}\frac{\partial^2 p'}{\partial t^2} + \frac{1}{2c_0}\sum_\nu \frac{m_\nu \tau_\nu \frac{\partial^2}{\partial t'^2}}{1 + \tau_\nu \frac{\partial}{\partial t'}}p' \tag{2.87}$$

Equation (2.87) is the augmented Burgers equation in the dimensional form. In ITUBOOM dimensionless form is solved numerically. Therefore, the following dimensionless form with the addition of the spreading term can be obtained:

$$\frac{\partial P}{\partial \sigma} = P\frac{\partial P}{\partial \tau} + \frac{1}{\Gamma}\frac{\partial^2 P}{\partial \tau^2} + \sum_\nu C_\nu \frac{\frac{\partial^2}{\partial \tau^2}}{1 + \theta_\nu \frac{\partial}{\partial \tau}}P - \frac{\frac{\partial}{\partial \sigma}S}{2S}P + \frac{\frac{\partial}{\partial \sigma}(\rho_0 c_0)}{2\rho_0 c_0}P \tag{2.88}$$

In this equation P is the dimensionless pressure, σ is the dimensionless distance, Γ is the dimensionless thermoviscous parameter called Gol'berg number, C_ν is the dimensionless dispersion parameter, θ_ν is the dimensionless relaxation time, and τ is the dimensionless time. The following relations are used to obtain these dimensionless parameters;

- $\sigma = z/\bar{x}$ where $\bar{x}$ is the shock formation distance
- $P = p'/P_0$ where P_0 is the reference peak pressure
- $\Gamma = 1/\alpha_0^{\mathrm{tv}}\bar{x}$ where $\alpha_0^{\mathrm{tv}} = \delta\omega_0^2/2c_0^3$ with δ being the diffusion parameter
- $C_\nu = \frac{m_\nu \tau_\nu \omega_0^2}{2c_0}\bar{x}$

- $\theta_\nu = \omega_0 \tau_\nu$ where ω_0 is the angular frequency
- $\tau = \omega_0 t'$ where t' is the retarded time to be defined as $t' = t - \int \frac{\mathrm{d}z}{c_0}$
- S is the ray tube area

In the next section, the numerical solution of equation (2.88) is explained.

3. ITUBOOM - SONIC BOOM PROPAGATION CODE

ITUBOOM is a sonic boom propagation suite that is developed in ITU AeroMDO Lab using Python language and is implemented in aircraft design and optimization studies. In the following section, the structure of the program, numerical calculation of the linear prediction method, ray tracing, and nonlinear prediction method are explained, respectively.

3.1 Program Structure

The program consists of two main modules. In the first module, ITUBOOM can be used to generate a near-field pressure signature from a CFD output in VTK format. The user must define flight conditions, the axial distance between the signal location and aircraft axis, and the azimuth angle. Two options are added to generate a near-field pressure signature from a CFD output. For the first option, the user must provide an output that contains the whole solution domain. Then, the program extracts the in-flow pressure signature from the CFD output directly. The second option is related to the calculation of the equivalent area distribution from the aircraft surface. According to the Mach number, angle of attack, and azimuth angle, ITUBOOM generates slices to calculate intersection surfaces between slice planes and the aircraft surface. Then, the equivalent area distribution is calculated along the x direction. By using area distribution, a near-field pressure signature can be calculated with equation 2.20. If the second option is used to generate a pressure signature, an output file that contains only aircraft surface mesh is required. This method is more convenient for low-fidelity panel method solutions.

The second module in ITUBOOM is wave propagation. The simplest option is the calculation of ISPR from a near-pressure signature. However, the default option is the solution of the augmented Burgers equation with ray tracing. If a custom atmosphere profile is not provided by the user, ITUBOOM uses a standard atmosphere profile for the temperature and relative humidity. Due to the numerical method, zero padding points are added to the front and rear sections of the signature. Two flags can be defined by the user to disable thermoviscosity and relaxation. In this case, ITUBOOM switches to a fixed step size and uses the equal-area rule for the waveform. After performing a numerical solution, pressure signature on the ground level, ground intersection points and propagation time can be obtained. For the perceived loudness calculation on the ground, USU Aero Lab's PyLdB [106] code is implemented in ITUBOOM. The flowchart of ITUBOOM is illustrated in Fig. 3.1.

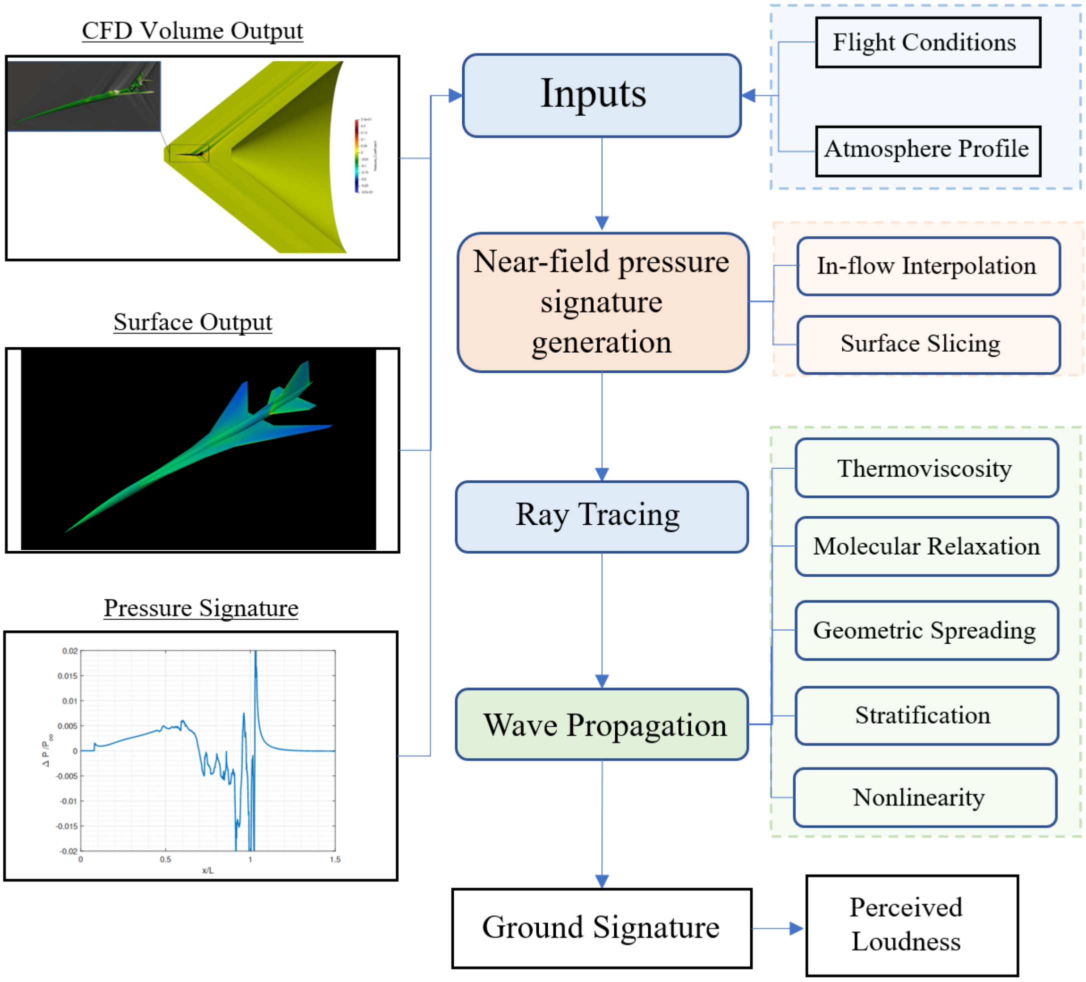

Figure 3.1 : Flowchart of ITUBOOM program

3.2 Near-Field Pressure Signature Calculation

As mentioned before, the near-field pressure signature can be calculated in two different ways. The first method is more accurate since it includes the effect of complex shock structures in the flow domain. The user must define a signal location in terms of axial distance and azimuth angle. By using these parameters, ITUBOOM defines a line that lies on the Mach cone domain. Therefore, the Mach angle is used to calculate the x location of the line. Users also can enter the angle of attack to align the signature line with the free-stream flow. However, if the aircraft geometry is rotated for the angle of attack instead of changing free-stream direction, the angle of attack parameter must be entered as zero. For the signature sampling, the default value is 2000 points. Users can increase the number of points depending on the number of mesh elements in the free-stream direction, however, 2000 points are found to be sufficient for the sonic boom propagation. Figure 3.2 shows an illustration of the near-field signature.

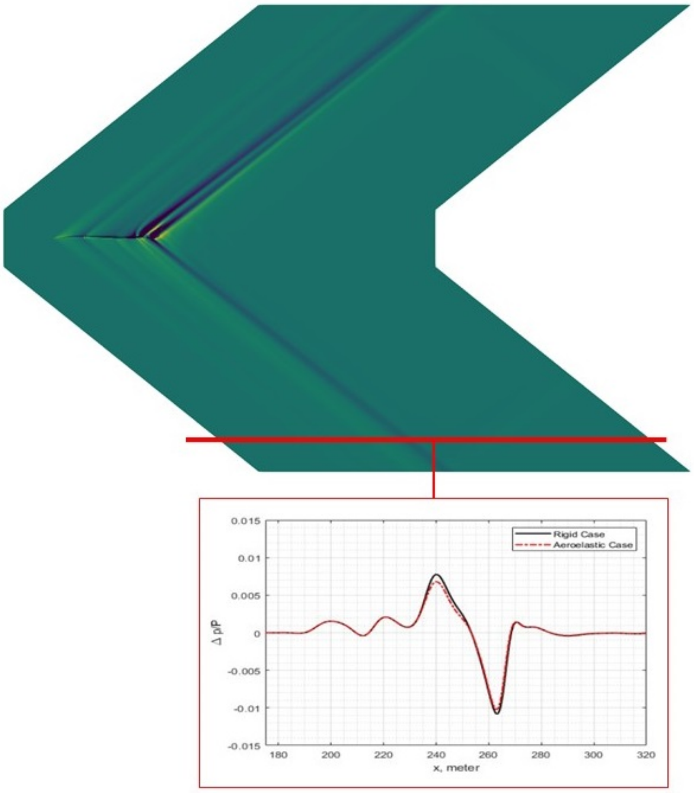

Figure 3.2 : Near-pressure signature line definition

If the CFD output file doesn't include pressure scalars in the flow field, the pressure coefficient can also be used to calculate the pressure signature as follows.

$$C_p = \frac{p - p_\infty}{\frac{\gamma}{2} p_\infty M^2} \tag{3.1}$$

3.2.1 Equivalent area distribution

The second method in ITUBOOM is equivalent area distribution calculation for the near-field pressure signature. This method is more suitable where only surface pressure distribution is available. Therefore, it can be used for the panel method solutions. To calculate equivalent area distribution, we need to take slices along the aircraft axis as explained in Section 2. VTK Python library is employed for the slicing. In the following subsection, the slicing technique in ITUBOOM is explained in detail.

3.2.1.1 Slicing

First, plane arrays beginning from the aircraft nose to the tail must be defined. These planes must be aligned with the Mach angle and angle of attack. A convergence study was performed to determine a minimum number of slices along the aircraft axis. Even though it depends on the complexity of the geometry, 300 slices were found as a sufficient. As the number of slices increases, the computation time also increases exponentially. After defining slice planes, an intersection command is called to find the intersection curves of each slice with the aircraft surface. Figure 3.3 shows the slicing of an aircraft surface.

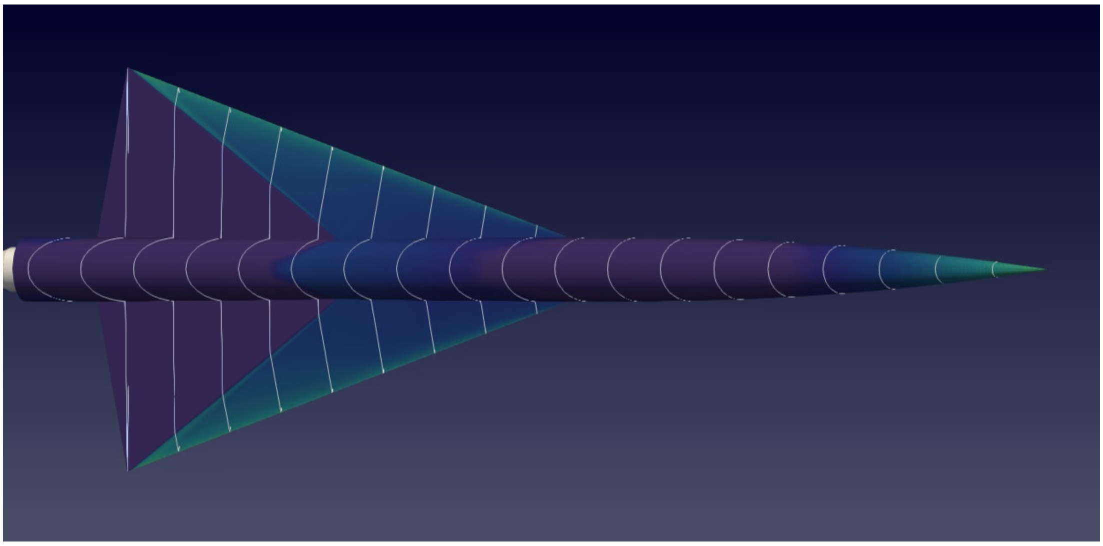

Figure 3.3 : Surface slicing of a delta wing model

When the intersection curves between slice planes and the aircraft surface are closed curves, the program can perform the integration. However, these intersection curves may not be closed surfaces in the presence of engine nacelle or in the case of complex geometries. Therefore, special treatment must be done in these situations. If ITUBOOM detects non-closed curves, another command from the VTK library is called to separate intersection curves into several closed curves. Then, the program performs integration over these each closed curve to be summed for the total lift and volume value of the current slice. Figure 3.4 illustrates an intersection curve between a supersonic airliner and a specific slice. As seen in the figure, there are two different closed curves which are needed to be integrated separately.

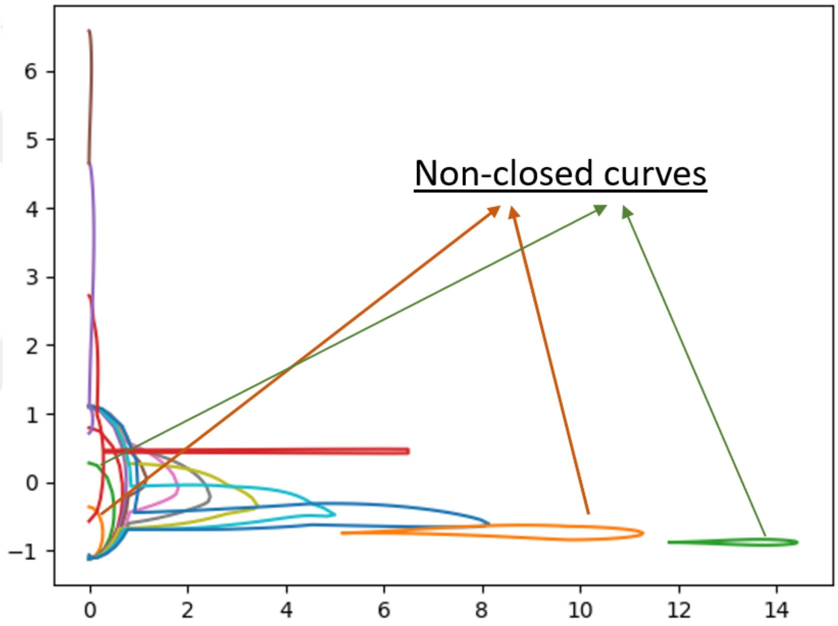

Figure 3.4 : Non-closed intersection curves

The trapezoidal rule is implemented for the calculation of line integral over intersection curves. For the volume calculation, equation (3.2) is used to calculate the intersection area.

$$A_{slice} = \sum_{i=1}^{N} (y_{i+1} + y_i) \times (z_{i+1} - z_i) \tag{3.2}$$

where y and z are the coordinates of points on the intersection curve and N is the total number of points on the slice. After, the lift component can be calculated as:

$$L_{slice} = \frac{1}{2} \sum_{i=1}^{N-1} (P_{i+1} + P_i) \times ds \times \vec{n}_z \tag{3.3}$$

where ds is the distance between two adjacent points and $\vec{n}_z$ is the z component of the normal vector. Therefore, surface normals must be calculated before the slicing operation for the lift component. After lift integration for each slice, the total equivalent area distribution can be obtained along the aircraft axis. The user must be defined if the surface file is a half-geometry or not. The program multiplies lift and volume values by 2 to take into account half geometries.

An equivalent area distribution is given in Fig. 3.5 calculated from a supersonic airliner. The flow solution was performed with PAN AIR as illustrated in Fig. 3.6.

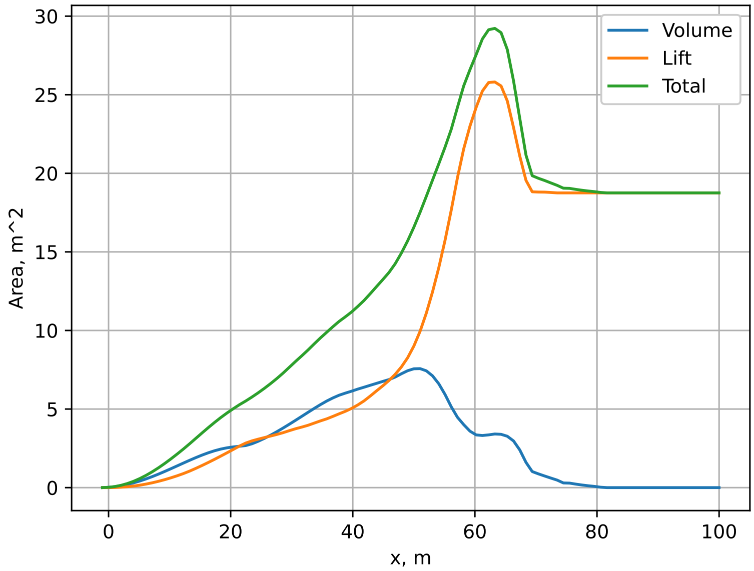

Figure 3.5 : Equivalent area distribution of supersonic airliner

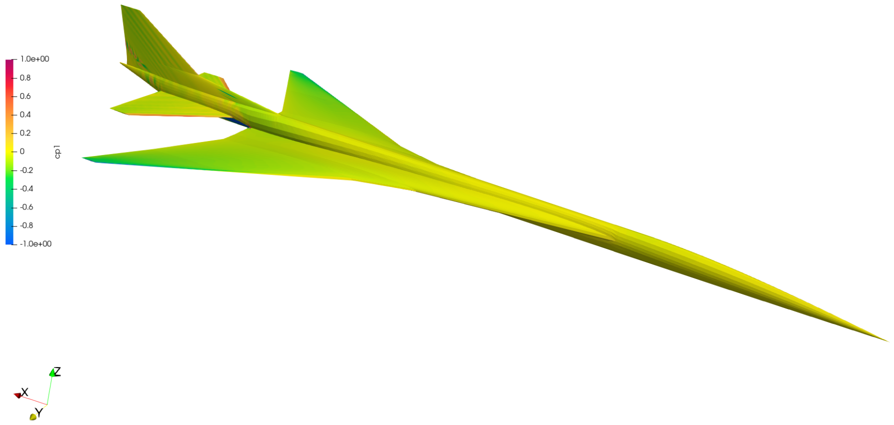

Figure 3.6 : Surface pressure distribution from PAN AIR

3.2.1.2 Lighthill F-function calculation

After calculating the equivalent area distribution, it must be converted to a near-field pressure signature. To do this, we need to first obtain F-function. As mentioned in Section 2, Lighthill F-function is used instead of the original Whitham F-function. First, a Stieltjes integral calculation is performed in the following form as [8] proposed for the discontinuous area distribution.

$$\int P(x)\mathrm{d}G(x) = \int P(x)G'(x)\mathrm{d}x \tag{3.4}$$

The numerical discretization for the first-order derivative of area distribution is;

$$\mathrm{d}S'_n = \frac{S_{n-1} - 2S_n + S_{n+1}}{\Delta x} \tag{3.5}$$

Instead of solving the $h(\chi)$ function in the Lighthill F-function, the following approximation in Fig. 3.7 is implemented from [8].

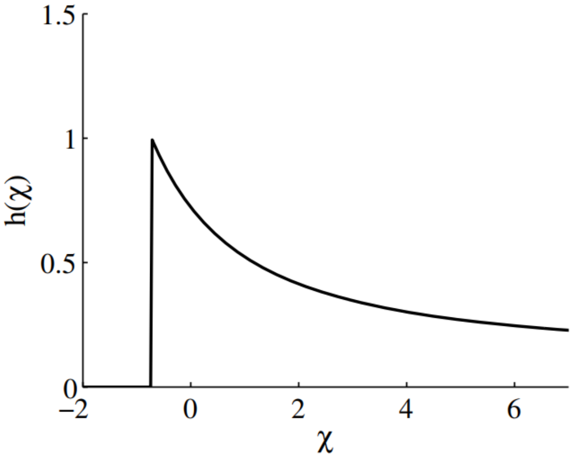

Figure 3.7 : The $h(\chi)$ function graph from [8]

Finally, a near-field pressure signature can be obtained by equation (2.14). If the linear method is used without a loss mechanism for propagation, then the area rule must be implemented for multi-valued pressure signatures. Numerical integration of distorted waveform is performed to obtain an integration curve. Locations where this integration curve intersects with itself reveal shock location. To reduce computation time, an algorithm that monitors possible shock regions is implemented. Therefore, instead of checking the intersection for the whole waveform, just multi-valued regions are checked. This algorithm reduced computation time significantly.

3.3 Ray Tube Area Calculation

Ray tube area calculation is required for the solution of the augmented Burgers equation. Also, atmospheric stratification and aircraft maneuver can be taken into account with the ray tube area calculation. Hayes [24] provided an analytical solution for the ray area by using the Jacobian calculation of the ray paths. However, four different ray path calculations are performed to calculate the ray tube area in this study. The computation time of ray tracing can be ignored as it lasts less than a second. Four adjacent rays are created at two-time steps with two azimuth angles. The difference between azimuth angles and time steps must be infinitesimally small. Therefore, 10^{-7} step size is used for both.

3.3.1 Ray tracing solution

Ray paths calculations are done with the 4 coupled ordinary differential equations given in Section 2. The number of calculation points in the ray path coordinate system is chosen as 5000. This parameter can be modified by the user in ITUBOOM. Before ray tracing calculations, the user must define an atmosphere profile for temperature and relative humidity. Otherwise, the program applies a standard atmosphere profile for the ray path calculation. The provided atmosphere profile must cover flight altitude and ground elevation. If the flight altitude is higher than the maximum altitude for the provided profiles, then the program terminates. In addition, a horizontal wind profile can also be defined. Since the linear geometric acoustics method is used, the ray path should not reach a horizontal position. If this occurs due to the low Mach number or atmosphere profile, the program terminates to prevent singularity. Finally, flight orientation such as pitch angle and aircraft maneuver can be defined by the user. The program takes into account these parameters when calculating initial wave normals for each of four adjacent rays.

3.4 Numerical Solution of Wave Equation

The numerical solution of the augmented Burgers equation is performed after calculating the ray tube area. First, the program adds zero-padding points before and after the pressure signature to ensure that both endpoints are zero due to the assumption of a numerical solution. For the waveform sampling, 10000-20000 points can be used.

Then, it calculates shock formation distance and angular frequency for the calculation of dimensionless parameters. Due to the use of the finite difference algorithm, uniform sampling is required for the waveform. Therefore, after each distortion, a linear interpolation is performed to make the waveform uniformly sampled. The operator-splitting method is implemented for the numerical solution.

3.4.1 Operator-Splitting method

In the operator-splitting, each term in the equation is solved individually. Then, these solutions can be summed to obtain a solution for the next step. The step size must be small enough to reduce the error of the method. A dimensionless step size parameter can be introduced as $\Delta\sigma$. As Cleveland [47] proposed, $\Delta\sigma$ must be smaller than 0.05. In the following subsections, numerical solutions for each individual term of equation (3.6) are provided

$$\frac{\partial P}{\partial \sigma} = P\frac{\partial P}{\partial \tau} + \frac{1}{\Gamma}\frac{\partial^2 P}{\partial \tau^2} + \sum_{\nu} C_{\nu}\frac{\frac{\partial^2}{\partial \tau^2}}{1+\theta_{\nu}\frac{\partial}{\partial \tau}}P - \frac{\frac{\partial}{\partial \sigma}S}{2S}P + \frac{\frac{\partial}{\partial \sigma}(\rho_0 c_0)}{2\rho_0 c_0}P \qquad \textbf{(3.6)}$$

3.4.1.1 Nonlinearity

The first term in equation (3.6) is responsible for the wave distortion. An analytical solution, Poisson solution, exists for the solution of this term:

$$P(\sigma+\Delta\sigma,\tau) = P(\sigma,\tau+P\Delta\sigma) \qquad \textbf{(3.7)}$$

A new coordinate can be introduced as a distorted time coordinate:

$$\tau_i^d = \tau_i - P_i^k\Delta\sigma \qquad \textbf{(3.8)}$$

In the waveform, higher-pressure regions are distorted more than lower regions.

3.4.1.2 Thermoviscous attenuation

The second term is thermoviscous attenuation where Γ is the dimensionless thermoviscous attenuation parameter. This equation can be discretized as follows:

$$P_j^{k+1} = 2\lambda P_{j-1}^k + (1-\lambda)P_j^k + 2\lambda P_{j+1}^k \qquad \textbf{(3.9)}$$

where $\lambda = \Delta\sigma/\left(2\Gamma(\Delta\tau)^2\right)$. This explicit relation can be converted into the following form that is known as the Crank-Nicolson solution which utilizes both of implicit and explicit finite difference:

$$-\lambda P_{j-1}^{k+1} + (1+2\lambda)P_{j}^{k+1} - \lambda P_{j+1}^{k+1} = \lambda P_{j-1}^{k} + (1-2\lambda)P_{j}^{k} + \lambda P_{j+1}^{k} \tag{3.10}$$

Here, there are N numbers of variables and N numbers of equations. Therefore, a linear system of equations can be written in the following matrix form.

$$\mathbf{A}_{tv}\mathbf{P}^{k+1} = \mathbf{B}_{tv}\mathbf{P}^{k} \tag{3.11}$$

where $\mathbf{A}_{tv}$ and $\mathbf{B}_{tv}$ matrices are:

$$\mathbf{A}_{tv} = \begin{pmatrix} 1 & 0 & & & \\ -\lambda & (1+2\lambda) & -\lambda & & \\ & \ddots & \ddots & \ddots & \\ & & -\lambda & (1+2\lambda) & -\lambda \\ & & & 0 & 1 \end{pmatrix} \tag{3.12}$$

$$\mathrm{B}_{tv} = \begin{pmatrix} 1 & 0 & & & \\ \lambda & (1-2\lambda) & \lambda & & \\ & \ddots & \ddots & \ddots & \\ & & \lambda & (1-2\lambda) & \lambda \\ & & & 0 & 1 \end{pmatrix} \tag{3.13}$$

These matrices are constructed such that the pressure values of both endpoints are zero. Since these are triangular matrices, a sparse structure is used in Python to solve the linear system of equations. Previously, Γ is defined as:

$$\Gamma = \frac{1}{\alpha_c \bar{x}} \tag{3.14}$$

Here, α_c^{tv} is the thermoviscous attenuation coefficient given by:

$$\alpha_c = \frac{\omega_0^2 \mu}{2\rho_0 c_0^3}\left[\frac{4}{3} + \frac{\mu_B}{\mu} + \frac{\gamma - 1}{\mathrm{Pr}}\right]. \tag{3.15}$$

where μ is the shear viscosity coefficient, μ_B is the bulk viscosity, and Pr is the Prandtl number defined as $c_p\mu/\kappa$. The following relation is used with given reference values from [37, 107].

$$\mu/\mu_0 = (T/T_0)^{3/2}\,(T_0 + T_s)\,/\,(T + T_s) \tag{3.16}$$

$$\kappa/\kappa_0 = (T/T_0)^{3/2}\left(T_0 + T_A e^{-T_B/T_0}\right)/\left(T + T_A e^{-T_B/T}\right) \tag{3.17}$$

3.4.1.3 Vibrational relaxation

The third term is equation (3.6) is responsible for vibrational relaxation during the passage of pressure wave. This term can be rearranged as:

$$\left(1+\theta_v\frac{\partial}{\partial\tau}\right)\frac{\partial P}{\partial\sigma}=C_v\frac{\partial^2 P}{\partial\tau^2} \tag{3.18}$$

Similar to thermoviscous attenuation, the Crank-Nicolson algorithm can be used to solve this term numerically. The right-hand side can be approximated as:

$$\frac{\partial^2 P}{\partial\tau\partial\sigma}=\frac{P_{i+1}^{k+1}-P_{i-1}^{k+1}-\left(P_{i+1}^{k}-P_{i-1}^{k}\right)}{2\Delta\tau\Delta\sigma}+O\left[(\Delta\sigma)^2,(\Delta\tau)^2\right] \tag{3.19}$$

For a single relaxation process, the discretization of the equation can be written in the following form.

$$\begin{aligned}-(\alpha\lambda+\mu)P_{j-1}^{k+1}+(1+2\alpha\lambda)P_{j}^{k+1}-(\alpha\lambda-\mu)P_{j+1}^{k+1}&=\\ \left(\alpha'\lambda-\mu\right)P_{j-1}^{k}+\left(1-2\alpha'\lambda\right)P_{j}^{k}+\left(\alpha'\lambda+\mu\right)P_{j+1}^{k}&\end{aligned} \tag{3.20}$$

Here, a is a control parameter for the solution stability, $\alpha'=1-\alpha,\lambda=C_v\Delta\sigma/(\Delta\tau)^2$, and $\mu=0_v/2\Delta\tau$. It is selected as $a=0.5$ in ITUBOOM. Then, it can be reduced into a matrix form:

$$\mathrm{A}_v\mathrm{P}^{k+1}=\mathrm{B}_v\mathrm{P}^{k} \tag{3.21}$$

where $\mathbf{A}_v$ and $\mathbf{B}_v$ matrices are:

$$\mathbf{A}_v=\begin{pmatrix}1 & 0 & & & \\ -(\alpha\lambda+\mu) & (1+2\alpha\lambda) & -(\alpha\lambda-\mu) & & \\ & \ddots & \ddots & \ddots & \\ & & -(\alpha\lambda+\mu) & (1+2\alpha\lambda) & -(\alpha\lambda-\mu)\\ & & & 0 & 1\end{pmatrix} \tag{3.22}$$

$$\mathbf{B}_v=\begin{pmatrix}1 & 0 & & & \\ (\alpha'\lambda-\mu) & (1-2\alpha'\lambda) & (\alpha'\lambda+\mu) & & \\ & \ddots & \ddots & \ddots & \\ & & (\alpha'\lambda-\mu) & (1-2\alpha'\lambda) & (\alpha'\lambda+\mu)\\ & & & 0 & 1\end{pmatrix} \tag{3.23}$$

Here, the dimensionless dispersion parameter can be defined as:

$$C_v=\frac{\Delta c_v\tau_v\omega_0^2\bar{x}}{c_0^2}=\alpha_v\bar{x} \tag{3.24}$$

$\alpha_v\bar{x}$ in the right-hand of the Eq. 3.24 can be calculated by superposition of Oxygen and Nitrogen. By using dispersion law and semi-empirical relations, $\alpha_O\bar{x}$ and $\alpha_N\bar{x}$ can be determined as follows.

$$\alpha_v = B_v \frac{f_{r,v} f^2}{f^2 + f_{r,v}^2} \tag{3.25}$$

where $f_{r,v}$ is the relaxation frequency:

$$f_{r,\mathrm{O}_2} = 1/\left(2\pi\tau_{\mathrm{O}_2}\right) = \left(p/p_{s0}\right)\left(24 + 4.04\times 10^4 h(0.02+h)/(0.391+h)\right) \tag{3.26}$$

$$\begin{gathered} f_{r,\,\mathrm{N}_2} = 1/\left(2\pi\tau_{\mathrm{N}_2}\right) = p/p_{s0}\left(T_0/T\right)^{1/2}\times \\ \left(9 + 280h\times\exp\left\{-4.17\left[\left(T_0/T\right)^{1/3} - 1\right]\right\}\right. \end{gathered} \tag{3.27}$$

In these equations, h is the absolute humidity in % to be determined from relative humidity h_r.

$$h = h_r\left(p_{\mathrm{sat}}/p_{s0}\right)/\left(p/p_{s0}\right) = p_{s0}\left(h_r/p\right)\left(p_{\mathrm{sat}}/p_{s0}\right)\% \tag{3.28}$$

The saturation vapor pressure, p_{sat} can be calculated from temperature.

$$\log_{10}\left[p_{sat}/p_{s0}\right] = -6.8346\left(\frac{T_0}{T}\right)^{1.261} + 4.6151 \tag{3.29}$$

In Equ. 3.25, B_v can be given with the following relation.

$$B_O = 0.01275\left(\frac{T}{T_0}\right)^{-5/2} e^{-2239.1/T} \tag{3.30}$$

$$B_N = 0.1068\left(\frac{T}{T_0}\right)^{-5/2} e^{-3352/T} \tag{3.31}$$

In ITUBOOM, two flags can be defined by the user to switch off both thermoviscous attenuation and vibrational relaxation.

3.4.1.4 Stratification and spreading

The last two terms of equation (3.6) are basically scaling terms due to the atmospheric stratification and geometric spreading. The following relations are used to solve these two terms.

$$P(\sigma+\Delta\sigma,\tau) = \sqrt{\frac{S(\sigma)}{S(\sigma+\Delta\sigma)}}P(\sigma,\tau) \tag{3.32}$$

$$P(\sigma+\Delta\sigma,\tau) = \sqrt{\frac{\left(\rho_0 c_0\right)|_{\sigma+\Delta\sigma}}{\left(\rho_0 c_0\right)|_{\sigma}}}P(\sigma,\tau) \tag{3.33}$$

Here, the ambient density and speed of sound are calculated from provided temperature profile by the user. A linear interpolation is used to find the temperature at the current altitude.

3.4.1.5 Step size

There are several criteria for the step size restriction. Keeping the step size too small results in a huge computation time. Therefore, the following restriction in equation (3.34) is applied during propagation. After each calculation step, the algorithm controls the next step size dynamically.

$$\begin{aligned}\Delta\sigma_{max} = min(0.2\frac{1}{max(\Delta P/\Delta\tau)}, 0.1\Gamma/N^2, 0.1\frac{1+M\theta_v^2}{C_v M},\\ \frac{2\pi}{\sqrt{M}\theta_v}, \frac{0.05A}{\partial A/\partial\sigma}, \frac{0.05\rho_0 c_0}{\partial\left(\rho_0 c_0\right)/\partial\sigma})\end{aligned} \tag{3.34}$$

As the solution reaches the ground, the pressure waveform is multiplied by a refraction factor on the ground. The default value of this refraction factor is 1.9 in ITUBOOM.

4. APPLICATIONS OF ITUBOOM

In this section, applications performed using ITUBOOM are presented. First, some validation studies are provided. Then, an investigation of the atmospheric effect on the sonic boom loudness is provided by using ITUBOOM. Then, the impact of numerical values on the sonic boom solution such as signal sampling is investigated. Finally, an application for the JWB model is provided with two levels of fidelity for flow solution.

4.1 Validation and Results

4.1.1 AXIEBODY, body of revolution

First, a comparison study is provided with NASA's sBOOM code for a body of revolution model from the second AIAA Sonic Boom Prediction Workshop for different signal locations. On-track near-field pressure signatures from SBPW are computed for AXIEBODY, a body of revolution, with two different locations such as 1 and 5 body lengths away, [66].

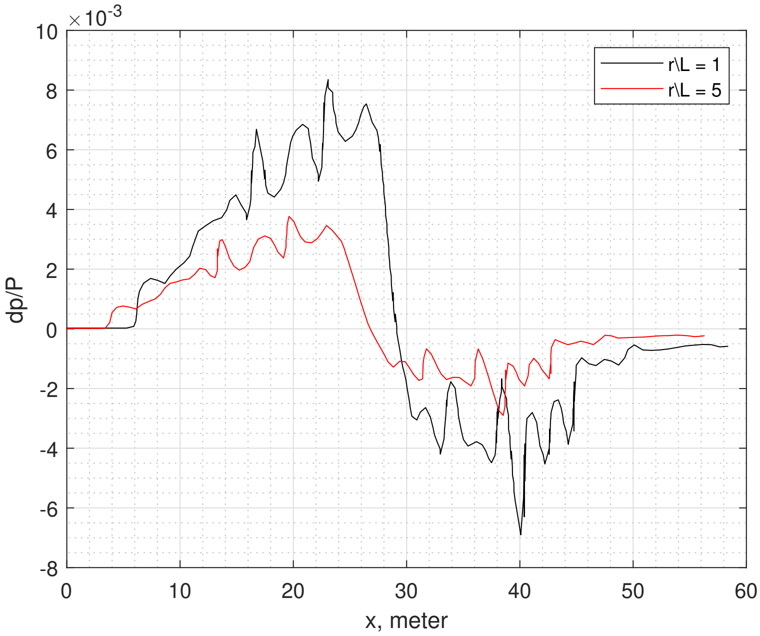

Figure 4.1 : Near-field pressure signatures at two different locations, AXIEBODY

Flight conditions are given as $M = 1.6$, 0 angle of attack, and 15760 m altitude. Figure 4.1 shows the near-field pressure signatures and Fig. 4.2 and 4.3 show ground signatures from sBOOM and ITUBOOM. Standard atmosphere conditions with zero wind profile are used for the propagation. Table 4.1 includes perceived loudness calculated with PyLdB and ground intersection coordinates.

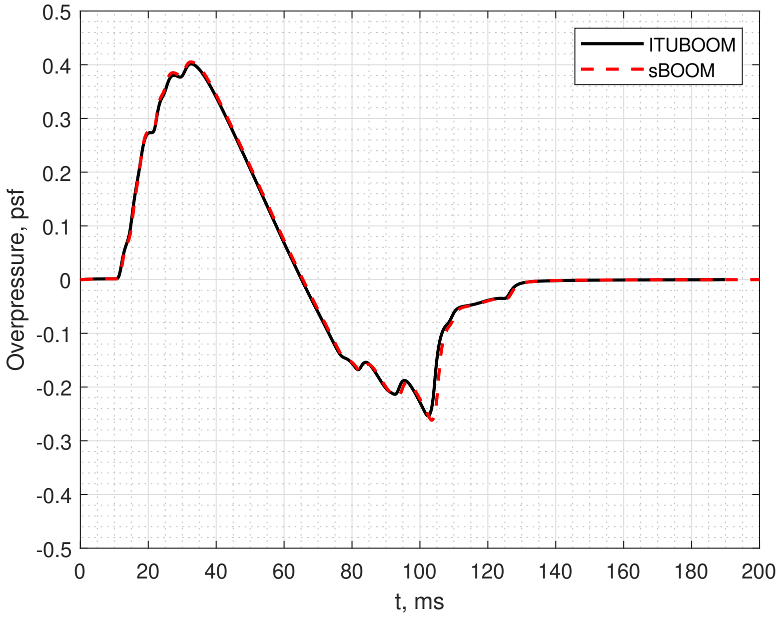

Figure 4.2 : Ground signatures, $r/L = 1$, AXIEBODY

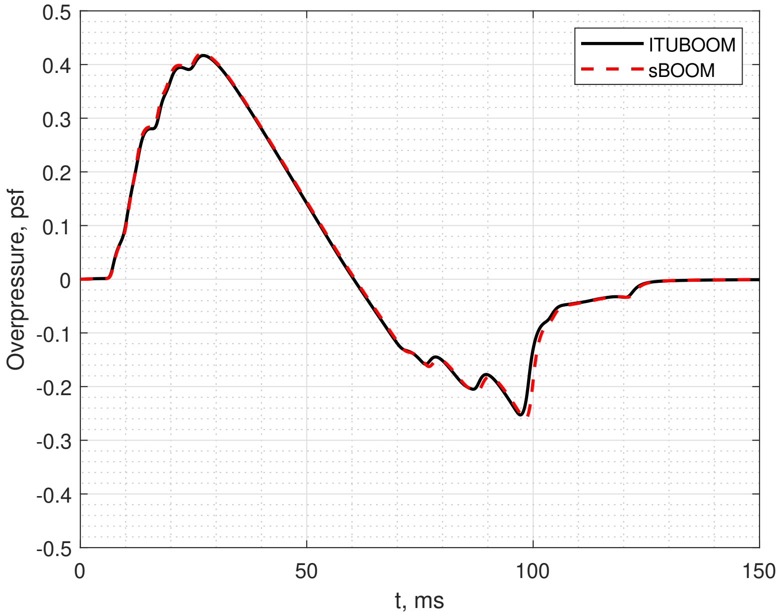

Figure 4.3 : Ground signatures, $r/L = 5$, AXIEBODY

Table 4.1 : AXIEBODY results from ITUBOOM and sBOOM

Case	Loudness, PLdB	Ground intersection x direction, m
ITUBOOM, $r/L = 1$	78.595	13887
sBOOM, $r/L = 1$	77.913	13878
ITUBOOM, $r/L = 5$	78.90	13887
sBOOM, $r/L = 5$	77.92	13878

4.1.2 JAXA wing-body case

Then, a wing-body combination, the JWB model, is used [101] for the validation. Flight conditions are the same with the AXIEBODY case, except the angle of attack which equals 3.07. The signal location is given as $r/L = 1$. Figure 4.4 depicts near-field pressure signatures and Fig. 4.5 shows ground signatures obtained from sBOOM and ITUBOOM with standard atmosphere propagation.

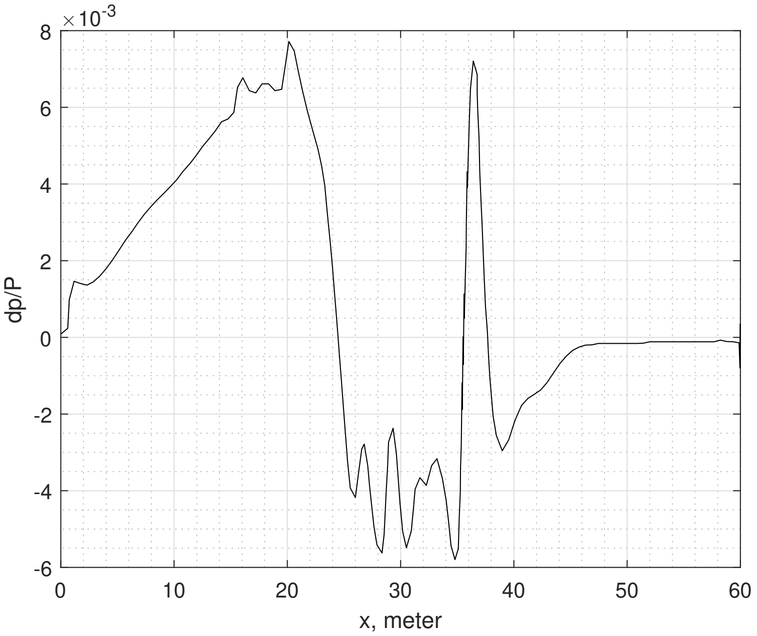

Figure 4.4 : Near-field signature, $r/L = 1$, JWB

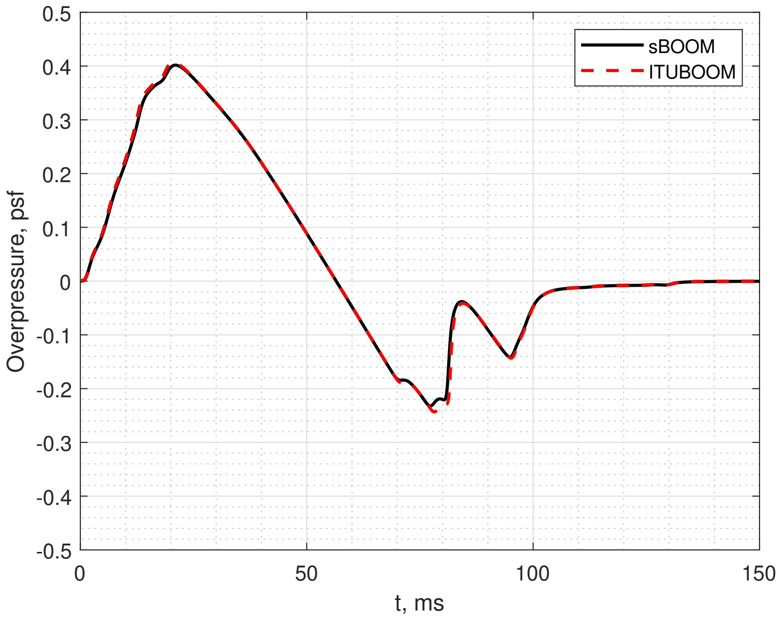

Figure 4.5 : Ground signatures, JWB

Two additional solutions are performed with 20^o and 40^o azimuth angles. Resultant loudness values are provided in Table 4.2.

Table 4.2 : JWB perceived loudness from ITUBOOM and sBOOM

Azimuth Angle	ITUBOOM	sBOOM
0 Degree	81.30063	80.66667
20 Degree	81.33086	78.06131
40 Degree	82.34975	80.14446

4.1.3 NASA C25D Low-boom demonstrator model

After, the NASA C25D low-boom demonstrator model from the second SBPW is used for the next validation. The aircraft geometry is illustrated in Fig. 2.6. Figure 4.6 shows the near-field pressure signature that is taken from $r_L = 5$. The propagation analysis is performed with both ITUBOOM and sBOOM for 55000 ft altitude and 1.6 Mach number. The standard atmosphere conditions are selected without wind. The resultant ground signatures are provided in Fig. 4.7 for comparison with sBOOM.

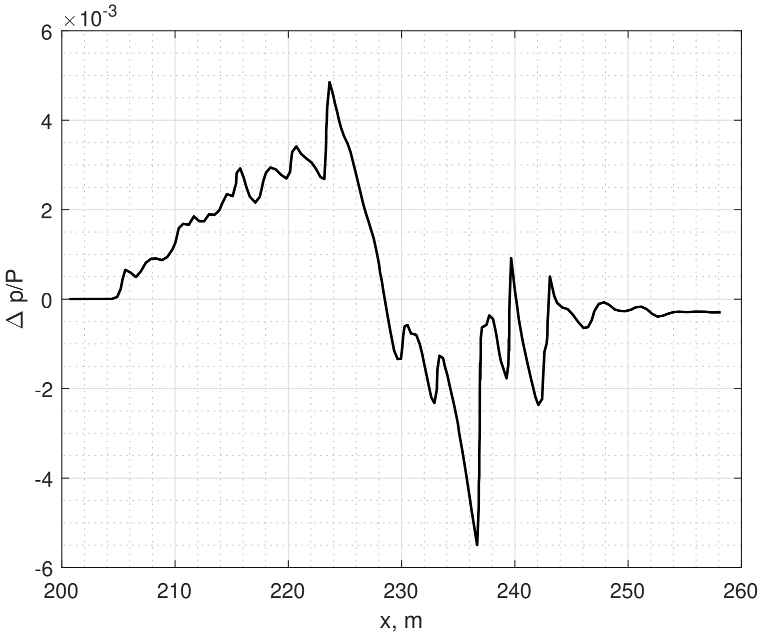

Figure 4.6 : Near-field pressure signature of NASA C25D aircraft, $r_L = 5$, NASA C25D

Figure 4.7 : Ground signatures comparison, NASA C25D

As seen from the comparison results, ITUBOOM is validated with respect to NASA's sBOOM program for various cases. In the following sections, several more advanced applications with ITUBOOM are presented.

4.2 Investigation of Parameter's Effects

The effect of input parameters on the loudness value is investigated. First, several atmosphere profiles are used to find changes in loudness value. Then, a convergence study is provided for the waveform sampling.

4.2.1 Atmospheric profiles

Atmospheric profiles are essential for the sonic boom loudness. Hutchinson and Bowersox [53] conducted an uncertainty quantification study with 9 different atmosphere profiles. A similar study is conducted with ITUBOOM to investigate the effect of atmosphere profiles with the JWB case. 4 different atmosphere profiles are selected from their study as shown in Fig. 4.8-4.11 where the first profile is the standard atmosphere. Then, a windy atmosphere profile is taken from [85] to demonstrate the effect of wind on propagation path, ground signature, and perceived loudness with atmosphere profile 1. Table 4.3 includes an arbitrary wind profile with respect to altitude. The resultant ground signatures are provided in Fig. 4.12 whereas loudness values and ground intersection coordinates are given in Table 4.4. 14000 m altitude is selected due to the altitude range of atmosphere profiles.

Table 4.3 : Arbitrary Wind profile

Altitude, m	X Wind, m/s	Y Wind, m/s
0	25	−50
5000	40	−80
10000	60	−120
20000	80	−160

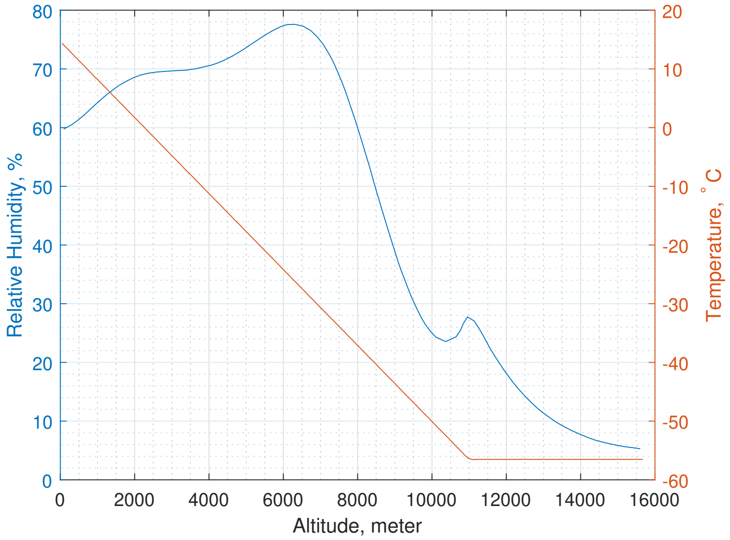

Figure 4.8 : Atmosphere profile 1

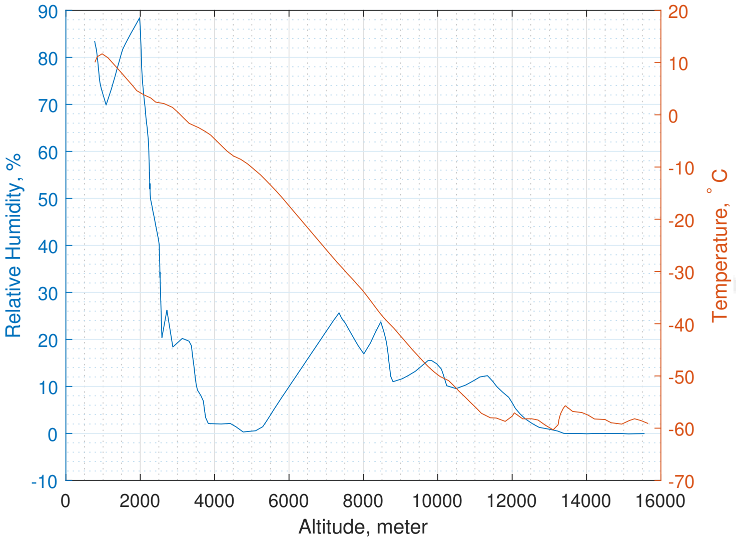

Figure 4.9 : Atmosphere profile 2

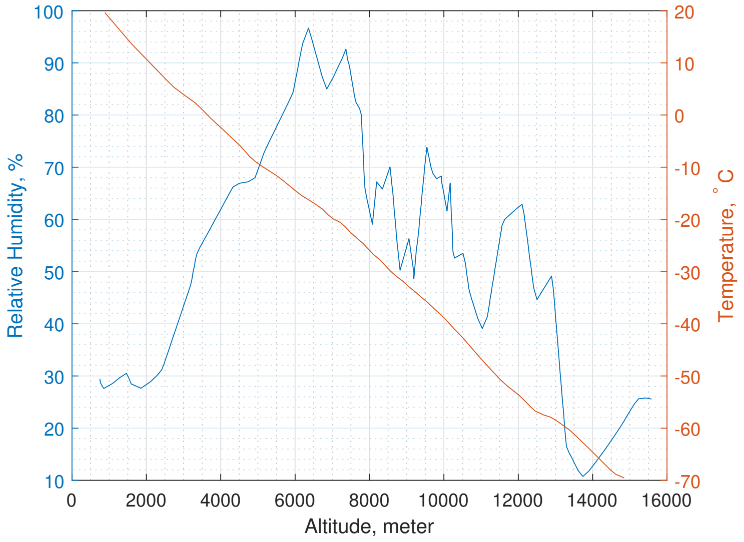

Figure 4.10 : Atmosphere profile 3

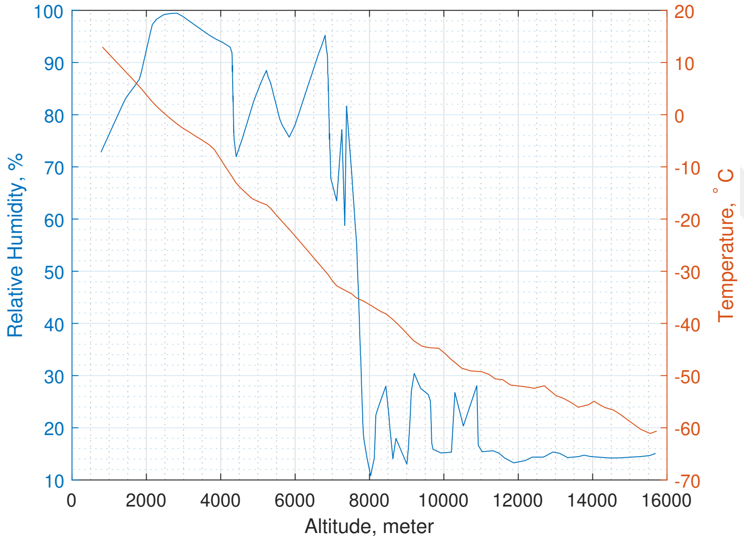

Figure 4.11 : Atmosphere profile 4

Table 4.4 : ITUBOOM results for different atmospheres

Profile	Loudness (PLdB)	Horizontal Propagation Distance, m
Atmosphere 1	86.784	5809
Atmosphere 2	82.4	5955
Atmosphere 3	88.27	6434
Atmosphere 4	88.48	5853
Windy Atmosphere	84.56	18310

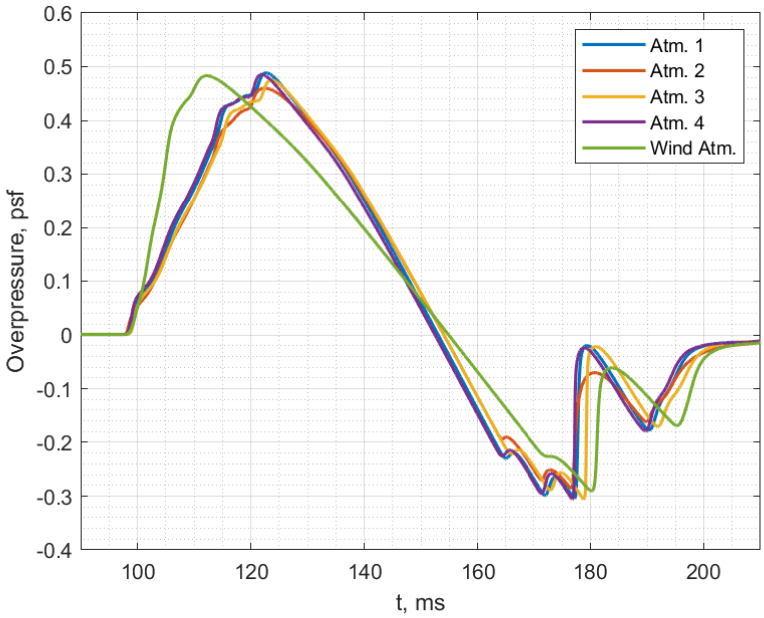

Figure 4.12 : Ground signatures with different atmosphere profiles

4.2.2 Waveform sampling

A convergence study is performed to determine the minimum number of points for the waveform. Near-field signature and flight conditions of the NASA C25D case are selected. 7 different analyses are conducted with several sampling rates as shown in Fig. 4.13. Change of loudness value with respect to the number of points on the waveform is also provided in Fig 4.14. It can be seen from the figures that 20000 points for the waveform are sufficient to make the solution grid independent.

ITUBOOM performs re-sampling for the pressure waveform according to user input. The linear interpolation function is called from Python's NumPy module for re-sampling.

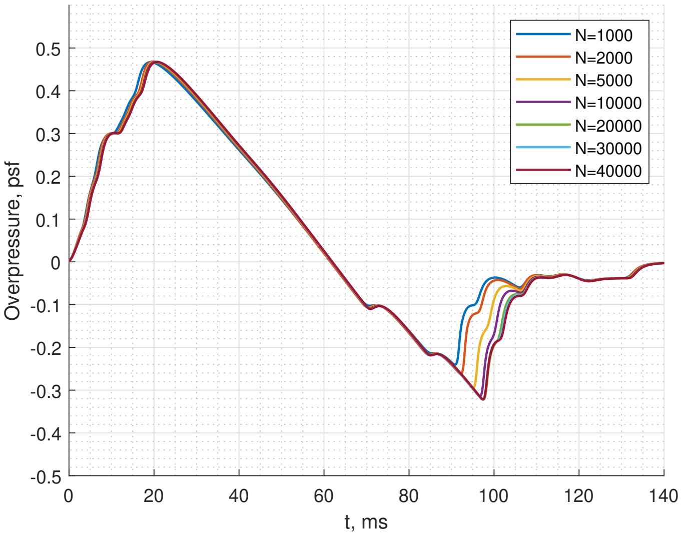

Figure 4.13 : Ground pressure signatures with various sampling rates, NASA C25D case

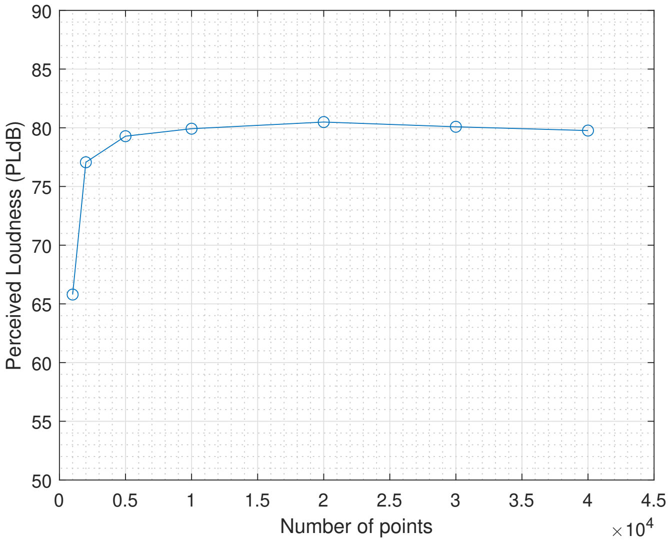

Figure 4.14 : PLdB values with respect to the number of points on the waveform, NASA C25D case

4.3 A Multi-fidelity Sonic Boom Prediction Application for the JAXA Wing-Body Aircraft

Previously, a comparative study showed that PAN AIR [95], a higher-order panel method program, is promising for the fast flow calculation of low-boom geometries [98]. Therefore, an application of a low-fidelity flow solution was performed by PAN AIR with a surface-slicing technique. Surface pressure signature distribution from PAN AIR result is used to calculate an equivalent area distribution for $M = 1.6$ flow at $\alpha = 3.07$ for JWB model [93]. The surface grid is illustrated in Fig. 4.15 and the resultant equivalent area distribution is provided in Fig. 4.16.

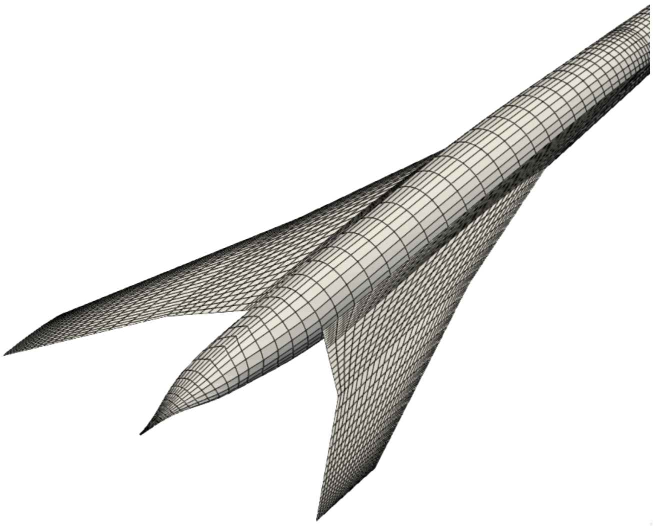

Figure 4.15 : JWB model surface grid

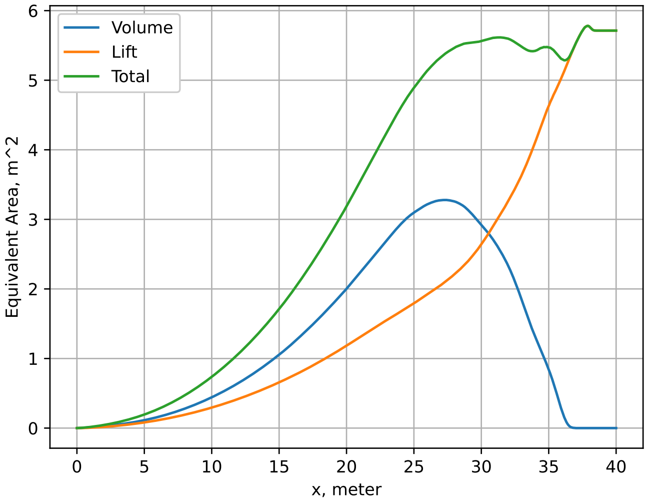

Figure 4.16 : Equivalent area distribution, JWB

Then, a near-field pressure signature was extracted from CFD output at 2 body lengths away from the aircraft with the SU2 CFD solver [99]. This pressure signature is presented in Fig. 4.17.

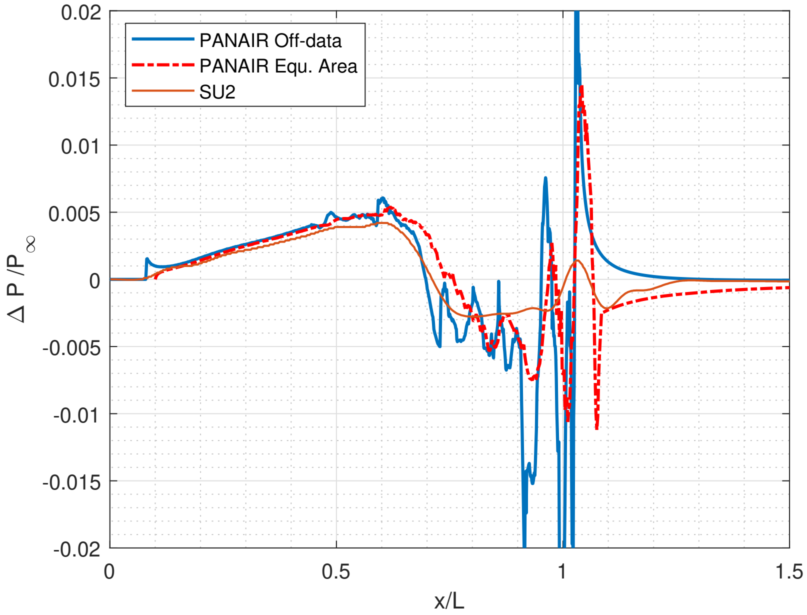

Figure 4.17 : Near-field pressure signature comparison, $r/L = 2$, JWB

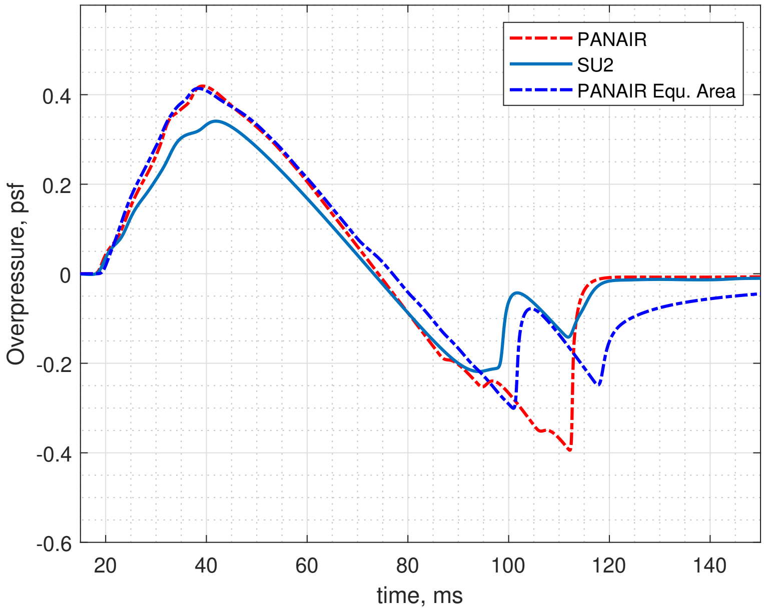

Figure 4.18 : Ground signature comparison computed by ITUBOOM for 52000 ft, JWB

In Fig. 4.17, three different pressure signatures are given. "PANAIR Equ. Area" curve represented the pressure signature obtained from equivalent area distribution calculation whereas the "PANAIR Off-data" curve is the PAN AIR output defined by the user. As seen, the pressure signature obtained from the equivalent area is more accurate than the program output. During the line integration for the lift contribution, an if condition can be added to eliminate non-physical data coming from due to the errors of the low-fidelity method. The ground signature calculated for 52000 ft altitude with standard atmosphere without wind is shown in Fig. 4.18 for three different near-field signatures. It can be seen in the figure that the pressure signature calculated from equivalent area distribution is closer to the CFD result rather than the PAN AIR's output signature.

5. CONCLUSION

A sonic boom prediction suite, named ITUBOOM, is developed in the content of this study by using Python programming language. Both linear and nonlinear methods are gathered into a single framework to be used in the design and optimization of low-boom supersonic aircraft. Implementation of the Lighthill F-function and equivalent area distribution from the surface of the aircraft are done successfully. This method enables using low-fidelity flow solvers such as panel solvers more efficiently in the optimization process as demonstrated in the last section of the applications. Also, equivalent area calculation is extended to any arbitrary aircraft shape with non-closed intersection surfaces on the slices. For wave propagation, an efficient algorithm is implemented to perform an equal area rule to eliminate multi-valued non-physical regions in the waveform.

In addition, a sonic boom propagation module utilizes the numerical solution of augmented Burgers equations in a ray tube coordinate system is implemented to calculate sonic boom loudness on the ground. The ray tracing technique enables us to perform analyzes with real atmosphere profiles. A validation study of a nonlinear propagation tool that includes thermoviscous attenuation and molecular relaxation is performed successfully with NASA's sBOOM program. Also, the effect of the atmosphere profiles is demonstrated for the perceived loudness on the ground.

As a future work, a target equivalent area distribution tool can be added to ITUBOOM. By using this tool, a target equivalent area can be generated by using lift and volume constraints at the beginning of the optimization. Instead of optimizing loudness on the ground, trying to minimize the difference between the current area distribution and to target area distribution can be more efficient. In addition, a reverse propagation module is planned to be added in ITUBOOM to calculate equivalent area distribution by using CFD-generated near-field pressure signature. This will allow more accurate optimization results rather than just using surface pressure distribution which does not include complex 3D flow structures near the aircraft. Finally, an adjoint formulation can be added to ITUBOOM to utilize adjoint optimization methods for sonic boom minimization.

In conclusion, we demonstrated the advantages of ITUBOOM with several applications. At the time this thesis is completed, there is no open-source nonlinear sonic boom prediction tool in the literature. Therefore, developing a state-of-the-art in-house prediction tool was essential for the efficient implementation into our MDO framework in ITU AeroMDO Lab.

REFERENCES

[1] **Division, N.A.S.**, (2021), Using NAS-Developed Tools to Quiet the Boom of Supersonic Flight, `https://www.nas.nasa.gov/pubs/stories/2021/feature_X-59.html`, [Online; accessed 05-November-2022].

[2] **SEEBASS, R.** (1969). Sonic boom theory., *Journal of Aircraft*, *6*(3), 177–184, `https://doi.org/10.2514/3.44032`.

[3] **Locey, L.L.** (2008). SONIC BOOM POSTPROCESSING FUNCTIONS TO SIMULATE ATMOSPHERIC TURBULENCE EFFECTS, *Ph.D. Dissertation*, The Pennsylvania State University.

[4] **AIAA**, (2022), ASA 2022 Special Focus Boom Session, `https://lbpw.larc.nasa.gov/?doing_wp_cron=1668191212.0171160697937011718750`, [Online; accessed 05-November-2022].

[5] **Park, M.A. and Morgenstern, J.M.** (2016). Summary and Statistical Analysis of the First AIAA Sonic Boom Prediction Workshop, *Journal of Aircraft*, *53*(2), 578–598, `https://doi.org/10.2514/1.c033449`.

[6] **Whitham, G.B.** (1956). On the propagation of weak shock waves, *Journal of Fluid Mechanics*, *1*(3), 290–318, `https://doi.org/10.1017/s0022112056000172`.

[7] **Walkden, F.** (1958). The Shock Pattern of a Wing-Body Combination, Far from the Flight Path, *Aeronautical Quarterly*, *9*(2), 164–194, `https://doi.org/10.1017/s0001925900001372`.

[8] **Jung, T.P.**, **Starkey, R.P. and Argrow, B.** (2015). Modified Linear Theory Sonic Booms Compared to Experimental and Numerical Results, *Journal of Aircraft*, *52*(6), 1821–1837, `https://doi.org/10.2514/1.c033088`.

[9] **Chambers, J.R.** (2005). *Innovation in Flight*, NASA, `https://history.nasa.gov/monograph39/mon39_a.pdf`.

[10] **FAA**, (2020), Supersonic Flight, `https://www.faa.gov/newsroom/supersonic-flight`, [Online; accessed 05-November-2022].

[11] **HAGLUND, G.** (1991). HSCT designs for reduced sonic boom, *Aircraft Design and Operations Meeting*, American Institute of Aeronautics and Astronautics, `https://doi.org/10.2514/6.1991-3103`.

[12] **Ribner, H.S. and Hubbard, H.H.** (1972). FOREWORD, *The Journal of the Acoustical Society of America*, *51*(2C), 671–671, `https://doi.org/10.1121/1.1912899`.

[13] **Rallabhandi, S. and Mavris, D.** (2005). Sonic Boom Minimization Using Improved Linearized Tools and Probabilistic Propagation, *43rd AIAA Aerospace Sciences Meeting and Exhibit*, American Institute of Aeronautics and Astronautics, `https://doi.org/10.2514/6.2005-1019`.

[14] **Farhat, C.**, **Maute, K.**, **Argrow, B. and Nikbay, M.** (2007). Shape Optimization Methodology for Reducing the Sonic Boom Initial Pressure Rise, *AIAA Journal*, *45*(5), 1007–1018.

[15] **Choi, S.**, **Alonso, J.J.**, **Kroo, I.M. and Wintzer, M.** (2008). Multifidelity Design Optimization of Low-Boom Supersonic Jets, *Journal of Aircraft*, *45*(1), 106–118, `https://doi.org/10.2514/1.28948`.

[16] **Rallabhandi, S.K. and Mavris, D.N.** (2007). Aircraft Geometry Design and Optimization for Sonic Boom Reduction, *Journal of Aircraft*, *44*(1), 35–47, `https://doi.org/10.2514/1.20456`.

[17] **Anderson, J.** (2010). *Fundamentals of Aerodynamics*, McGraw-Hill Education, `https://books.google.com/books?id=xwY8PgAACAAJ`.

[18] **Whitham, G.B.** (1952). The flow pattern of a supersonic projectile, *Communications on Pure and Applied Mathematics*, *5*(3), 301–348, `http://doi.wiley.com/10.1002/cpa.3160050305`.

[19] **Lighthill, M.** (1945). Supersonic flow past bodies of revolution, *In Aeronautical Research Commission, Reports and Memoranda*, *1*(2003).

[20] **Jung, T.P.** (2012). Modified Linear Theory Aircraft Design Tools and Sonic Boom Minimization Strategy Applied to Signature Freezing via F-function Lobe Balancing, *Ph.D. Dissertation*, University of Colorado.

[21] **LIGHTHILL, M.J.** (1948). SUPERSONIC FLOW PAST SLENDER BODIES OF REVOLUTION THE SLOPE OF WHOSE MERIDIAN SECTION IS DISCONTINUOUS, *The Quarterly Journal of Mechanics and Applied Mathematics*, *1*(1), 90–102, `https://doi.org/10.1093/qjmam/1.1.90`.

[22] **Gottlieb, J.J. and Ritzel, D.V.** (1988). Analytical study of sonic boom from supersonic projectiles, *Progress in Aerospace Sciences*, *25*(2), 131–188, `https://doi.org/10.1016/0376-0421(88)90006-1`.

[23] **McLean, F.E.** (1965). SOME NONASYMPTOTIC EFFECTS ON THE SONIC BOOM OF LARGE AIRPLANES, **Technical ReportNASA TN D-2877**, NATIONAL AERONAUTICS AND SPACE ADMINISTRATION.

[24] **Hayes, W.D.**, **Haefeli, R.C. and Kulsrud, H.E.** (1969). Sonic Boom Propagation In A Stratified Atmosphere, With Computer Program, **Technical ReportNASA CR-1299**, NASA Contractor Report.

[25] **CHEUNG, S.**, **EDWARDS, T. and LAWRENCE, S.** (1990). Application of CFD to sonic boom near and mid flow-field prediction, *13th Aeroacoustics Conference*, American Institute of Aeronautics and Astronautics, `https://doi.org/10.2514/6.1990-3999`.

[26] **PAGE, J. and PLOTKIN, K.** (1991). An efficient method for incorporating computational fluid dynamics into sonic boom prediction, *9th Applied Aerodynamics Conference*, American Institute of Aeronautics and Astronautics, `https://doi.org/10.2514/6.1991-3275`.

[27] **Nikbay, M.** (2002). Coupled Sensitivity Analysis by Discrete-Analytical Direct and Adjoint Methods with Applications to Aeroelastic Optimization and Sonic Boom Minimization, *Ph.D. Dissertation*, University of Colorado.

[28] **Rallabhandi, S.K. and Mavris, D.N.** (2007). New Computational Procedure for Incorporating Computational Fluid Dynamics into Sonic Boom Prediction, *Journal of Aircraft*, *44*(6), 1964–1971, `https://doi.org/10.2514/1.32035`.

[29] **Farhat, C.**, **Maute, K.**, **Argrow, B. and Nikbay, M.** (2007). Shape Optimization Methodology for Reducing the Sonic Boom Initial Pressure Rise, *AIAA Journal*, *45*(5), 1007–1018.

[30] **Onyeonwu, R.O.** (1971). The Effects of Wind And Temperature Gradients on Sonic Boom Corridrs, *Ph.D. Dissertation*, University of Toronto.

[31] **Barger, R.L.** (1968). Development of Sonic-Boom Signatures in A Stratified Atmosphere, **Technical Report**, NASA Technical Note.

[32] **Keller, J.B.** (1954). Geometrical Acoustics. I. The Theory of Weak Shock Waves, *Journal of Applied Physics*, *25*(8), 938–947, `https://doi.org/10.1063/1.1721807`.

[33] **Kulowski, A.** (1985). Algorithmic representation of the ray tracing technique, *Applied Acoustics*, *18*(6), 449–469, `https://doi.org/10.1016/0003-682x(85)90024-6`.

[34] **Thomas, C.L. and Field, M.** (1972). PRESSURE SIGNATURES BY THE WAVEFORM PARAMETER METHOD, 35.

[35] **Lonzaga, J.B.** (2019). Recent Enhancements to NASA's PCBoom Sonic Boom Propagation Code, *AIAA Aviation 2019 Forum*, American Institute of Aeronautics and Astronautics, `https://doi.org/10.2514/6.2019-3386`.

[36] **PLOTKIN, K.** (1989). Review of sonic boom theory, *12th Aeroacoustic Conference*, American Institute of Aeronautics and Astronautics, `https://doi.org/10.2514/6.1989-1105`.

[37] **Pierce, A.D.** (2019). *Acoustics: An Introduction to Its Physical Principles and Applications*, Springer International Publishing, Cham, `http://link.springer.com/10.1007/978-3-030-11214-1`.

[38] **Blokhintzev, D.** (1946). The Propagation of Sound in an Inhomogeneous and Moving Medium I, *The Journal of the Acoustical Society of America*, *18*(2), 322–328, `https://doi.org/10.1121/1.1916368`.

[39] **Groves, G.** (1955). Geometrical theory of sound propagation in the atmosphere, *Journal of Atmospheric and Terrestrial Physics*, *7*, 113–127, `https://doi.org/10.1016/0021-9169(55)90119-7`.

[40] **Ockendon, H. and Spence, D.A.** (1969). Non-linear wave propagation in a relaxing gas, *Journal of Fluid Mechanics*, *39*(2), 329–345, `https://doi.org/10.1017/s0022112069002205`.

[41] **Blackstock, D.** (2000). *Fundamentals of Physical Acoustics*, A Wiley-Interscience publication, Wiley, `https://books.google.com/books?id=5N-ZDwAAQBAJ`.

[42] **Lee, Y.S. and Hamilton, M.F.** (1995). Time-domain modeling of pulsed finite-amplitude sound beams, *The Journal of the Acoustical Society of America*, *97*(2), 906–917, `https://doi.org/10.1121/1.412135`.

[43] **Pestorius, F.M.** (1973). Propagation of plane acoustic noise of finite amplitude, **Technical ReportARL-TR-73-23**, Applied Research Laboratories, The University of Texas at Austin.

[44] **Anderson, M.O.** (1974). The propagation of a spherical N wave in an absorbing medium and its diffraction by a circular aperture, **Technical ReportARL-TR-74-25**, Applied Research Laboratories, The University of Texas at Austin.

[45] **Orenstein, L.B.** (1982). The Rise Time of N Waves Produced by Sparks, **Technical ReportARL-TR-82-51**, Applied Research Laboratories, The University of Texas at Austin.

[46] **Robinson, L.D.** (1991). Sonic boom propagation through an inhomogeneous windy atmosphere, *Ph.D. Dissertation*, The University of Texas at Austin.

[47] **CLEVELAND, R.O.** (1995). PROPAGATION OF SONIC BOOMS THROUGH A REAL, STRATIFIED ATMOSPHERE, *Ph.D. Dissertation*, THE UNIVERSITY OF TEXAS AT AUSTIN.

[48] **Cleveland, R.O., Chambers, J.P., Bass, H.E., Raspet, R., Blackstock, D.T. and Hamilton, M.F.** (1996). Comparison of computer codes for the propagation of sonic boom waveforms through isothermal atmospheres, *The Journal of the Acoustical Society of America*, *100*(5), 3017–3027, `https://doi.org/10.1121/1.417113`.

[49] **Hammerton, P.** (2001). Effect of molecular relaxation on the propagation of sonic booms through a stratified atmosphere, *Wave Motion*, *33*(4), 359–377, `https://doi.org/10.1016/s0165-2125(00)00078-0`.

[50] **Blanc-Benon, P.**, **Lipkens, B.**, **Dallois, L.**, **Hamilton, M.F. and Blackstock, D.T.** (2002). Propagation of finite amplitude sound through turbulence: Modeling with geometrical acoustics and the parabolic approximation, *The Journal of the Acoustical Society of America*, *111*(1), 487–498, `https://doi.org/10.1121/1.1404378`.

[51] **Pilon, A.R.** (2007). Spectrally Accurate Prediction of Sonic Boom Signals, *AIAA Journal*, *45*(9), 2149–2156, `https://doi.org/10.2514/1.28159`.

[52] **Qiao, J.L.**, **Han, Z.**, **Song, W. and Song, B.F.** (2019). Development of Sonic Boom Prediction Code for Supersonic Transports Based on Augmented Burgers Equation, *AIAA Aviation 2019 Forum*, American Institute of Aeronautics and Astronautics, `https://doi.org/10.2514/6.2019-3571`.

[53] **Hutchinson, A.D. and Bowersox, R.D.** (2021). A Sonic Boom Propagation Code for Studying Atmospheric Effects and Uncertainties, *AIAA Scitech 2021 Forum*, American Institute of Aeronautics and Astronautics, `https://doi.org/10.2514/6.2021-0010`.

[54] **Fujino, K.**, **Kikuchi, R.**, **Shimoyama, K.**, **Obayashi, S. and Makino, Y.** (2017). Effects of Uncertainties in Atmospheric Turbulence and Weather Predictions on Sonic Boom, *55th AIAA Aerospace Sciences Meeting*, American Institute of Aeronautics and Astronautics, `https://doi.org/10.2514/6.2017-0280`.

[55] **Rallabhandi, S.K.** (2011). Advanced sonic boom prediction using the augmented burgers equation, *Journal of Aircraft*, *48*(4), 1245–1253.

[56] **Stout, T.A.** (2018). Simulation of N-wave and Shaped Supersonic Signature Turbulent Variations, *Ph.D. Dissertation*, The Pennsylvania State University.

[57] **Takeno, J.**, **Misaka, T.**, **Shimoyama, K. and Obayashi, S.** (2015). Analysis of sonic boom propagation based on the KZK equation, *53rd AIAA Aerospace Sciences Meeting*, American Institute of Aeronautics and Astronautics, `https://doi.org/10.2514/6.2015-0745`.

[58] **Yamashita, R. and Suzuki, K.** (2014). Full-Field Sonic Boom Simulation in Real Atmosphere, *32nd AIAA Applied Aerodynamics Conference*, American Institute of Aeronautics and Astronautics, `https://doi.org/10.2514/6.2014-2269`.

[59] **Yamashita, R. and Suzuki, K.** (2016). Full-Field Sonic Boom Simulation in Stratified Atmosphere, *AIAA Journal*, *54*(10), 3223–3231, `https://doi.org/10.2514/1.j054581`.

[60] **Yamashita, R.**, **Makino, Y. and Roe, P.L.** (2022). Fast Full-Field Simulation of Sonic Boom Using a Space Marching Method, *AIAA Journal*, *60*(7), 4103–4112, `https://doi.org/10.2514/1.j061363`.

[61] **QIAO, J.**, **HAN, Z.**, **ZHANG, L.**, **SONG, W. and SONG, B.** (2022). Far-field sonic boom prediction considering atmospheric turbulence effects: An improved approach, *Chinese Journal of Aeronautics*, *35*(9), 208–225, `https://doi.org/10.1016/j.cja.2022.01.013`.

[62] **Kaori, K.** (2004). Secondary Sonic Boom, *Ph.D. Dissertation*, University of Oxford.

[63] **Plotkin, K.J.** (2002). State of the art of sonic boom modeling, *The Journal of the Acoustical Society of America*, *111*(1), 530–536, `https://doi.org/10.1121/1.1379075`.

[64] **Salamone, J.A.**, **Sparrow, V.W. and Plotkin, K.J.** (2013). Solution of the Lossy Nonlinear Tricomi Equation Applied to Sonic Boom Focusing, *AIAA Journal*, *51*(7), 1745–1754, `https://doi.org/10.2514/1.j052171`.

[65] **Park, M.A. and Morgenstern, J.M.** (2014). Summary and Statistical Analysis of the First AIAA Sonic Boom Prediction Workshop, *32nd AIAA Applied Aerodynamics Conference*, American Institute of Aeronautics and Astronautics, `https://doi.org/10.2514/6.2014-2006`.

[66] **Rallabhandi, S.K. and Loubeau, A.** (2019). Summary of Propagation Cases of the Second AIAA Sonic Boom Prediction Workshop, *Journal of Aircraft*, *56*(3), 876–895, `https://doi.org/10.2514/1.c034805`.

[67] **Rallabhandi, S.K. and Loubeau, A.** (2022). Summary of Propagation Cases of the Third AIAA Sonic Boom Prediction Workshop, *Journal of Aircraft*, *59*(3), 578–594, `https://doi.org/10.2514/1.c036327`.

[68] **David A. McCurdy** (1994). High-Speed Research: 1994 Sonic Boom Workshop Configuration Design, Analysis, and Testing, **Technical ReportCP-1999-209699**, NASA Langley Research Center.

[69] **Daniel G. Baize** (1995). 1995 NASA High-Speed Research Program Sonic Boom Workshop Volume I, **Technical ReportNASA Conference Publication 3335**, NASA Langley Research Center.

[70] **Daniel G. Baize** (1995). 1995 NASA High-Speed Research Program Sonic Boom Workshop Volume II-Configuration Design, Analysis, and Testing, **Technical ReportCP-1999-209520**, NASA Langley Research Center.

[71] **A. R. Seebass** (1967). Sonic Boom Research, **Technical ReportNASA SP-147**, National Aeronautics and Space Administration.

[72] **Ira R. Schwartz** (1968). Second Conference on Sonic Boom Research, **Technical ReportNASA SP-180**, National Aeronautics and Space Administration.

[73] **Jones, L.B.** (1961). Lower Bounds for Sonic Bangs, *The Journal of the Royal Aeronautical Society*, *65*(606), 433–436, `https://doi.org/10.1017/s0368393100074757`.

[74] **Seebass, R. and George, A.R.** (1972). Sonic-Boom Minimization, *The Journal of the Acoustical Society of America*, *51*(2C), 686–694, `https://doi.org/10.1121/1.1912902`.

[75] **GEORGE, A.R. and PLOTKIN, K.J.** (1969). Sonic boom waveforms and amplitudes in a real atmosphere, *AIAA Journal*, *7*(10), 1978–1981, `https://doi.org/10.2514/3.5491`.

[76] **Darden, C.M.** (1977). Sonic Boom Theory: Its Status in Prediction and Minimization, *Journal of Aircraft*, *14*(6), 569–576, `https://doi.org/10.2514/3.58822`.

[77] **Seebass, R. and Argrow, B.** (1998). Sonic boom minimization revisited, *2nd AIAA, Theoretical Fluid Mechanics Meeting*, American Institute of Aeronautics and Astronautics, `https://doi.org/10.2514/6.1998-2956`.

[78] **Alonso, J.**, **Jameson, A. and Kroo, I.** (2002). Advanced algorithms for design and optimization of Quiet Supersonic Platforms, *40th AIAA Aerospace Sciences Meeting Exhibit*, American Institute of Aeronautics and Astronautics, `https://doi.org/10.2514/6.2002-144`.

[79] **Bowersox, R.**, **Wilson, E. and Karr, C.** (2003). Minimization of Sonic Boom with Genetic Algorithms, *41st Aerospace Sciences Meeting and Exhibit*, American Institute of Aeronautics and Astronautics, `https://doi.org/10.2514/6.2003-463`.

[80] **Makino, Y. and Kroo, I.** (2006). Robust Objective Functions for Sonic-Boom Minimization, *Journal of Aircraft*, *43*(5), 1301–1306, `https://doi.org/10.2514/1.19442`.

[81] **Rallabhandi, S. and Mavris, D.** (2006). Design and Analysis of Supersonic Business Jet Concepts, *6th AIAA Aviation Technology, Integration and Operations Conference (ATIO)*, American Institute of Aeronautics and Astronautics, `https://doi.org/10.2514/6.2006-7702`.

[82] **Li, W.**, **Shields, E. and Geiselhart, K.** (2010). A Mixed-Fidelity Approach for Design of Low-Boom Supersonic Aircraft, *48th AIAA Aerospace Sciences Meeting Including the New Horizons Forum and Aerospace Exposition*, American Institute of Aeronautics and Astronautics, `https://doi.org/10.2514/6.2010-845`.

[83] **Ordaz, I. and Rallabhandi, S.** (2010). Boom Minimization Framework for Supersonic Aircraft Using CFD Analysis, *48th AIAA Aerospace Sciences Meeting Including the New Horizons Forum and Aerospace Exposition*, American Institute of Aeronautics and Astronautics, `https://doi.org/10.2514/6.2010-1506`.

[84] **Maute, K.**, **Farhat, C.**, **Argrow, B. and Nikbay, M.** (2008). Sonic boom mitigation via shape optimization using an adjoint method and application to a supersonic fighter aircraft, *European Journal of Computational Mechanics*, *17*(1-2), 217–243, `https://doi.org/10.3166/remn.17.217-243`.

[85] **Rallabhandi, S.** (2011). Sonic Boom Adjoint Methodology and its Applications, *29th AIAA Applied Aerodynamics Conference*, American Institute of Aeronautics and Astronautics, `https://doi.org/10.2514/6.2011-3497`.

[86] **Li, W. and Shields, E.** (2011). Generation of Parametric Equivalent-Area Targets for Design of Low-Boom Supersonic Concepts, *49th AIAA Aerospace Sciences Meeting including the New Horizons Forum and Aerospace Exposition*, American Institute of Aeronautics and Astronautics, `https://doi.org/10.2514/6.2011-462`.

[87] **Li, W. and Rallabhandi, S.** (2014). Inverse Design of Low-Boom Supersonic Concepts Using Reversed Equivalent-Area Targets, *Journal of Aircraft*, *51*(1), 29–36, `https://doi.org/10.2514/1.c031551`.

[88] **Li, W. and Geiselhart, K.** (2021). Integration of Low-Fidelity MDO and CFD-Based Redesign of Low-Boom Supersonic Transports, *AIAA Journal*, *59*(10), 3923–3936, `https://doi.org/10.2514/1.j060368`.

[89] **Li, W. and Geiselhart, K.** (2021). Multidisciplinary Design Optimization of Low-Boom Supersonic Aircraft with Mission Constraints, *AIAA Journal*, *59*(1), 165–179, `https://doi.org/10.2514/1.j059237`.

[90] **Domenic J. Maglieri, Percy J. Bobbitt, Kenneth J. Plotkin and Kevin P. Shepherd, Peter G. Coen, and David M. Richwine** (2014). Sonic Boom Six Decades of Research, **Technical ReportSP-2014-622**, NASA Langley Research Center.

[91] **Bolander, C.R. and Hunsaker, D.F.** (2020). Near-field Pressure Signature Splicing for Low-Fidelity Design Space Exploration of Supersonic Aircraft, *AIAA Scitech 2020 Forum*, American Institute of Aeronautics and Astronautics, `https://doi.org/10.2514/6.2020-0789`.

[92] **Giblette, T. and Hunsaker, D.F.** (2019). Prediction of Sonic Boom Loudness Using High-Order Panel Methods for the Near-Field Solution, *AIAA Scitech 2019 Forum*, American Institute of Aeronautics and Astronautics, `https://doi.org/10.2514/6.2019-0605`.

[93] **Ueno, A.**, **Kanamori, M. and Makino, Y.** (2016). Multi-fidelity Low-boom Design Based on Near-field Pressure Signature, *54th AIAA Aerospace Sciences Meeting*, American Institute of Aeronautics and Astronautics, `https://doi.org/10.2514/6.2016-2033`.

[94] **Anderson, J.D.** (2016). *Fundamentals of aerodynamics*, McGraw-Hill Education, Columbus, OH, 6 edition.

[95] **Carmichael1981, R. and Erickson, L.** (1981). PAN AIR - A higher order panel method for predicting subsonic or supersonic linear potential flows about arbitrary configurations, *14th Fluid and Plasma Dynamics Conference*, June 1981, American Institute of Aeronautics and Astronautics.

[96] **Goates, C.D. and Hunsaker, D.F.** (2022). Development of a Subsonic-Supersonic, Unstructured Panel Method, *AIAA SCITECH 2022 Forum*, American Institute of Aeronautics and Astronautics, `https://doi.org/10.2514/6.2022-0403`.

[97] **Davis, J. and Marshall, D.** (2020). A Higher-Order Method Implemented in an Unstructured Panel Code to Model Linearized Supersonic Flows, *AIAA Scitech 2020 Forum*, American Institute of Aeronautics and Astronautics, `https://doi.org/10.2514/6.2020-1748`.

[98] **Demiroglu, Y. and Nikbay, M.** (2021). A COMPARATIVE STUDY ON MULTI-FIDELITY SONIC BOOM PREDICTION FOR A SUPERSONIC AIRCRAFT, *AeroBest 2021 - International Conference on Multidisciplinary Design Optimization of Aerospace Systems*, ECCOMAS.

[99] **Economon, T.D.**, **Palacios, F.**, **Copeland, S.R.**, **Lukaczyk, T.W. and Alonso, J.J.** (2016). SU2: An Open-Source Suite for Multiphysics Simulation and Design, *AIAA Journal*, *54*(3), 828–846, `https://doi.org/10.2514/1.j053813`.

[100] **Nayani, S.** (2013). Evaluation of Grid Modification Methods for On- and Off-Track Sonic Boom Analysis, *51st AIAA Aerospace Sciences Meeting including the New Horizons Forum and Aerospace Exposition*, American Institute of Aeronautics and Astronautics, `https://doi.org/10.2514/6.2013-798`.

[101] **Park, M.A. and Nemec, M.** (2019). Nearfield Summary and Statistical Analysis of the Second AIAA Sonic Boom Prediction Workshop, *Journal of Aircraft*, *56*(3), 851–875, `https://doi.org/10.2514/1.c034866`.

[102] **Vanharen, J.**, **Loseille, A.**, **Alauzet, F. and Park, M.A.** (2022). Near-Field Anisotropic Mesh Adaptation for the Third AIAA Sonic Boom Workshop, *Journal of Aircraft*, *59*(3), 683–696, `https://doi.org/10.2514/1.c036502`.

[103] **Ordaz, I.**, **Wintzer, M. and Rallabhandi, S.K.** (2015). Full-Carpet Design of a Low-Boom Demonstrator Concept, *33rd AIAA Applied Aerodynamics Conference*, American Institute of Aeronautics and Astronautics, `https://doi.org/10.2514/6.2015-2261`.

[104] **Tekaslan, H.E.**, **Demiroglu, Y. and Nikbay, M.** (2022). Surrogate Unsteady Aerodynamic Modeling with Autoencoders and LSTM Networks, *AIAA SCITECH 2022 Forum*, American Institute of Aeronautics and Astronautics, `https://doi.org/10.2514/6.2022-0508`.

[105] **Ritzel, D.V. and Gottlieb, J.J.** (1988). Numerical evaluation of Whitham's F-function for supersonic projectiles, *AIAA Journal*, *26*(2), 244–247, `https://doi.org/10.2514/3.9880`.

[106] **Bolander, C.R.**, **Hunsaker, D.F.**, **Shen, H. and Carpenter, F.L.** (2019). Procedure for the Calculation of the Perceived Loudness of Sonic Booms, *AIAA Scitech 2019 Forum*, American Institute of Aeronautics and Astronautics, `https://doi.org/10.2514/6.2019-2091`.

[107] **Yamamoto, M.**, **Hashimoto, A.**, **Aoyama, T. and Sakai, T.** (2015). A unified approach to an augmented Burgers equation for the propagation of sonic booms, *The Journal of the Acoustical Society of America*, *137*(4), 1857–1866, `https://doi.org/10.1121/1.4916833`.

CURRICULUM VITAE

Name SURNAME: Yusuf Demiroglu

EDUCATION:

- **B.Sc.:** 2019, Istanbul Technical University, Faculty of Aeronautics and Astronautics, Department of Astronautical Engineering

PROFESSIONAL EXPERIENCE:

- 2021-2022, ITU Faculty of Aeronautics and Astronautics, Graduate Teaching Assistant.
- 2019-2022, ITU Aerospace Multidisciplinary Design Optimization Laboratory, Graduate Research Assistant.

PUBLICATIONS FROM THESIS:

- **Demiroglu Y.**, Nikbay M. “Development of A Sonic Boom Propagation Code For Low-Boom Supersonic Aircraft Design and Optimization” *AIAA Scitech Forum*, Washington DC USA, 23-27 January 2023.
- Tekaslan E., Yildiz, Ş., **Demiroglu Y.**, Nikbay M. “Implementation of Multidisciplinary Multi-Fidelity Uncertainty Quantification Methods in Sonic Boom Prediction” *AIAA Journal of Aircraft*, https://doi.org/10.2514/1.C036962.
- Nikbay M., Kilic D., Cakmak E., Tekaslan E., Yildiz S., **Demiroglu Y.** “Multi-Fidelity and Multi-Disciplinary Design Optimization of A Low-Boom Supersonic Transport Aircraft” *AIAA Scitech Forum*, Washington DC USA, 23-27 January 2023.
- Tekaslan E., **Demiroglu Y.**, Nikbay M. “Surrogate Unsteady Aerodynamic Modeling with Autoencoders and LSTM Networks” *AIAA Science and Technology Forum*, San Diego, CA, USA, 3–7 January 2022.

- **Demiroglu Y.**, Nikbay M. "A Comparative Study on Multi-Fidelity Sonic Boom Prediction for a Supersonic Aircraft" *An ECCOMAS Thematic Conference on Multidisciplinary Design Optimization of Aerospace Systems*, Lisbon, Portugal (online conference), July 21-23, 2021.

- Tekaslan E., Yildiz, Ş., **Demiroglu Y.**, Nikbay M. "Implementation of Multidisciplinary Multi-Fidelity Uncertainty Quantification Methods in Sonic Boom Prediction" *AIAA Aviation Forum*, Washington, DC, USA, August 7-11, 2021.

- **Demiroglu Y.**, Yildiz, Ş., Nikbay M. "Multi-fidelity Sonic Boom Minimization of A Supersonic Aircraft by Parametric Wing Shape Design" *AIAA Science and Technology Forum*, Tennessee, USA, January 11-15, 2021.

- Yildiz, Ş., **Demiroglu Y.**, Nikbay M. "Sonic Boom Optimization for The Forebody of a Supersonic Aircraft" (in Turkish) *National Aerospace Conference (UHUK)*, Ankara, Turkey, September 9-11, 2020.

AWARDS:

- ITU Scientific Research Program, June 2019-June 2022
  Master Thesis Grant Support.

- Institution of Mechanical Engineers' Unmanned Aircraft Systems Challenge 2018
  Grand Champion, Safety & Airworthiness Award, Best Flight Readiness Review (ITU Hedef UAV Team).

- Institution of Mechanical Engineers's Unmanned Aircraft Systems Challenge 2017
  Manufacturing Award, Best Flight Readiness Review (ITU Hedef UAV Team).

- Cansat Competition 2017 - American Astronautical Society, NASA Goddard Space Center
  4'th Place Award (ITU Apis Team).